Synthesis and Properties of Molecular Nanostructures on Surfaces

Nasiba Abdurakhmanova

to my parents,
Gulmirzo Abdurakhmonov and Gulbahor Vahidova,
for their infinite love and support

Let us permit nature to have her way.
She understands her business better than we do.
Michel de Montaigne

Abstract

One central aim of nanotechnology is the creation and exploitation of nanostructured materials with pre-programmed architecture and properties. The fabrication of functional nanostructures relies on versatile protocols of synthetic chemistry enabling the precise control of reactions at the molecular level. The surface-supported nanostructures investigated in this thesis have been synthesized using extended concepts of synthetic chemistry. To this end, mainly two chemical bonding types were employed: metal-organic coordination and covalent bonding. The resulting structures were characterized by scanning tunneling microscopy (STM) under ultra-high vacuum (UHV) conditions. Furthermore, the electronic and magnetic properties of the coordination structures were investigated by x-ray absorption spectroscopy (XAS) at the synchrotron radiation facility in Grenoble, France.

The thesis is organized into the following three topics:

- *Organizational chirality of metal-organic coordination networks on a metal surface.* The metal coordination networks formed by 7,7,8,8-tetracyanoquinodimethane (TCNQ) and Mn as well as Cs adatoms on Ag(100) are presented in chapter 3. The metal atoms form very similar chiral complexes with TCNQ. The complexes organize into densely packed and highly ordered domains whose organizational chirality depends on the metal center. This issue is addressed by theoretical modeling. It is shown that the flexibility of the metal-organic coordination bond plays a key role in the supramolecular chirality. Mn forms rigid and directional bonds resulting in a heterochiral packing of the complexes. This organization avoids electrostatic repulsion between adjacent cyano groups of TCNQ. In the Cs-TCNQ$_4$ structure this is achieved by an umbrella-like folding of four TCNQs around the central Cs atom, which yields a denser homochiral packing. This is enabled by the flexible nature of the ionic bonds. Moreover, the alkali atoms allow a mean to modify the electrostatic properties of the organic adlayer, which is important for the design of metal-organic interfaces in electronic devices.

- *Electronic and magnetic properties of the Me-TCNQ structures on metal surfaces.* Previous investigations based on x-ray photoemission spectroscopy and density functional theory calculations for the Me-TCNQ$_x$ systems on Cu(100) and Ag(100) surfaces show that two charge transfer (CT) channels are present, i.e, metal adatom-TCNQ and substrate-TCNQ. The choice of the substrate significantly influences CT, thereby controlling the electronic properties. In chapter 4 the magnetic properties of Ni-TCNQ and Mn-TCNQ structures on Ag(100) and Au(111) is presented. It is shown that the magnetic properties of Mn-TCNQ structures are essentially the same on Ag(100) and Au(111) surfaces, whereas for Ni-TCNQ the influence of the substrate is very pronounced. Both Ni-TCNQ/Au(111) and Ni-TCNQ/Ag(100) show ferromagnetic (FM) behavior, with stronger coupling observed on Au(111). This fact is especially interesting since the Ni impurities are found to be nonmagnetic on both substrates. The observations are linked to the different CT channels and possible coupling mechanisms are identified.

- *The covalent bond formation reactions.* Chapter 5 discusses the on-surface controlled synthesis of carbon-based nanostructures. The investigation of the properties of carbon-based nanostructures requires a better control over the synthesis process. To this end, one of the strategies proposed is the use of well-defined precursor molecules, which are deposited and activated on the surface to obtain the final structure. The surface catalyzed cyclodehydrogenation (SCDDH) reaction was used for the synthesis of fullerenes and nanotube caps. The selectivity of the C-C bond formation process is shown. Based on this result the isomeric pure C84 higher fullerene was synthesized. The same method was applied to the synthesis of nanotube caps. The precursor-based approach was also applied to the synthesis of N=9 and N=15 graphene nanoribbons (GNRs). Polyphenyl precursor molecules have been employed, which allow a synthetically simple mean to adjust the width of the ribbons. However, the resulting GNRs comprise many defects and the coupling mechanism is not very effective. The aspects of surface supported reactions are discussed and possible improvement strategies are proposed.

Keywords: *Scanning tunneling microscopy, time-of-flight secondary ion mass spectroscopy, X-ray absorption spectroscopy, ferromagnetism, chirality, reactions at surfaces, TCNQ, metal-organic coordination, self-assembly, fullerenes, graphene nanoribbons, carbon nanotubes, precursors*

Kurzzusammenfassung

Eines der Ziele der Nanotechnologie ist die Herstellung von Nanostrukturen und Materialien mit vordefiniertem Aufbau und Eigenschaften. Für die Realisierung werden vielseitige Ansätze der synthetischen Chemie verwendet, die eine präzise Kontrolle der Reaktionen auf molekularer Ebene erlauben. Die in dieser Doktorarbeit untersuchten Nanostrukturen auf Oberflächen wurden mittels erweiterter Konzepte der synthetischen Chemie hergestellt. Hierzu wurden hauptsächlich zwei chemische Bindungstypen untersucht: die metallorganische Koordinationsbindung und die kovalente Bindung. Die hergestellten Strukturen wurden mittels Rastertunnelmikroskopie im Ultrahochvakuum charakterisiert. Weiterhin wurden die elektronischen sowie magnetischen Eigenschaften der Koordinationsstrukturen mittels Röntgenabsorptionsspektroskopie am Synchrotron in Grenoble untersucht.

Die Doktorarbeit ist in die folgenden drei Themenbereiche unterteilt:

- *Chiraler Aufbau von metallorganischen Netzwerken auf einer Metalloberfläche.* Die Koordinationsnetzwerke gebildet aus 7,7,8,8-tetracyanoquinodimethane (TCNQ) und Mn sowie Cs Adatomen auf Ag(100) werden in Kapitel 3 betrachtet. Die Metallatome bilden mit TCNQ chirale Komplexe auf der Oberfläche, die sich strukturell sehr ähnlich sind. Die Komplexe bilden dichtgepackte und hochgeordnete Domänen aus, die sich abhängig vom Metallzentrum in ihrer Chiralität unterscheiden. Dieser Sachverhalt wird mittels theoretischer Modellierung analysiert. Es wird gezeigt, dass die Flexibilität der Metallkoordinationsbindung eine Schlüsselrolle in der supramolekularen Chiralität spielt. Mn bildet starre und gerichtete Bindungen mit TCNQ und führt zu einer heterochiralen Packung der Komplexe. Diese Packung vermeidet die elektrostatische Abstoßung zwischen benachbarten Cyano Gruppen des TCNQs. In der Cs-TCNQ$_4$ Struktur wird dies mittels einer schirmartigen Faltung von vier TCNQ Moleküle um das zentrale Cs Atom erzielt, was somit zu einer dichteren homochiralen Packung führt. Dies wird durch die flexible Natur dieser ionischen Bindung ermöglicht. Zudem erlauben die Alkali Atome die Modifizierung der elektrostatischen Eigenschaften der organischen Schicht, was für das Design metallorganischer Übergänge in der Elektronik von Bedeutung ist.

- *Elektronische und magnetische Eigenschaften von Metall-TCNQ Strukturen auf Metalloberflächen.* Vorangegangene Röntgenphotoemissionsspektroskopie und Dichtefunktionaltheorie Untersuchungen für die Mn-TCNQ$_x$

Systeme auf Cu(100) und Ag(100) Oberflächen zeigen die Existenz zweier Ladungstransferkanäle, d.h. Metall-Adatom-TCNQ und Substrat-TCNQ. Die Wahl des Substrats beeinflusst signifikant den Ladungstransfer und kontrolliert somit die elektronischen Eigenschaften. In Kapitel 4 werden die magnetischen Eigenschaften der Ni-TCNQ und Mn-TCNQ Strukturen auf Ag(100) und Au(111) behandelt. Es wird gezeigt, dass sich die magnetischen Eigenschaften der Mn-TCNQ Strukturen auf Ag(100) und Au(111) Oberflächen im Wesentlichen ähneln, während bei Ni-TCNQ der Einfluss des Substrats sehr ausgeprägt ist. Sowohl Ni-TCNQ / Au(111) als auch Ni-TCNQ / Ag(100) zeigen ferromagnetisches Verhalten, wobei auf Au(111) eine stärkere Kopplung beobachtet wird. Diese Tatsache ist insbesondere interessant, da einzelne Ni Atome auf beiden Substraten kein Spin-Moment besitzen. Die Beobachtungen werden mit den unterschiedlichen Ladungstransferkanälen diskutiert, und mögliche Kopplungsmechanismen werden identifiziert.

- In Kapitel 5 wird die oberflächengesteuerte Synthese kohlenstoffbasierter Nanostrukturen diskutiert. Um die Eigenschaften von kohlenstoffbasierten Nanostrukturen zu untersuchen, ist eine verbesserte Kontrolle des Syntheseprozesses erforderlich. Eine der hierzu vorgeschlagenen Strategien ist die Verwendung definierter Präcursor-Moleküle, die zur Bildung der Zielstruktur auf die Oberfläche deponiert und aktiviert werden. Zur Synthese von Fullerenen und Nanoröhrenkappen wurde die oberflächenkatalysierte Cyclodehydrogenierungsreaktion verwendet. Es wird die Selektivität des C-C Bindungsbildungsprozesses gezeigt. Von diesem Ergebnis ausgehend wurde das hhere Fulleren C_{84} isomerenrein synthetisiert. Dieselbe Methode wurde zur Synthese von Nanoröhrenkappen angewendet. Die Präcursor basierte Methode wurde ebenfalls zur Synthese von N=9 und N=15 Graphennanoribbons (GNRs) angewendet. Hierzu wurden Polyphenylmoleküle verwendet, die es ermöglichen die Breite der GNRs einfach einzustellen. Die erzielten GNRs weisen jedoch viele Defekte auf, und der Kopplungsmechanismus ist nicht sehr effektiv. Die Aspekte der oberflächengestützten Reaktionen werden diskutiert und mögliche Verbesserungsstrategien vorgeschlagen.

Stichworte: *Rastertunnelmikroskopie, Flugzeit-Sekundär-Ionen Massenspektrometrie, Röntgenabsorptionsspektroskopie, Ferromagnetismus, Chiralität, Oberflächenchemie, TCNQ, Metallorganische Koordination, Selbstorganisation, Fullerene, Graphennanoribbons, Kohlenstoff Nanoröhren, Präcursor-Moleküle*

Sommario

Uno degli obiettivi delle nanotecnologie consiste nel creare nanostrutture e materiali con struttura e proprietà programmate *a priori*. Per raggiungere questo obiettivo, vengono largamente utilizzate delle procedure versatili di sintesi chimica che consentono un preciso controllo delle reazioni a livello molecolare. Metodi di sintesi modificati ad hoc sono stati utilizzati per la sintesi in-superficie delle nano strutture studiate in questa tesi. Sono stati considerati due tipi di forze motrici: la coordinazione metallo-organica ed il legame covalente. Le strutture ottenute sono state caratterizzate con la microscopia a effetto tunnel (STM) in condizioni di ultra alto vuoto (UHV). Inoltre, le proprietà elettroniche e magnetiche delle strutture di coordinazione sono state analizzate con la spettroscopia di assorbimento di raggi X (XAS) presso il sincrotrone ESRF di Grenoble, Francia.

In questa tesi sono stati affrontati tre argomenti principali:

- *Chiralità supramolecolare di network a coordinazione metallo-organica su superfici metalliche.* I sistemi di interesse sono i network di coordinazione formati da 7,7,8,8-tetraciano-chinodimetano (TCNQ): Mn-TCNQ$_4$ e Cs-TCNQ$_4$ su Ag(100). Nonostante le geometrie strutturali siano molto simili, la loro organizzazione in strutture estese si dimostrata essere diversa. Questo aspetto viene trattato attraverso un modello teorico. Si dimostra infatti che la flessibilità del legame di coordinazione metallo-organico gioca un ruolo chiave nel guidare la chiralità supramolecolare. I rigidi legami direzionali formati dal Mn risultano in un impacchettamento eterochirale per evitare la repulsione elettrostatica tra i gruppi ciano adiacenti all'interno del TCNQ. Nella struttura del Cs-TCNQ$_4$ questo scopo é raggiunto attraverso una disposizione a ombrello di quattro TCNQ attorno allatomo centrale di Cs. Ciò é unicamente possibile grazie alla natura flessibile dei legami formati dagli ioni dei metalli alcalini e governa l'omochiralità del sistema. Inoltre, gli atomi alcalini forniscono un mezzo per modificare le proprietà elettrostatiche dello strato organico depositato. Questo aspetto é importante per la progettazione di interfacce metallo-organiche.

- *Proprietà elettroniche e magnetiche delle strutture di Me-TCNQ su superfici metalliche.* Attraverso spettroscopia di fotoemissione di raggi X e calcoli di teoria del funzionale della densità per i sistemi di Me-TCNQ$_x$ su superfici di Cu(100) e Ag(100) si dimostra che ci sono due canali di trasferimento di carica (charge transfer CT), ovvero quello ad atomo metallico-TCNQ e substrato-TCNQ. La scelta del substrato influenza significativamente i CT o elimina uno dei due canali di CT, condizionando di conseguenza le propriet elettroniche. I risultati sono discussi nel capitolo 4. Viene presentata l'evoluzione delle proprietà magnetiche delle strutture 1:1 del Ni-TCNQ e del Mn-TCNQ su Ag(100) ed Au(111). Si mostra che le proprietà magnetiche delle strutture di Mn-TCNQ sono essenzialmente le stesse sulle superfici di Ag(100) e Au(111), mentre nel caso del Ni-TCNQ l'influenza del substrato risulta più pronunciata. Entrambi NiTCNQ/Au(111) e Ni-TCNQ/Ag(100) presentano un comportamento ferromagnetico (FM), con un ferromagnetismo più pronunciato su Au(111). Questo fatto é particolarmente interessante dal momento che si é scoperto che le impurezze di Ni su entrambi i substrati si trovano in uno stato di *spin quenched*. Le osservazioni sono infine collegate ai canali di CT e vengono identificati alcuni possibili meccanismi di *coupling*, in particolare il Rudermann-Kittel-Kasuya-Yoshida (RKKY).

- Il capitolo 5 tratta della sintesi, controllata in superficie, di nanostrutture a base di carbonio. Lo studio delle proprietà di queste nanostrutture richiede un maggior controllodel loro processo di sintesi. Una delle strategie proposte l'uso di molecole ben definite come precursori, che vengono depositate sulla superficie ed attivate per formare la nanostruttura desiderata. La reazione di ciclo-deidrogenazione (SCDDH) catalizzata in superficie é stata usata per la sintesi di fullereni e di calotte (caps) di nanotubi. Viene illustrata la selettività della formazione del legame C-C. Sulla base di questo risultato é stato sintetizzato il fullerene C_{84}. Lo stesso metodo stato applicato per la sintesi di caps di nanotubi. L'approccio basato sull'impiego di precursori é stato inoltre applicato per la sintesi di nanostrisce di grafene (GNRs) con N=9 e N=15. Dal momento che le GNRs ottenute non erano interamente prive di difetti, vengono infine discussi vari aspetti che favoriscono ed influenzano la reazione, assieme ad alcune possibili strategie per migliorarla.

Parole chiave: *microscopia a effetto tunnel, spettroscopia di massa a tempo di volo, spettroscopia di assorbimento di raggi X, ferromagnetismo, chiralità, reazioni di superficie, TCNQ, coordinazione metallo-organica, self-assembly, fullereni, nanoribbons di grafene, nanotubi di carbonio, precursori.*

Contents

Chapter 1

Introduction

The emergence of quantum mechanics in the beginning of the 20th century has led to a deeper understanding of the properties of condensed matter. The fundamental properties of matter were found to emerge from the peculiar behavior of electrons and nuclei. As a result, a boom in engineering and science has followed, the most famous examples of which are semiconductor electronics and information technology. These are true examples of how science changes our daily lives. The current fabrication technologies utilize a top-down approach which comprises precise iterations of deposition and patterning to create integrated circuits. As device miniaturization continues, the bottom-up strategy becomes a more efficient way to create the desired structures. The bottom-up approach utilizes the concepts of molecular self-assembly and recognition where complex systems are fabricated from relatively simple molecular building blocks. Therefore, the phenomena at the atomic and molecular scale become extremely important. The investigations and manipulation of these objects is the realm of nanoscience. Since novel and intriguing phenomena emerge due to a reduction in size, nanoscience has attracted wide interest from both fundamental and technological points of view.

Structuring surfaces has been an efficient strategy to bestow functionality on materials. For many cases in the macroworld the role of the surface can be reduced to merely a support. However, for nanoscale objects the presence of the surface and its properties become crucial. Many parameters characterizing the behavior of nanostructures change dramatically with the choice of different substrates. In an attempt to better understand these issues and resolve related difficulties, the whole field of surface science has emerged. Surface science primarily focuses on the physical phenomena and chemical reactions occurring at the both sides of the interface and is a very active area of research at present. The emergence of various techniques has largely contributed to our understanding of the physics and chemistry at surfaces and interfaces. Among these, the class of scanning probe methods stands alone as they provided new insight and understanding of the surface-related effects. Especially the role of scanning tunneling microscopy [1] cannot be undervalued. With its unique ability to resolve matter at the submolecular and atomic level and complemented by other spectroscopic techniques and theoretical methods it has demonstrated its unparalleled importance in various areas of surface science. Not only has it demonstrated its ability to deliver topographical information, but also its potential for manipulating matter in the atom-by-atom fashion [2–4] was shown. In addition, its spectroscopic capability allows us to obtain detailed chemical and electronic information at the atomic scale[5, 6].

One of the famous quotes of Pauli goes 'God made solids, but surfaces were the work of the Devil'. In light of recent achievements in the field of surface science it would perhaps be more correct to say that surfaces are a blessing from God. Surfaces lend themselves to the studies of adsorption/desorption phenomena, reactivity, catalysis [7], investigations of arrangements of various types of molecules and their properties upon adsorption [8–13]. A decade ago the principles of supramolecular chemistry were successfully applied on surfaces, boosting research in this direction. Supramolecular chemistry, a chemistry beyond the single molecule, focuses primarily on systems of molecules where the self-assembly and/or molecular recognition guide the molecular organization into a specific structure [14, 15]. The detailed self-assembly path of a particular system depends on specific interactions between the molecular building blocks, their structure and the functional groups comprising them. The interactions involved are generally of the non-covalent type, being, e.g., metal-ligand interactions, hydrogen bonding, van-der-Waals interactions, electrostatic forces, etc. In general, these intermolecular forces are weaker than covalent bonds which is reflected in the thermodynamic properties of the resulting supramolecular structures. The lack of stability is paid off by the high flexibility of these bonds. A simple annealing can be used to cure the structural errors to reach thermodynamic equilibrium. Formation of structures via self-assembly has the advantage of being a fast, parallel, method of producing larger area nanostructures compared to an atom-by-atom manipulation with STM where only a very limited number of structures per unit area can be created [2–4, 16].

Metal-organic coordination is one of the most widely used strategies to organize molecules into a supramolecular architecture [14, 17, 18]. The concepts of coordination chemistry were established more than a century ago[19] and nowadays it has turned into an efficient tool for the predictable organization of organic ligands and metals to steer supramolecular coordination. Various types of coordination frameworks with intriguing properties have been synthesized. The concept was applied to rational crystal engineering and used to understand the catalytic processes in enzymatic proteins containing transition metals. The latter led to the synthesis of a wide range of metal-organic catalytic materials, the properties of which were studied both experimentally and theoretically. In this light, the investigation of transition metal coordination structures on surfaces is of great importance and interest, especially since the local probe methods can be directly used to visualize the structure. Another aspect of metal-organic coordination structures is the subject of magnetism. One of the recent advances of solution-based chemistry is the synthesis of the family of molecule-based magnets ranging from the single molecule to bulk crystals [20–22]. For many of them interesting properties were demonstrated. Apart from scientific importance, molecular magnets are potential successors of conventional bulk metal magnets due to their relatively simple fabrication, tunability of magnetic properties via the synthesis and ability to create surface-supported thin-films compatible with current technology. Despite the intensive research dedicated to molecular magnets, for some of them the origin of their properties remains unclear due to the lack of long-range order in the bulk material. Therefore, investigation on surfaces would help to understand the structure-property relationship in these materials. Naturally, fabrication of metal-organic networks on surfaces derives inspiration from solution-based supramolecular chemistry but several additional important aspects arise. One of them is the structural aspect linked to the confinement to the surface. That is, the growth behavior is affected by the surface and, in general, the effect of the surface cannot be fully predicted. The second aspect concerns the adsorbate-surface interaction leading to electronic modifications of both sides of the interface. As a consequence, the properties of the supported networks are modified and the degree of change depends on the interaction strength. The latter one can be tuned by the appropriate choice of the substrate.

Among the various attributes that an organic molecule can bring to a metal surface, there is one that requires particular attention. This is the question of structural chirality. Chirality is simply a geometric property where the mirror transformation of an object is a non-identity operation, i.e., the object and its mirror image are non-superimposable by any translation or rotation. As a result, a chiral object can exist in two distinguishable, enantiomeric, forms. The property of chirality has profound effects in physics, chemistry and biology, ranging from parity violations for weak forces, to the exclusive use of one mirror form of amino acids by all life forms on earth. Chiral expression at surfaces has attracted increasing attention only in recent years, despite the fact that it is actually easier to create chirality in a two dimensional (2D) system, since a surface cannot possess a center of inversion and can only maintain reflection mirror symmetry planes normal to the surface. Although intrinsically chiral metal surfaces can be created by cutting a crystal along certain crystallographic planes to expose step and kink sites that are chiral [23–25], the interesting point for the organic/inorganic interface is how the adsorption of organic molecules bestows chirality to a previously achiral surface. The emergence of various surface science techniques and ready availability of UHV technology have enabled a detailed investigation and high control over the molecular species to be studied. A wide range of molecular systems was investigated [26–28]. Among these STM studies combined with theoretical modeling have proven to be the most fruitful in explaining the enantioselective assembly and the fundamental processes of chiral recognition [29, 30]. Understanding these principles is important as they govern the basic mechanisms of living systems. Furthermore, the creation of enantiomorphic domains and complete monolayers of molecules bestowing chirality upon an achiral surface is of particular relevance for heterogeneous enantioselective catalysis [31–33].

The molecular nanostructures formed via self-assembly and held by noncovalent bonds possess a high degree of flexibility due to the reversible nature of the interactions involved. However, these structures are inherently fragile and the intermolecular interactions are weak, which prevents, e.g., the mechanical stability or efficient intermolecular charge transport. Clearly, structures held by covalent bonds would show more stability due to higher bond strength. Creation of these large structures of a particular configuration is experimentally a difficult task. First, it requires large molecules which are difficult to synthesize by conventional organic chemistry. Secondly, and this is important for local probe investigations, even if the synthesis is possible, they can hardly be deposited intact under ultra-high vacuum conditions because of their high molecular weight. To overcome this problem, it is necessary to form covalent bonds between the molecular units directly on the surface. The on-surface synthesis has several advantages over the traditional synthetic chemistry route. On-surface experiments in UHV allow better control and a broader range of reaction temperatures to be used without risk of air oxidation or solvent decomposition. The confinement to two dimensions could favor some reactions which are difficult to achieve with three-dimensional systems. This can happen as a result of entropic or kinetic effects or due to interaction with the substrate. Moreover, extended 1D, 2D structures can be synthesized, which is not possible in solution due to solubility issues. At last, on-surface reactions can be studied by STM to gain the atomic-scale insights into the reaction path, reactant conformation, adsorption site, etc., and other surface science techniques such as XPS, NEXAFS, UPS and IRS for further characterization. Since the first experiments by Côté *et al.* in 2005 [34] on crystalline extended organic structures formed by covalently bonded organic building blocks, successful synthesis of various covalently bonded nanostructures was reported. These include, but are not limited to, covalent assemblies of large porphyrine molecules [35] and covalent chains [36], imine synthesis [37], formation of molecular domes [38], synthesis of fullerenes [39, 40] and graphene nanoribbons [41], thereby demonstrating the potential of this method.

This thesis presents the results of the investigations of nanostructures formed by metal-organic coordination and by means of on-surface covalent bond formation reactions on well-defined metal surfaces. We start with non-covalently bonded metal-organic nanostructures for which the aspects of structure, chirality, and chemical as well as physical properties are discussed. The substrate dependence of these properties will be elucidated. We further proceed with the synthesis of covalently bound nanostructures on the surfaces, where surface catalyzed as well as surface supported reactions will be presented.

The thesis is organized as follows:

- In **Chapter 2** a brief introduction to the techniques that were used for this work is given. These include: STM, ToF-SIMS, XAS and XMCD. The STM is used to obtain detailed structural information on the supramolecular architectures and nanostructures on surfaces. ToF-SIMS and XAS/XMCD were utilized as complementary techniques to probe the chemical and magnetic state of the systems of interest. At the end of the chapter information on ample preparation is provided.

- **Chapter 3** discusses the topic of chirality of metal-organic systems consisting of Mn/Cs and TCNQ. It is found that Cs and Mn form similar complexes with TCNQ where four TCNQ molecules are coordinated to the central metal. However, the organization of these units into domains is shown to be dependent on the nature of the central metal atom: Cs-TCNQ$_4$ domains contain exclusively homochiral units, while Mn-TCNQ$_4$ domains are heterochiral. A possible explanation for these different organizational chirality based on theoretical modeling is given.

- **Chapter 4** deals with magnetic properties of Ni- and Mn-TCNQ structures on Ag(100) and Au(111) surfaces investigated by XAS/XMCD. The Ni impurities on both surfaces were investigated as a reference and were found to be non-magnetic, while Ni atoms embedded into the networks have shown a relatively strong ferromagnetic coupling. The effect being more pronounced for the NiTCNQ structures on Au(111). Mn atoms in the MnTCNQ networks on Ag(100) and Au(111) were found to be paramagnetic. The results are explained based on different charge transfer channels. Possible coupling mechanisms are discussed.

- The controlled synthesis routes of carbon-based nanostructures are discussed in **Chapter 5**. The precursor-based approach towards the selective production of fullerenes, graphene nanoribbons and carbon nanotubes are proposed. The effect of various parameters governing the reactions on the surfaces are discussed.

- **Chapter 6** concludes and summarizes the findings from these studies. It also presents experimental considerations for further improvements in future work.

Chapter 2

Experimental Techniques

In this chapter a brief description of the experimental techniques employed in this thesis will be given. The first section details the theoretical foundations of Scanning Tunneling Microscopy (STM). In the second section a brief introduction to Time-of-Flight-Secondary Ion Mass Spectroscopy (ToF-SIMS) is discussed, while the third section focuses on X-Ray Magnetic Circular Dichroism (XMCD) used for the investigations of magnetic properties of the nanostructures. The last two sections are dedicated to the experimental set-up and sample preparation.

2.1 Scanning Tunneling Microscopy

STM is the ultimate technique for characterizing the structure and the electronic properties of conducting surfaces at the atomic scale in real space. Even though it was originally used to obtain topographic information, a variety of further techniques have evolved from it later on, e.g. Scanning Tunneling Spectroscopy (STS), local luminescence excitation and spin polarized STM [42, 43]. In this section the basics of topographic imaging principles of STM are given.

STM is based on the quantum mechanical tunneling effect. The basic operation principles are sketched in Figure 2.1. A metallic tip is positioned a few Å above a conductive or semiconductive sample. Either the tip or the sample is mounted on a piezoelectric scanner to allow scanning in the

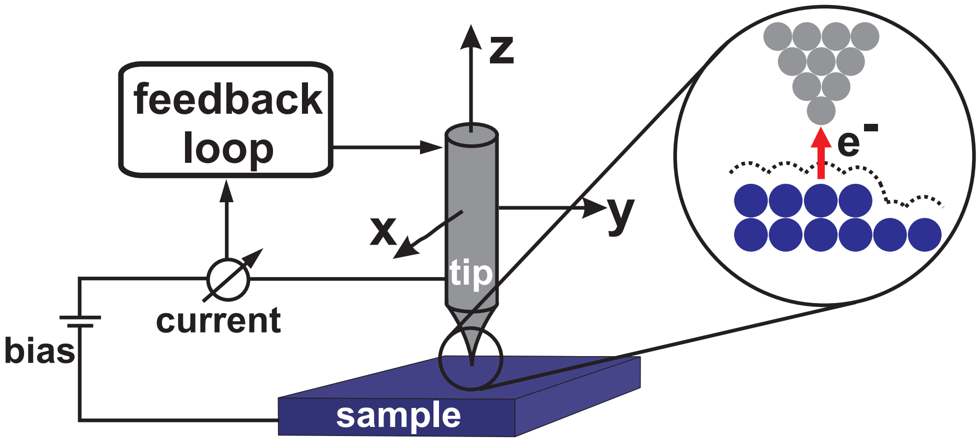

Figure 2.1: Schematic illustration of a scanning tunneling microscope.

XY-plane. Due to the small tip to sample distance, the wavefunctions of the sample and the tip overlap. By applying a bias between the sample and the tip, electrons can tunnel through the vacuum barrier. Calculation of the tunneling current requires detailed knowledge of the wave functions of the tip and the sample. However, details of the electronic structure of the tip are usually not known. In a simple approximation the tip is regarded as a protruding piece of Sommerfeld metal with a radius of curvature R. Further, it is assumed that only the s-wave solutions of this quantum mechanical problem (spherical potential well) are important. Tersoff and Hamann [44, 45] used this simplification to describe the relation between the tunneling current $I(V)$ and the local density of states (LDOS) of the tip ρ_t and the sample ρ_s leading to the following expression:

$$I(V) \propto \int_{-\infty}^{\infty} \rho_s(E)\rho_t(E-eV)\tau(E,V,z)(f(E-eV,T)-f(E,T))dE. \quad (2.1)$$

$f(E-eV,T)$ and $f(E,T)$ are the Fermi distributions of tip and sample at a temperature T and an energy E; V is the applied bias between tip and sample and $\tau(E,V,z)$ is the transmission coefficient of the tunneling gap and is given by [46]:

$$\tau(E,V,z) = \exp\left(-2z\sqrt{\frac{m_e}{\hbar^2}(\Phi_s+\Phi_t-2E+eV)}\right) \quad (2.2)$$

where z is the width of the tunneling gap (i.e. the distance between tip and sample), m_e is the electron mass and Φ_s and Φ_t are the workfunctions of the sample and the tip, respectively. At low temperatures the Fermi distribution can be simplified to a step function which yields for 2.1:

$$I(V) \propto \int_0^{eV} \rho_s(E)\rho_t(E-eV)\tau(E,V,z)dE. \tag{2.3}$$

If $V \ll \Phi_s, \Phi_t$ the transmission coefficient can be further simplified to:

$$\tau(z) = \exp(-2z\sqrt{\frac{m_e}{\hbar^2}(\Phi_s+\Phi_t)}) \tag{2.4}$$

Thus, expression 2.3 can be rewritten as

$$I(V) \propto \tau(z)\int_0^{eV} \rho_s(E)\rho_t(E-eV)dE. \tag{2.5}$$

The first factor shows that the tunneling current depends exponentially on the tip-sample distance and the second factor shows the dependence on the LDOS of the tip and sample. It should be mentioned that approximation 2.4 is not valid for high voltages (>1 V). However, high voltages are often required to perform STM measurements on semiconductors. As a consequence, the transmission coefficient can not be separated from the integral, as it was done to obtain equation 2.5, which leads to a weighting of the LDOS by $\tau(E,V,z)$.

As illustrated in Figure 2.1, the x-y-piezo scanner is used to scan over the sample surface to measure the tunneling current as a function of the lateral position of the tip. In the constant current mode the electronic feedback control keeps the tunneling current constant by readjusting the height of the tip by means of the z-piezo scanner. In contrast, in the constant height mode, the height is kept constant and the current is recorded in dependence on the sample position. All the STM measurements shown in this work are performed in constant current mode.

2.2 Time-of-Flight Secondary Ion Mass Spectroscopy

Since part of the results obtained in Chapter 5 is based on ToF-SIMS measurements a basic introduction to the technique will be given here.

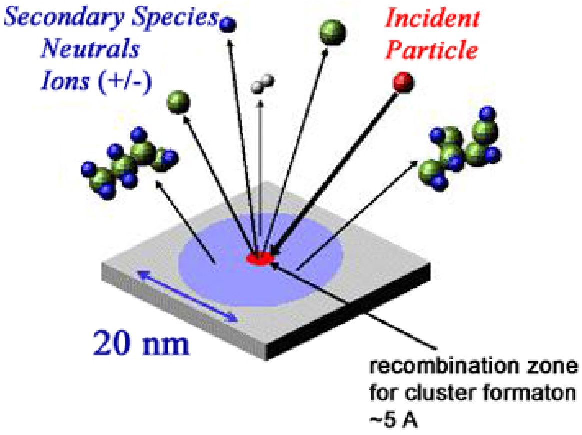

Figure 2.2: Particle beam interaction using ToF-SIMS. Incident particles bombard the surface liberating single ions (+/-) and molecular compounds.

ToF-SIMS (Figure 2.2) is a surface-sensitive analytical method that uses a pulsed ion beam (Cs or microfocused Ga) to remove molecules from the outermost surface of the sample. The particles are removed from atomic monolayers on the surface (secondary ions). These particles are then accelerated into a "flight tube" and their mass is determined by measuring the exact time at which they reach the detector (i.e. time-of-flight). Three operational modes are available using ToF-SIMS: surface spectroscopy, surface imaging and depth profiling. Analytical capabilities of ToF-SIMS include:

- Mass resolution $M/\Delta M > 10000$. Particles with similar nominal mass (e.g. Si and C_2H_4, both with amu = 28) are easily distinguished from one another.
- Mass range of 0-10,000 amu; ions (positive or negative), isotopes, and molecular compounds (including polymers, organic compounds, and up to amino acids) can be detected.
- Trace element detection limits in the ppm range.
- Sub-micron imaging to map any mass number of interest.
- Depth profiling capabilities; sequential sputtering of surfaces allow analysis of the chemical stratigraphy on material surfaces (typical sputtering rates are $\sim$100 Å/minute).
- Retrospective analysis. Every pixel of a ToF-SIMS map represents a full mass spectrum. This allows an analyst to retrospectively produce

maps for any mass of interest, and to investigate regions of interest for their chemical composition via computer processing after the dataset has been instrumentally acquired.

2.3 XAS and XMCD

X-ray absorption spectroscopy (XAS) is an element specific technique that allows probing of unoccupied electronic states of a given material. The absorption spectra are recorded within a certain photon energy range and therefore a tunable light source is required which is provided by synchrotron facilities. The synchrotron radiation offers high intensity and brilliance in a wide range of energies.

XAS experiments with polarized light allow probing the magnetic state of the system. Qualitatively this is explained by a dependence of the absorption cross section on the relative orientation between sample magnetization **M** and photon helicity **P**. The light can be tuned to have linear or right (R) and left (L) circular polarization. The corresponding helicity is conventionally labeled as $\mathbf{P^0}$ for linear and $\mathbf{P}^{\pm}$ for R and L circular polarization. In Figure 2.3 XAS spectra of Ni in the NiTCNQ network on Au(111) recorded at $L_{2,3}$-edges are shown. The spectra have been recorded for R and L circular polarized light, and it is evident that the absorption cross section is different in the two cases of parallel (I^+) and antiparallel (I^-) alignment of the magnetic field and photon helicity (T=8 K, B_z=5 T, Fig. 2.3(b)). The X-ray magnetic circular dichroism (XMCD) is simply defined as the difference in the absorption cross sections between I^+ and I^- (Fig. 2.3 (c)). This can be measured equivalently by using R and L circular polarization or by changing the magnetization direction for a given helicity. The maximum dichroism effect is obtained when the magnetization is aligned with the photon spin direction. If there is an angle θ between the two, then the XMCD signal is scaled by $\cos\theta$.

It will be shown in the following, that the XMCD intensity is proportional to the imbalance between the minority and majority $3d$ states above the Fermi level, which in turn is proportional to **M**. Changes in the XMCD therefore record variations of **M**.

The starting point to explain the sensitivity of XMCD to magnetism is the interaction between photons and matter. The light excites electrons in the core levels generating transitions to empty levels with higher energies

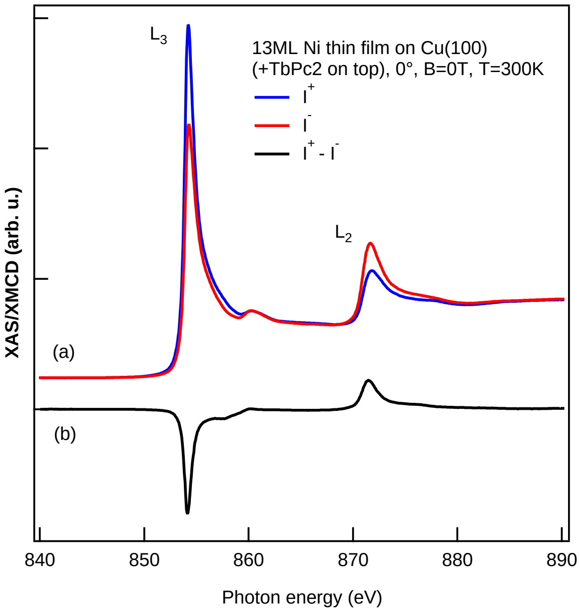

Figure 2.3: (a) XAS spectra at the Ni L-edge for the 13 ML thick Ni layer on Cu(100) recorded for parallel (I^+) and antiparallel (I^-) alignment of the magnetic field **H** and the photon helicity **P**. (b) XMCD signal defined as the difference of the two absorption spectra shown in (a).

(absorption process, see Fig. 2.4). The absorption cross section σ is defined as the number of excited electrons per unit time (or the transition amplitude $w_{i\to f}$ between initial and final state), divided by the incident photon flux I_0:

$$\sigma = \frac{w_{i\to f}}{I_0} \tag{2.6}$$

The transition amplitude per unit time is given to first order perturbation theory by Fermi's golden rule:

$$w_{i\to f} = \frac{2\pi}{\hbar}\sum_f |\langle f|\hat{H}_1|i\rangle|^2\delta(E_f - E_i - \hbar\omega) \tag{2.7}$$

where E_f , E_i are the energy of final and initial states, respectively. The Hamiltonian $\hat{H}_1$ describes the absorption process and is given by $\hat{H}_1 = -\frac{e}{mc}\mathbf{A}\cdot\mathbf{p}$ with $\mathbf{A}$ being the vector potential of the electromagnetic radiation and p the momentum operator of the electron. $\hat{H}_1$ is the first term of the full Hamiltonian that describes the interaction between matter and light, and also comprises scattering terms [47]. Without going into details, to calculate the absorption cross section in Eq. 2.6 one makes the approximation that during the absorption process the core-electron, localized around the nuclei, does not 'see' the spatial variation of the electromagnetic wave and therefore $e^{ik\cdot r} \sim 1$ (electric dipole approximation). This approximation is valid in the energy range of soft X-rays. $\mathbf{k}$ is the light wave vector and $\mathbf{r}$ is the space coordinate of the electron wavefunction. A further assumption concerns the electron excitation process which is considered to be a one-electron process. This allows one to write the initial state as a core wavefunction and the final state as a valence state electron wavefunction [48]. All the other electrons are assumed not to take part in the X-ray transition process. With these approximations Eq. 2.6 becomes [49]

$$\sigma = \frac{4\pi^2 e^2}{\hbar c}\hbar\omega \sum_f |\langle f|\mathbf{P}\cdot\mathbf{r}|i\rangle|^2 \rho(E_f = E_i + \hbar\omega) \tag{2.8}$$

where $\rho(E)$ is the density of unoccupied final states. Usually, for circularly polarized light the propagation direction is chosen to point along the z axis, that corresponds to the quantization axis of the system, given by the magnetization direction. Permitted transitions are only those for which the matrix element in Eq. 2.8 is not zero. One finds conditions for the quantum numbers of the final state, also known as electric-dipole selection rules. These conditions are:
$\Delta j = 0, \pm 1; \Delta l = \pm 1; \Delta s = 0; \Delta m_l^{linear} = 0; \Delta m_l^{R/L} = +/-1$
j, l, and s are the quantum numbers of the total angular momentum, the orbital angular momentum and the spin momentum. m_l and m_s are the components of the orbital and spin moments along the quantization direction. The superscript label of m_l indicates the light polarization. The dipole operator $\mathbf{P}_\pm \cdot \mathbf{r}$ does not involve the electron spin, and thus the photo-electron spin is conserved during the absorption process. Furthermore, if the photoelectron originates from a spin-orbit split level, e.g. the $p_{3/2}$level, the angular momentum of the photon can be transferred in part to the spin through the spin-orbit coupling. As will be shown more precisely below, since the $p_{3/2}$ and $p_{1/2}$ levels have opposite spin-orbit coupling ($l+s$ and $l-s$, respectively), the spin-polarization will be opposite at the two edges, L_3 and L_2.

For transition metal elements the dipole-permitted excitations from core p to valence d states have energies in the soft X-ray range. For $3d$ transition metals the dipole selection rules allow the following transitions:

K: $1s \rightarrow 4p_{1/2}$
L_2: $2p_{1/2} \rightarrow 3d_{3/2}, 4s$
L_3: $2p_{3/2} \rightarrow 3d_{3/2,5/2}, 4s$,

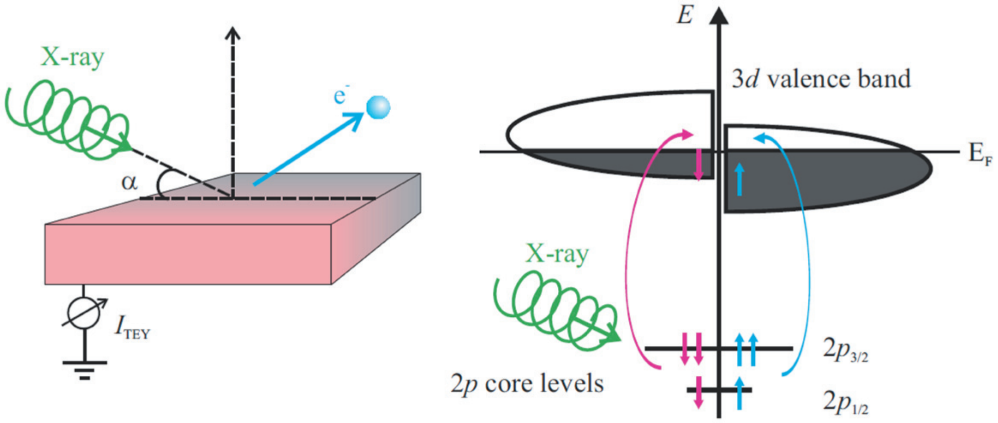

Figure 2.4: (a) (a) Schematic drawing of the XAS measurement in the TEY mode; (b) Absorption process in the case of $2p \rightarrow 3d$ transitions.

The p to d channel often called 'white lines' largely dominates the absorption process by 95%[50].

The sum of the L_3 and L_2 line intensities after the correction for transitions into continuum states is proportional to the number of holes in the $3d$ band. This correction is usually done by the subtraction of step functions from the experimental XAS[51]. In the absence of spin-orbit coupling at the final states, a ratio (so called branching-ratio defined as $L_3/(L_2+L_3)$) $2:1$ is expected for the white line intensities at the L_3 and L_2 edges for unpolarized radiation, which reflects the degeneracy of the $p_{3/2}$ and $p_{1/2}$ states.

If one interprets the absorption as a two-step process then, in the single electron approximation, after the initial excitation step and in the absence of correlations between core hole and valence electron the absorption cross section is also proportional to the density of final states Eq. 2.8. In the absence of a net magnetization (spin-polarization) in the final state, that is if spin-up and spin-down states are equally populated, there is no difference between the spectra taken with R- and L-circularly polarized photons and no dichroism is observed. The total (spin up and spin down) transition intensities for R and L circular polarization are in fact identical. The total spin polarization for the p level, summing up over the $p_{3/2}$ and $p_{1/2}$ manyfolds, is also equal to zero.

The situation is different if the $3d$ band of the metal is split into a spin majority and a spin minority band, i.e., the empty states have predominantly minority character. In this case the final states act as a filter for the spin of the excited photoelectron. If for example there are only spin down empty states, then the dichroic signal will only be sensitive to spin down electrons. The XAS signal at the L_3 edge will be larger for L (62.5% spin down) than for R circularly polarized light (37.5% spin down) and *vice-versa* at the L_2 edge, giving a non-zero dichroic signal. If both spin up and down states are available at the final state, then the dichroism is proportional to the difference between them.

Similarly, if the d valence shell possesses an orbital momentum, it will act as an orbital momentum filter for the excited photoelectrons that will also contribute to the dichroic signal. The presence of a non-vanishing orbital magnetic moment in the final state will lead to L_3/L_2 ratios of the XMCD signal which differ from the $2:1$ value. The XMCD at the L_3 edge in fact is found to have a higher intensity than at the L_2, and this effect is attributed to the spin-orbit coupling in the final state that lifts the degeneracy of the d states. Therefore the L_3 and L_2 edges probe different final states, according to the dipole selection rules [50].

Given an experimental set of data one can use the so-called sum rules to extract the orbital and spin contribution to the magnetic moment from an XMCD spectrum, as discussed in the following.

Sum Rules

Three important magneto-optical sum rules [52–55] relate the XAS and XMCD data to the element specific orbital and spin magnetic moment, and to the anisotropy terms of the spin and charge densities in the unit cell. The derivation of these rules has been carried out for electric dipole transitions in a localized model, considering a single ion in an arbitrary crystal field symmetry. Hybridization of the final states is only allowed for intra-shell orbitals, i.e. there is no mixing of the d states with *sp*-like states. The validity of sum rules has been tested both by band-structure calculations and experimentally.

The first rule relates the shell-specific groundstate expectation value of the orbital angular momentum operator $\hat{L_P}$(z is the direction specified by the incident photon beam) to the integral of the XMCD adsorption spectrum taken over the complete core level edge of a magnetically oriented ferromagnetic or ferrimagnetic material. The ground state expectation value of the orbital angular momentum per hole can be expressed as:

$$\frac{1}{n_h}\langle \hat{L_P} \rangle = \frac{\int\limits_{L_3+L_2} dE(I^+ - I^-)}{\int\limits_{L_3+L_2} dE(I^+ + I^- + I^0)} \tag{2.9}$$

where n_h is the number of holes in the d shell, and the denominator term normalizes the XMCD signal to the unpolarized (isotropic) absorption spectrum.

I^0 is the absorption coefficient for linearly polarized light perpendicular to $\mathbf{P}^{\pm}$and it is usually approximated as the average of I^+ and I^-.

The second sum rule relates the XMCD signal to the shell-specific ground-state expectation values of the total spin operator $\hat{S_P}$ per hole and of the intra-atomic magnetic dipole operator $\hat{T_P}$ per hole:

$$\frac{2}{3n_h}\left(\langle S_P\rangle + \frac{7}{2}\langle T_P\rangle\right) = \frac{3\int\limits_{L_3} dE(I^+ - I^-) - 2\int\limits_{L_2} dE(I^+ - I^-)}{\int\limits_{L_3+L_2} dE(I^+ + I^- + I^0)} \tag{2.10}$$

The term containing $\langle T_P\rangle$ arises from the multipole expansion of the spin density: the largest (monopole) term integrated over the atomic volume, corresponds to the isotropic magnetic moment; the next higher (quadrupole) term reflects the lowest order anisotropic spin distribution in the atomic cell and gives rise to the intra atomic magnetic dipole moment $\mu_D = -7\mu_B\langle T_P\rangle$, where $\mu_B = e\hbar/2m_e$ is the Bohr magneton [56]. First principles calculations [57] show that the $7\langle T_P\rangle$ in Eq. 2.10 can be safely neglected for atoms in the cubic symmetry, but that its contribution might be of the order of 10% of $\langle S_P\rangle$ for atoms at the surfaces and interfaces.

The third rule, termed 'the charge sum rule', relates the integrated intensity of the white line to the number of holes n_h in the valence shell as

$$n_h \propto \int\limits_{L_2+L_3} dE(I^+ + I^- + I^0) \tag{2.11}$$

This sum rule neglects 2p→4s and other transitions. Experimentally this implies that the 2p→3d transitions must be separated out of the other transitions.

2.4 Experimental Set-up

All sample preparation and characterization in this thesis was performed *in-situ* under UHV conditions. The STM measurements were carried out in a home-built UHV chamber with a base pressure of $\sim 5 \times 10^{-10}$mbar hosting the variable STM. The chamber is equipped with standard UHV sample preparation tools, such as an ion-gun to sputter-clean surfaces, a quadrupole mass-spectrometer to monitor residual gases and a load-lock unit for sample exchange. Organic and metal evaporators are attached with gate-valves

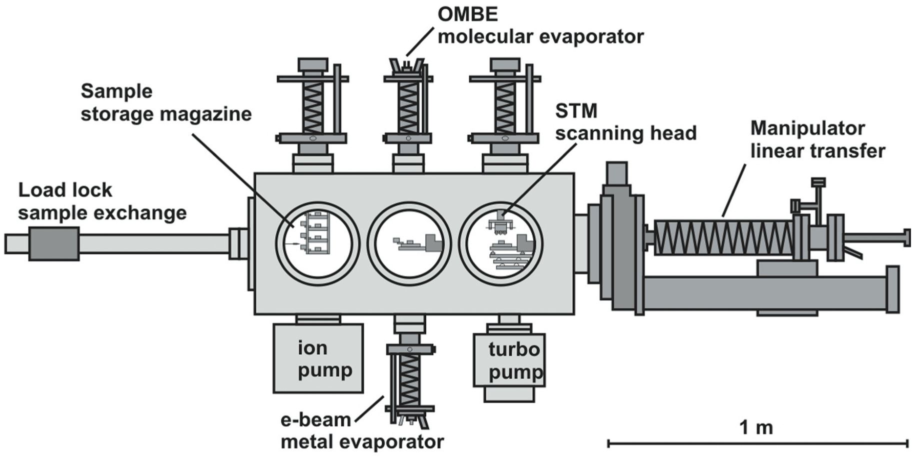

Figure 2.5: (a) Schematic drawing of the UHV-STM system used in the experiments. The base pressure is $\sim 5 \times 10^{-10}$ mbar. The UHV chamber is equipped with organic molecule and metal evaporation sources enabling the *in-situ* sample preparation. The sample holder is attached to the end of the manipulator, which can be transferred to the required position for the sample preparation or characterization. The load-lock system on the left side allows the sample exchange without breaking the vacuum. The figure adapted from [58].

allowing quick exchange of the materials without breaking the vacuum. A sample storage magazine is installed which can host up to four samples. The sample holder is mounted on a movable manipulator and, thus, the sample can be transferred to required position for cleaning, materials deposition or sample exchange. The sample can be heated to 1100 K by electron bombardment using a tungsten filament mounted below the sample (Fig. 2.6). The sample can be cooled down to 100 K with a helium flow cryostat connected by a Cu braid. During the STM measurements the sample-holder is decoupled from the precision tube and rests on a viton-damped copper-stack and at the same time the whole UHV-chamber is suspended from the ceiling by springs.

All the x-ray absorption and time-of-flight measurements were performed in similar UHV-chambers. The Tof-SIMS measurements were conducted at the Interface Analysis Group at the MPI-Stuttgart [59]. The TOF-SIMS data presented in this work were acquired with a TOF-SIMS 5 (IonTOF Corp. Muenster, Germany [60]). This device contains three different ion beam sources for gallium, oxygen and cesium. Oxygen and cesium ion beams of 250 - 2000 eV kinetic energy are used for sputtering in order to remove

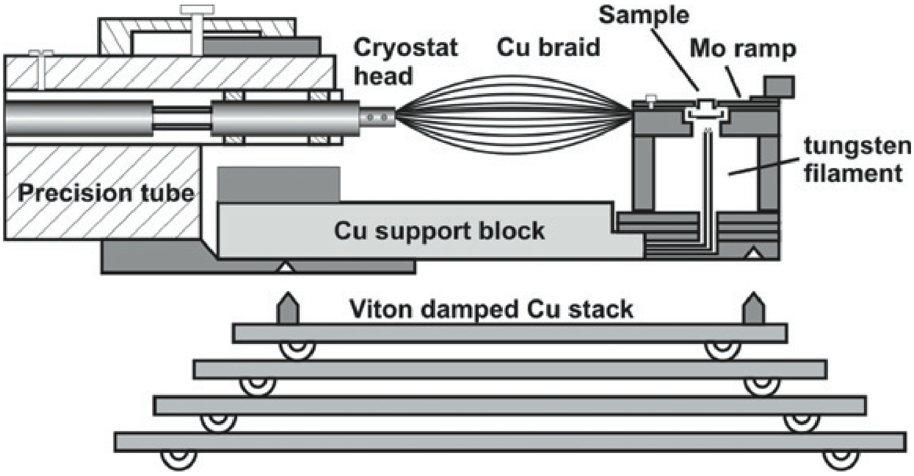

Figure 2.6: (a) Schematic drawing of the sample-holder of the UHV-STM system. Figure adapted from [58].

material for depth profile measurements. The analytical sputtering is done using the Ga^+ beam at an energy of 15 keV or 25 keV. The samples were prepared in a separate UHV-chamber connected to the ToF-SIMS chamber by a gate valve. The samples were transferred using a manipulator without breaking the vacuum. The preparation chamber is equipped with an ion-gun for sputter-cleaning the samples, low-energy electron diffraction (LEED) and Auger electron spectrometer (AES). The sample cleanliness was checked by means of AES.

The XMCD measurements were conducted at the ID08 beamline of ESRF, Grenoble [61]. The UHV-chamber consists of three parts: the preparation chamber, the STM-chamber and the measurement chamber. The samples were characterized by STM prior to the XMCD measurements. The spectra were recorded in the measurement chamber equipped with a cryomagnet operating at the variable magnetic field of $B_z=\pm 5$ T (applied parallel or antiparallel to the beam direction) and at variable temperature of 8-350K. The magnetic field is collinear with the incident beam and the sample can be rotated for angle-dependent XAS-measurements. An evaporator can be mounted for an *in-situ* metal deposition. The XAS spectra were measured in the total electron yield (TEY) mode by measuring the drain current on the sample. The spectra were normalized to the incident photon flux, which is obtained by the photocurrent at the gold grid placed before the sample. The XMCD spectrum is the difference of XAS spectra measured at the opposite helicities, that is right- and left-circularly polarized light.

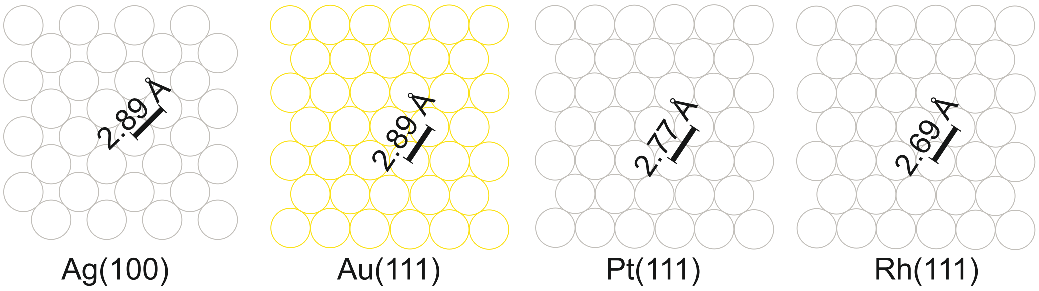

Figure 2.7: Samples used for experiments with the corresponding lattice constants marked.

Sample Preparation

In the experiments reported in this thesis, single crystals of Ag(100), Au(111), Pt(111) and Rh(111) were utilized. All the crystals are face-centered-cubic (fcc). The Ag(100) has a square lattice with the nearest-neighbor distance of 2.89 Å, the other samples have hexagonal lattices with the nearest-neighbor distances of 2.89, 2.77 and 2.69 Å, respectively. The samples were cleaned under the UHV conditions by repeated cycles of sequential Ar^+ sputtering and annealing. The Ar^+ beam was typically set to 1 keV at an incident angle of 45°. The sputtering current detected on the sample was about 1 μA. One cleaning cycle typically took 30 min sputtering and 10-15 min annealing. After a few of these cycles, atomically clean flat surfaces were produced, with the terrace width of about 100 nm.

The organic layers were prepared $in-situ$ under UHV conditions. The molecules (TCNQ-98% Aldrich [62], the other molecules used in chapter 5 were synthesized at the group of Prof. M. Jansen, MPI-Stuttgart[63]) were deposited by organic molecular beam epitaxy from a resistively heated quartz crucible at the deposition rates of 0.01-0.1 ML/min with sublimation temperatures listed in table 2.1. The metals Cs, Mn and Ni were used to produce the M-TCNQ networks. The metals were always deposited after the TCNQ to avoid the surface alloy formation. Cs was deposited by means of resistive heating of an alkali metal dispenser (SAES)[64]. While Ni and Mn were evaporated using an e-beam heated evaporator (EFM3, Omicron) [65]. Both molecular and metallic materials were thoroughly degassed before use. Depending on the experiment, the substrate was kept at room or elevated temperature during the material deposition. The Mn and Ni-$TCNQ_x$ networks on Ag(100) required substrate temperatures of 400 K during the metal deposition, while Cs-$TCNQ_4$ structures on Ag(100) as well as Mn and Ni-

Material	**Sublimation T**
TCNQ	370-400 K
Dibromopentaphenylene	515 K
Dibromotriphenylene	415 K
C_{60} precursor, $C_{60}H_{30}$	750 K
Nanotetrahedra precursor, $C_{60}H_{30}$	750 K
C_{84} precursor, $C_{84}H_{42}$	830 K
Cap precursor **I**, $C_{60}H_{30}$	780 K
Cap precursor **II**, $C_{54}H_{24}$	730 K

Table 2.1: Materials employed in this study and their sublimation temperatures (the structures of the molecules are given in the respective chapters).

TCNQ structures on Au(111) formed at room temperature. The nanoribbon and fullerene precursors were deposited onto the substrates at room temperature as well.

Similar sample preparation procedures were used for ToF-SIMS and XMCD measurements carried out at the Surface and Interface Analysis group MPI-Stuttgart and at ID08-beamline at ESRF Grenoble. The surfaces after the deposition were always checked by either STM, LEED or AES.

Density Functional Theory calculations for the Cs- and Mn-$TCNQ_4$ structures were performed in the group of Prof. A. de Vita, Imperial college, London, UK.

Chapter 3

Tuning the chirality of $MeTCNQ_4$ networks via the nature of the metal center

The crystallization of a mixture of chiral molecules results either in the formation of racemates, i.e., crystals consisting of both enantiomers in equal amounts, or in the separation of enantiomers, forming crystals of a single handedness, known as a racemic conglomerate[66]. The condensation of a particular molecule forming either crystals of mixed or single chirality is, however, poorly predictable. On the other hand, the chemistry of life selects specific chiral enantiomers, using only left-handed forms of amino acids and right-handed forms of sugars. The ability of living organisms to discriminate between two enantiomers of chiral molecules is pivotal for biological processes in cells, and the ingestion of the wrong enantiomer can cause severe harm in some cases[67, 68]. Therefore, understanding the processes of chiral organization and separation at the molecular level is very important not only from an academic point of view, but also for the design of drugs, bio-analytics and in enantiomer-resolved technological processing like asymmetric chiral catalysis. A variety of strategies have been developed to attack these fundamental problems, among which chiral functionalized surfaces are a promising route[23, 24, 69–71]. In general, the presence of a surface restricts the configurational space available for the molecules, effectively altering their mutual interaction[72, 73]. Moreover, the adsorbate-substrate system may introduce additional physical effects, like the creation of surface dipoles and elastic deformations, which can enhance the intermolecular interaction[74, 75].

STM, with its unique capability to image structures with submolecular resolution, has offered a great deal of information on the local structure, chiral organization, separation and recognition of both intrinsically chiral and prochiral molecules on surfaces. Starting with the first studies of chirality of individual molecules in 1998[76, 77], successive investigations demonstrated the spontaneous resolution of a mixture of enantiomers into homochiral molecular pairs, rows and two-dimensional islands[29, 30, 78–83]. Chiral self-assembly and ordering phenomena can also emerge for highly symmetric achiral molecules on non-chiral surfaces, suggesting that surface confinement can ultimately promote and amplify chiral separation of compounds that are racemic in bulk. This, however, introduces a new level of complexity as one has to account for the complex phenomena at the molecule-substrate interface together with the intramolecular interactions. This is exactly where the modern theoretical techniques come into play and where a unique platform for the fruitful synergy of experiment and theory is provided.

In the following, STM and Density Functional Theory (DFT) calculations are combined to shed light onto the assembly phenomena of alkali (Cs) and transition metals (Mn) co-adsorbed with 7,7,8,8-tetracyanoquinodimethane (TCNQ) molecules, forming highly ordered chiral superstructures on the Ag(100) surface. At the surface, chiral metal-TCNQ windmill complexes form, which are stabilized by rather strong metal-ligand interactions for both Cs and Mn atoms. Depending on the nature of the metal center, the complexes organize exclusively into either hetero- or homochiral domains. As it will be shown, this striking difference in the organizational chirality results from pronounced differences in the stiffness of the metal-TCNQ bonding.

3.1 Cs- and Mn-TCNQ$_4$ coordination structures on Ag(100)

In Figure 3.1 the STM images of the metal-organic structures after deposition of Cs and Mn onto the TCNQ layer reveal domains of closely packed mononuclear windmill-shaped units, respectively. These units consist of a central protrusion representing the metal atom, which is surrounded by four TCNQ molecules aligned perpendicular to each other. The arrangement of the molecules around the metal center bestows the units with a rotational sense, i.e., clockwise- (R) and anticlockwise-folded (S) complexes can be distinguished and are highlighted by a yellow and blue square in Figure 3.1d. These entities can be regarded as two-dimensional chiral enantiomers. The packing of these units into an extended superstructure depends on the iden-

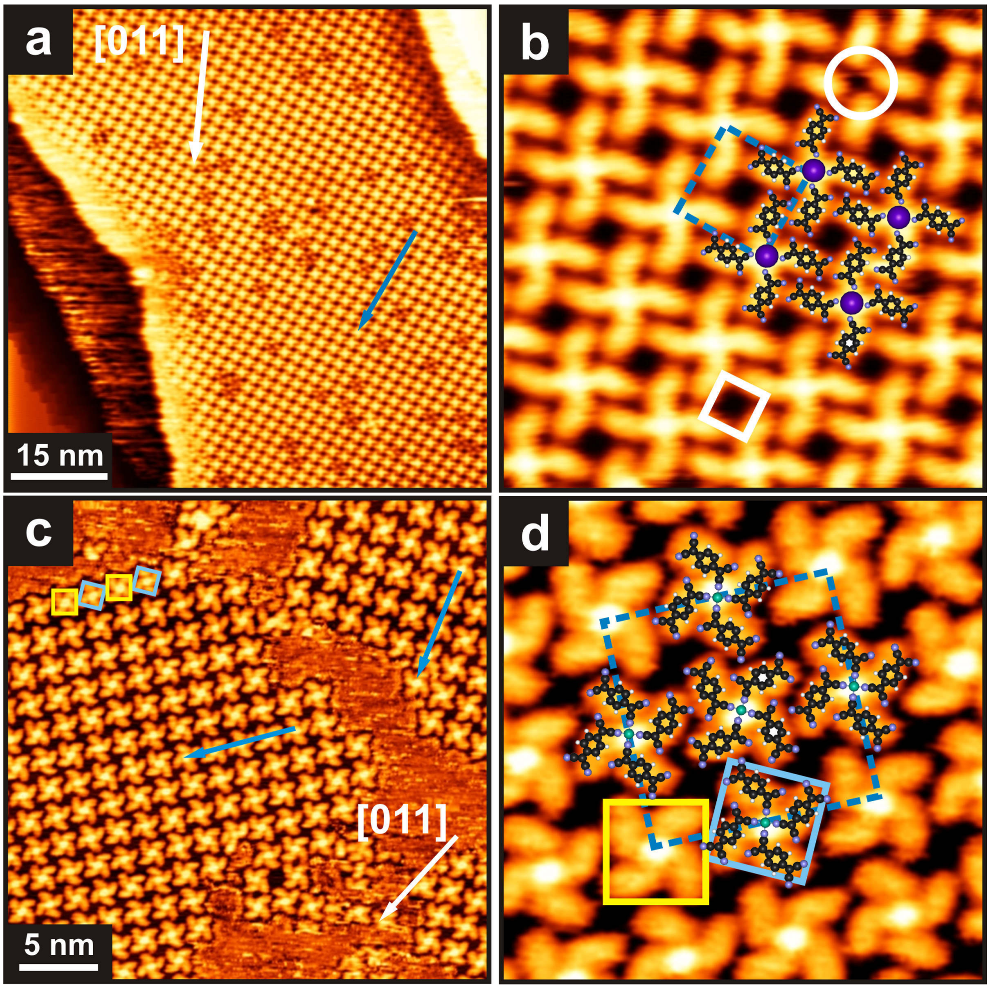

Figure 3.1: STM data of self-assembled metal-TCNQ complexes. (a,b) Cs-TCNQ$_4$ homochiral superstructure: (a) Large-scale image showing a single domain of S-enantiomers (blue arrow indicates the domain orientation). (b) Detailed image (9.1×9.1 nm ^{2}) of the domain structure. The Cs-Cs distance is 18.6 Å. The white circle indicates a Cs vacancy, and the white square marks one of the regularly spaced square-shaped holes in the superstructure. (c,d) Mn-TCNQ$_4$ heterochiral superstructure: (c) Large-scale image showing two non-equivalent heterochiral domains, mirror symmetric with respect to the [011] substrate direction. Blue vectors indicate the domain orientations. Alternating yellow and blue squares symbolize clockwise R- and anti-clockwise S-enantiomers, respectively. (d) Detailed image of the arrangement of the complexes (8×8 nm ^{2}). The dashed square marks the superstructure unit cell (28.1 Å), while the Mn-Mn nearest-neighbor distance is 19.4 Å.

tity of the metal center, although the complexes are structurally very similar for Cs and Mn. Cs-TCNQ$_4$ complexes form domains consisting exclusively of R (or S) enantiomers, whereas the Mn-TCNQ$_4$ superstructure represents a racemic compound with R- and S-units.

The Cs-TCNQ adlayer forms large domains ($>$ 200 nm in size) composed of a single enantiomer. Thus, both the single units as well as the domains are mirror symmetric to each other with respect to the substrate [011] direction. No post-deposition annealing is required to stimulate the superstructure formation. This, together with the presence of mobile adsorbate species, is an indication of a relatively weak interaction of the constituents among each other and a low surface potential corrugation. Figure 3.1a shows one of the homochiral Cs-TCNQ$_4$ domains, which in this particular case consists of S-enantiomers. The orientation of R- and S-domains is defined by connecting the nearest-neighbor Cs centers (indicated by the blue arrow in Figure 3.1a and is approximately ±26.7°with respect to the substrate [011] direction. The domains represent a compact structure with regular square pores (marked by the white square on Figure 3.1b. The square unit cell of the Cs-TCNQ$_4$ superstructure is indicated by the blue dashed square in Figure 3.1b with a periodicity of about 18.6 Å, which corresponds to 6.3a$_0$ (a$_0$=2.89 Å is the lattice constant of the Ag(100) surface). These parameters are compatible with a commensurate superstructure of (6, 3/-3, 6). Despite their ability to form stable domains, Cs atoms seem to be relatively weakly bonded to the TCNQ molecules as suggested by the presence of hopping and missing Cs atoms in the STM images (highlighted by white circle in Figure 3.1b). TCNQ molecules within a complex are adsorbed with their long axis +18.6° to the substrate [011] direction in the case of R-units, and with -18.6° in the case of S-enantiomers. This means that the two equivalent adsorption configurations of the molecules lead to opposite enantiomers upon binding to the metal atoms. The complex is presumably additionally stabilized by the intra-unit hydrogen bonds.

In contrast, the Mn-TCNQ$_4$ network is a racemic compound consisting of R- and S-enantiomers as indicated by the yellow and blue squares in Figure 3.1, panels c and d. Mn-TCNQ$_4$ units are mobile and only observed at step edges or in well-ordered Mn-TCNQ$_4$ domains at sufficiently high concentration of units (Figure 3.1c). The domain size increases with coverage or post-deposition annealing treatment and can reach a width of 100 nm. The fuzziness of the bare metal surface between the domains indicates the presence of mobile species at room temperature.

Two non-equivalent domain orientations can be identified in Figure 3.1c. Both domains consist of the same R and S enantiomers and are mirror-symmetric to the substrate [011] direction. The two domain orientations are indicated by the blue vectors oriented approximately ±19.0 ° with respect to the substrate close-packed direction (Figure 3.1c). The unit cell of the Mn-TCNQ$_4$ superstructure is indicated by the blue dashed square in Figure 3.1d. The size of the unit cell is estimated to be 28.1 $\AA$ ∼9.5 a$_0$ from the STM data. From these parameters we deduce a commensurate superstructure of (9, 3/-3, 9). Similar to the Cs complexes, the R/S Mn-enantiomers are composed of molecules with the long axes oriented +19°/-19° from the [011] direction. The orientation of molecules is nearly identical to this in the pure molecular phase [84]. This suggests that the two equivalent adsorption configurations of molecules lead to distinct chiral motifs upon coordination to Mn. In principle, e.g. the +19°-rotated molecules should form also S-units (i.e. anticlockwise-folded) if only the orientation of the molecules is taken into account. However, this enantiomer has not been observed for this system, suggesting that the surface breaks the symmetry of the ligand.

The formation of extended structures suggests that the surface plays a role in guiding the self-assembly as well as the formation of single units. Furthermore, the racemic packing of R and S enantiomers is likely to be mediated by inter-unit hydrogen bonds. Each Mn-TCNQ$_4$ binds to four adjacent units through these hydrogen bonds. Due to the intermediate strength of both adsorbate-substrate interaction and inter-unit hydrogen bonds, single Mn-TCNQ$_4$ units can reversibly attach to the domain as revealed by the changing domain edges and the presence of mobile single Mn-TCNQ$_4$ units.

Both metals, Cs and Mn, form very similar chiral complexes with TCNQ molecules that bind with one cyano group to the metal atom. The orientation of the molecules in the complex with respect to the surface is nearly identical for both metal centers. The highly ordered domains of single complexes are potentially stabilized by hydrogen bonds between adjacent units. Besides the different chiral organization of the different metal complexes, the Cs superstructure is more densely packed compared to the Mn-TCNQ$_4$ network, despite that Cs ion is larger than Mn and forms a slightly larger complex. Importantly, for Cs-TCNQ$_4$ relatively large domains are easily obtained after metal deposition, indicating a strong tendency of Cs-TCNQ$_4$ to form stable structures. In contrast to Mn-TCNQ$_4$, the preparation of Cs-TCNQ$_4$ domains does not require additional post-deposition annealing.

3.2 Theoretical analysis of the metal binding

DFT calculations were performed in order to rationalize the structural differences between the two metal complexes and the emergence of the distinctive chiral ordering. The analysis includes gas-phase calculations of individual metal-TCNQ$_4$ units, simulations of periodically repeating units in the absence of the surface, and calculations of metal-TCNQ$_4$ units on Ag(100). Relaxed structures and charge density isosurfaces of individual gas-phase units are shown in Figure 3.2. The isosurfaces show that Cs fully donates its valence electron to TCNQ$_4$,mainly to the neighboring nitrogen atoms and 2^{nd} neighbors carbon atoms. The double bond connecting the phenyl ring to the C_3N_2 external groups breaks, and the missing charge goes to the phenyl ring, favoring its aromaticity. This implies an increasing torsional flexibility of the external C_3N_2 group facing the metal, relative to the rest of the molecule. The hydrogen atoms closest to the Cs acquire some charge from the neighboring C atoms, with a corresponding depolarization of the C-H bond. The other hydrogen atoms are unaffected by the metal-molecule interaction. Given the ionic nature of the Cs-TCNQ bond, the latter is non-directional and allows free rotations of the molecules around the Cs^+ ion without much energy cost. In the case of Mn the charge transfer picture is completely different. There is a π-back-donation of a Mn-3d charge on the π^* orbital of the neighbors N-C complex. This implies a rigid, directional coordination bond with most of the charge forming a squared structure parallel to the surface plane. Clearly, the rotational freedom is absent in this case. Both metals yield a stable complex with the four TCNQ molecules, with metal-TCNQ$_4$ binding energies of 7.13 and 4.5 eV for Mn and Cs, respectively. However, different metal-N-C bonding angles of $\sim140°$ and $\sim180°$ are obtained for Cs and Mn, respectively. With the angle of $\sim180°$ the Mn-N-C-C sequence forms a straight line. The different steric flexibility and structural stiffness of the metal-TCNQ$_4$ units revealed by these results have important consequences for the packing of the complexes.

A comparison of the Mn-TCNQ$_4$ fully relaxed heterochiral superstructure with the "best" hypothetical homochiral gas-phase model structure obtained by juxtaposition of the relaxed complexes (Figure 3.3b and 3.3a, respectively) provides more insight on the origin of the global chirality observed in the assembly domains. In the heterochiral structure, the outer, negatively charged TCNQ nitrogens naturally avoid each other, being placed at an average distance of $\sim$3.6 Å. This allows the complexes to remain planar after full relaxation. In the homochiral structure the nitrogen atoms (highlighted by a red ellipse in Figure 3.3a) are instead necessarily very close to each other if the units are constrained to a planar geometry. Upon full structural relaxation, their mutual repulsion is only decreased if a significant out-of-plane buckling of the outer cyano groups (of ∼2 Å, Figure 3.3a, down) is allowed. However, the occurrence of buckling would be highly unlikely on the metal surface, since all cyano groups are expected to form a relatively strong bond with the underlying metal substrate. Similar calculations performed for the homochiral Cs-TCNQ$_4$ network reveal that the 140° Cs-N-C bond angle allows a much more compact arrangement than the one obtained for the Mn enantiomers, consistent with our STM observations. In this case, the mutually repelling nitrogens (Figure 3.3c) avoid each other via an out-of-plane rotation of the whole molecule around its principal axis, permitted by the Cs ionic bond rotational freedom (Figure 3.3d). Unlike the outer cyano moieties out-of plane buckling in the Mn-bound system, this rearrangement is compatible with the presence of the surface.

DFT calculations of Mn-TCNQ$_4$ and Cs-TCNQ$_4$ networks including the Ag(100) substrate (Figure 3.4a,b) strengthen all the arguments above in favour of the Cs-TCNQ$_4$ network stability, and introduce new electrostatic ones. Firstly, these calculations rule out the possibility of N-buckling: in both Cs and Mn complexes we find that the outer nitrogens form covalent bonds

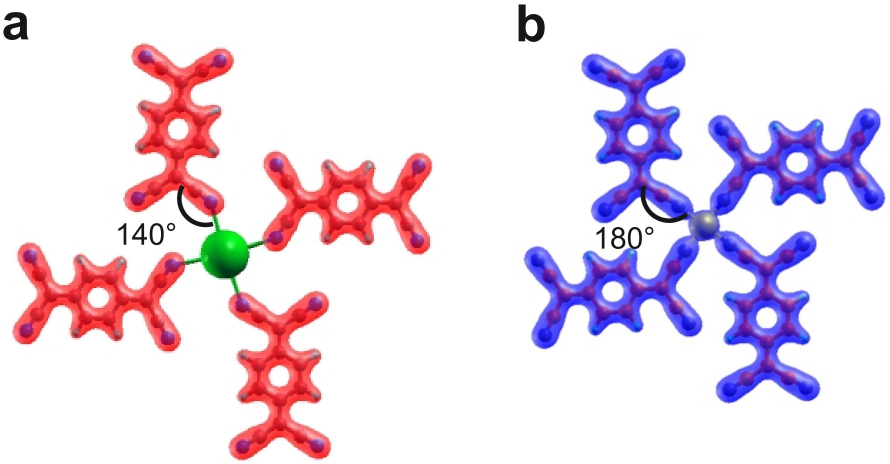

Figure 3.2: Metal-TCNQ$_4$ charge density isosurface of isolated complexes. (a) Cs-TCNQ$_4$ and (b) Mn-TCNQ$_4$. In contrast to Mn which forms directional coordination bonds with TCNQ$_4$, no charge is present around Cs. This shows that Cs fully donates its valence electron to the molecules establishing an ionic bond.

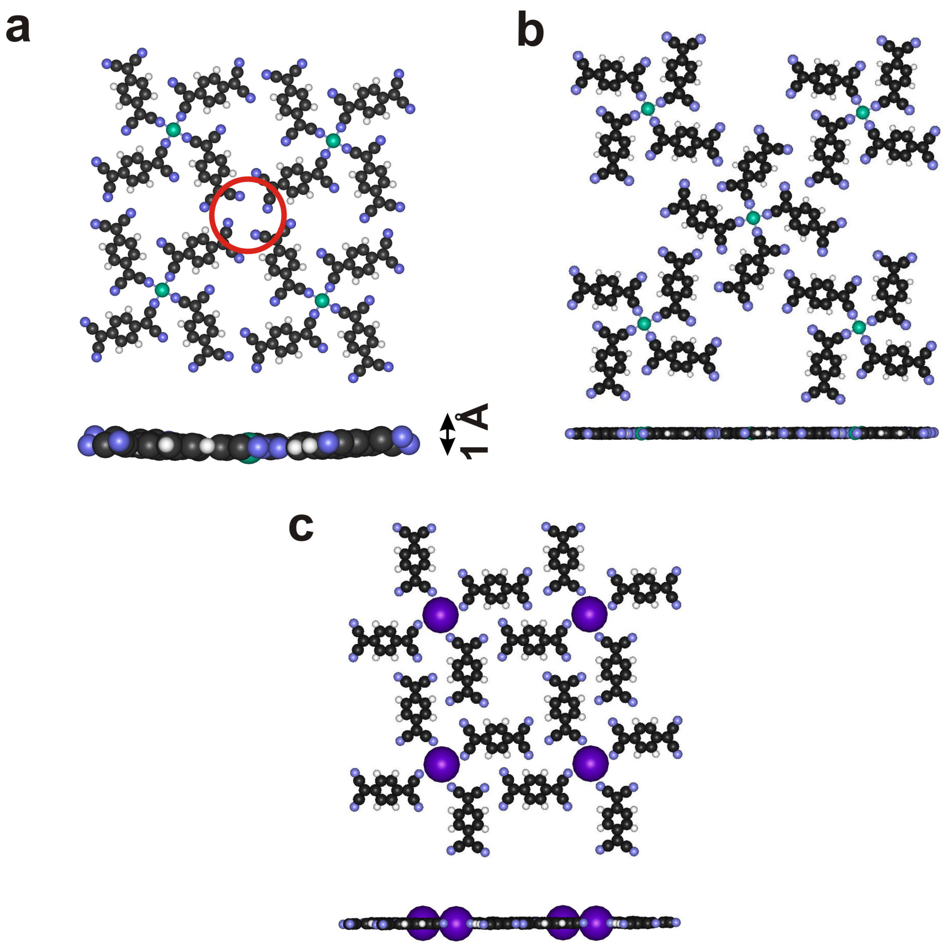

Figure 3.3: Simulations of periodically repeated complexes without surface. (a) Hypothetical homochiral Mn-TCNQ$_4$ structure. Outer nitrogen atoms, highlighted by the red ellipse, repel each other and are buckled upon relaxation (b) Heterochiral Mn-TCNQ$_4$ structure observed in the experiment. The fully relaxed structure remains planar, i.e. the nitrogen atoms avoid each other without causing the buckling. (c) Hypothetical planar Cs-TCNQ$_4$ structure. The 140° Cs-N-C bonding angle allows a more compact structure. After relaxation the structural flexibility allows the rotation of molecules around Cs atoms, pulling the nitrogen atoms apart.

with the surface Ag atoms and reside at approximately the same height above the surface. As found in the gas phase, the Mn atoms occupy the center of their ligands square arrangement, without deformation of the straight metal-ligand Mn-N-C bond alignment, which would be energetically too costly in this structure. The heterochiral arrangement experimentally observed for

Mn-bonded TCNQ layers can thus be simply rationalized as the only way to avoid the repulsive interaction between adjacent complexes without buckling the ligands inducing N-Ag bond breaking. At the same time, the arrangement favours the formation of intercomplex hydrogen bonds. Secondly, significant differences in the relaxation pattern of the two metal-organic layers emerge from the calculations, indicating that the Cs- bonded TCNQ adlayer is electrostatically more stable. We find that while the Mn-TCNQ$_4$ adlayer remains essentially flat upon full structural relaxation (Mn and its ligand N atoms being at a height $z = 2.7$ Å measured from the surface top layer, Figure 3.4b, down), the Cs-TCNQ$_4$ complexes become highly non-planar, with the Cs atoms significantly lifted up from the surface ($z = 5.7$ Å, Figure 3.4a) together with their bonding N atoms (average $z = 4.9$ Å). This novel, out-of-plane "umbrella"-like structure results in a laterally more compact, ordered arrangement, hosting a regular array of holes, as observed in the STM images in Figure 3.1a and b.

To develop further insight on the relative electrostatic stability of the

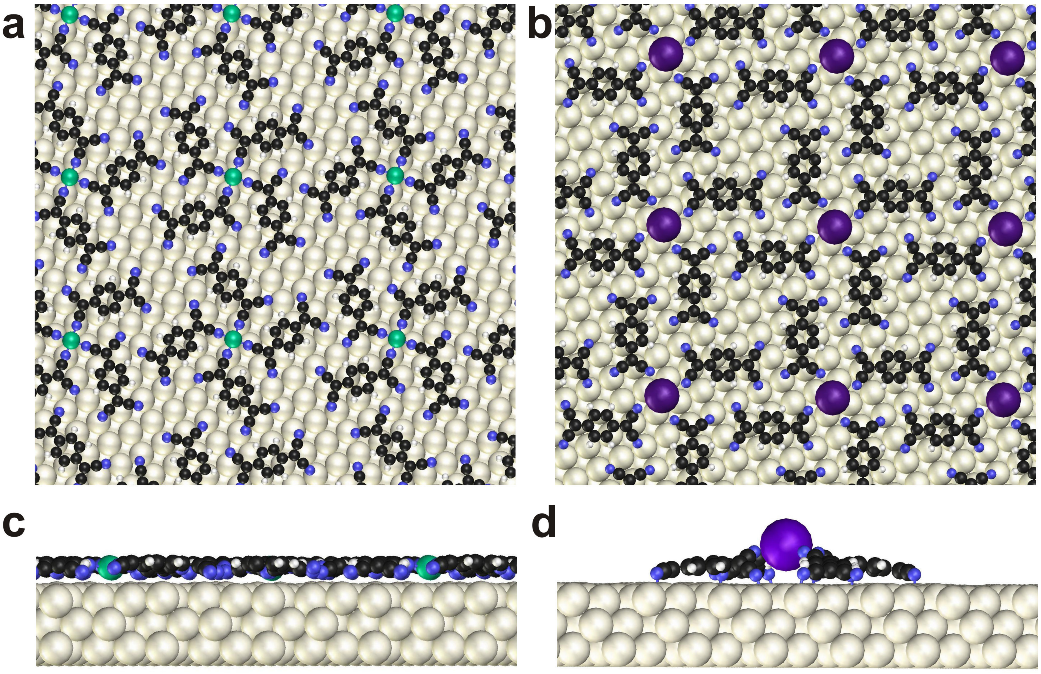

Figure 3.4: Cs-TCNQ$_4$ and Mn-TCNQ$_4$ structures on Ag(100). (a,c) Planar Mn structure. (b,d) Highly non-planar, umbrella like Cs structure, with Cs atom lifted up.

Cs-TCNQ$_4$ and Mn-TCNQ$_4$ adlayers, we next analyze their electron density displacement field. This is defined as the density of the interacting system minus the densities of its three constituents (TCNQ molecules, bridging atoms and Ag substrate, in their electrically neutral states) calculated separately for the same atomic positions of the interacting system. The field is illustrated in Figure 3.5. The metal-organic bonding displacement pattern is clearly visible in the right panel at the bridging Mn sites, while the black depletion zones on the left panel reveal the Cs atoms full ionization, which provides an additional rotational degree of freedom for the molecular adlayer to achieve a stable assembly structure.

We next note that charge transfer from the surface (CTS) to the adlayer is expected in this system. TCNQ has a large electronic affinity (2.8 eV) and the clean Ag(100) work function is 4.64 eV. The 1.84 eV difference between these two values, possibly reduced by "pillow effects", points to a likely charge transfer and hence the polarization of the substrate ("image charge effect") and of the TCNQ molecules themselves. We also note that the Cs-TCNQ$_4$ stoichiometry of the assembly is too unbalanced for the Cs-donated electron to suffice for fully charging up each TCNQ anion and keep the neutrality of the "organic salt" adlayer. Therefore, CTS is expected for the Mn- and Cs-bridged TCNQ adlayers, in both cases resulting in an overall negative surface electric dipole, whose value is ultimately limited by its own electrostatic cost.

Interestingly, our DFT-calculated CTS for the Cs and Mn complexes is -0.39e/TCNQ and -0.33e/TCNQ, respectively. This indicates that the total charge acquired by each TCNQ in the Cs complex (estimated as -0.64e/TCNQ, including the -0.25e/TCNQ donated by Cs atoms) can be significantly larger than for Mn, suggesting that the Cs centers are better suited to the TCNQ electronegative character. This is clearly visible in Figure 3.5, where the yellow-red patterns of accumulated negative charge, reflecting the LUMO state of TCNQ, are distinctively more pronounced in the Cs-bonded system (Figure 3.5, left panel).

Further calculations reveal a 2.01 D/TCNQ electric dipole for the Cs-TCNQ adlayer, significantly smaller than the 2.59 D/TCNQ dipole associated with the Mn-bonded adlayer. Separate calculations on isolated neutral adlayers (in their adsorbed geometry, without including the metal surface) indicate that these dipoles are +3.47D/TCNQ and +1.33D/TCNQ for the Cs and Mn structures, respectively. Thus, the dipole induced by the interaction with the surface is 5.46D/TCNQ (4.00D/TCNQ) for the Cs (Mn)-layer. Clearly, a large cancellation occurs in the alkali metal-bonded adlayer between the positive dipole due to the "lifted up" Cs$^+$ ions and further screened by CTS. A direct consequence is that a higher charge transfer on TCNQ and a smaller electric dipole can be achieved at the same time, stabilizing the Cs-bonded adlayer.

These results suggest that alkali atom bridging can be useful in stabilizing self-assembled structures of electronegative organic molecules adsorbed on metal surfaces. For a start, a better steric performance of flexible units is induced by the ionic, rather than coordination, bonding. Furthermore, the TCNQ molecules will tend to become negatively charged well beyond the charge contribution provided by the alkali donor, and will thus repel each other as a layer of parallel adjacent negative dipoles. The resulting electrostatic cost can be moderated by developing strong positive dipoles at the sites of the alkali atoms, simply increasing their heights and thus their dipolar screening. The height increase will in turn favour further CTS. This interpretation suggests that the adlayer stability and its overall state of charge could be further fine-tuned by different choices of alkali bridging ions.

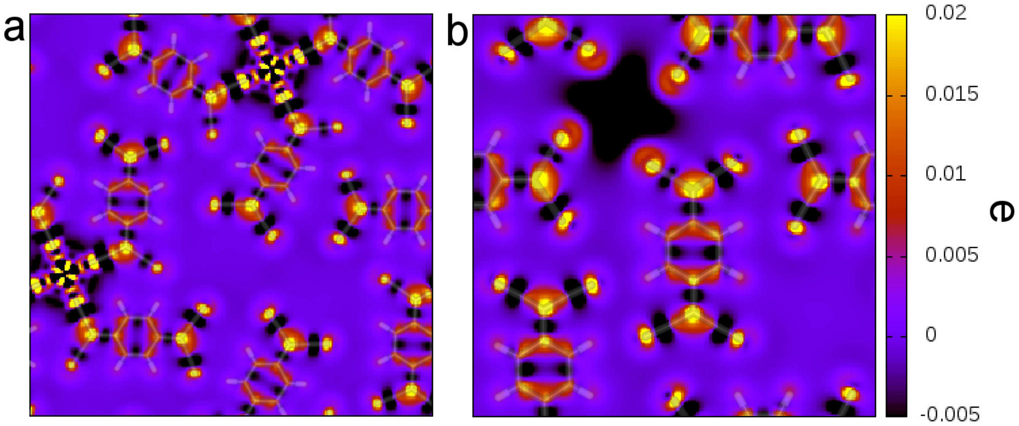

Figure 3.5: Charge density displacement field. (a) Cs-TCNQ$_4$ and (b) Mn-TCNQ$_4$. The plot illustrates the displacement field, i.e., the difference of electron density between the non-interacting components and the full adsorbate system. Positive charge (yellow, red) values indicate charge accumulation during the adsorbate bonding process; negative values (black) refer to charge depletion. Highest positive values (yellow-red) reflect the TCNQ LUMO state.

3.3 Conclusions

In this chapter an important question of the origin of two-dimensional chirality was addressed. The systems of interest consist of *achiral* TCNQ molecules coordinated to alkali metal atoms of Cs and transition metal atoms of Mn on Ag(100) surface. In both cases the elementary block of the domains formed upon coordination consist of central metal atom surrounded by four TCNQ molecules perpendicular to each other, i.e. so-called windmill-shape. As the molecular symmetry is broken upon adsorption on the surface, this results in the clockwise or anticlockwise folding of the molecules around the central metal in both cases. Intriguingly, the overall organization into domain was found to be different for Mn and Cs-TCNQ$_4$units yielding large homochiral Cs-TCNQ$_4$ domains and heterochiral islands of Mn-TCNQ$_4$ complexes on a Ag(100) substrate. Despite the fact that Cs is larger than Mn and, in principle, forms larger units, the Cs-TCNQ$_4$ domains were found to be more densely packed compared to Mn-TCNQ$_4$. STM data alone cannot provide sufficient information to explain these differences in the organizational chirality of these structures.

To address these issues DFT calculations were performed based on the experimental data. DFT calculations show that while the Mn-N coordination bonds are directional, rigid and poorly deformable, the Cs-N bonds are ionic, non-directional and highly flexible. The adlayer structure and global chirality are steered by intracomplex interactions and metal-ligand bonding: switching from directional coordination (Mn-TCNQ$_4$) to flexible ionic bonding (Cs-TCNQ$_4$) results in the switch from heterochiral to homochiral domains. Thus, the control of the intracomplex stiffness offers a route to steer long range organizational chirality and provides a tool for the chiral design of organic crystals. Furthermore, the alkali bridging atom allows charge transfer to the electronegative molecules within the adlayer, which, unlike charge transfer from the surface (CTS), acts as a stabilizing electrostatic effect yielding an alkali organic salt. Moreover, the atomic relaxation of the alkali ions screens the build-up of surface electric dipole, allowing for extra CTS. Thus, the bridging atoms used to control the assembly structure have also a role in the fine-tuning, via dipole formation, the molecular charging and, thus, the overall electronic level alignment of the metalorganic system. These results, connecting molecular charging and assembly properties, are particularly significant in the study of level alignment effects in metal-organic interfaces of great interest in organic electronics.

At last, it was found that Cs-structures form networks with regularly spaced square holes, which could be used as a template to host other molecules with potentially interesting properties. As these pores are also chiral, they can be exploited as a chiral filter for racemic mixtures of small organic molecules, since only molecules of a particular chirality would bind to the R/S-pores of the network.

Chapter 4

Structure and Properties of MeTCNQ$_x$ Coordination Structures on Ag(100) and Au(111)

Metal-organic coordination bonds represent a compromise between bond strength and bond reversibility. The binding energies are higher than in the case of hydrogen bonds, ranging from 50 kJ/mol to 200 kJ/mol [85]. Generally speaking, a coordination system consists of a coordinating metal atom (or cluster of atoms) with one or more electron rich ligands attached to it. Various examples of metal-organic frameworks (MOFs) with a high degree of order in one, two, and three dimensions exist in the literature [18, 22, 86, 87]. The bonding mechanism is discussed controversially in the literature [88], but it is by now well established that the coordination bond has both ionic and covalent contributions [89]. Various theories, which were favored at different times, have been developed - mostly only being able to describe certain aspects of the bond. Ligand field theory for instance describes very well spectroscopic properties. Based on molecular orbital theory the formation of a coordination compound can be described by the following sequence [88]:

- Removal of electrons from the metal center (i.e. oxidation) in order to provide a cation.
- Hybridization of the metal atomic orbitals which provide a set of equivalent hybrid orbitals directed towards the ligands.
- If necessary, rearrangement of the metal electrons to ensure that the hybrid orbitals are unoccupied.

- Formation of covalent σ-bonds between metal center and ligand by the overlap of metal hybrid orbitals with ligand orbitals containing lone-pair electrons.

Hence, the formation of metal-coordination networks is mostly determined by the coordination geometry of the metal center which for transition metals depends on the d-orbital occupation. Under 2D conditions, however, the presence of a metal substrate makes it difficult to predict coordination geometries in comparison to a known 3D analogue. Whereas in 3D the element determines the geometry, in 2D “unusual” motifs can occur. Such deviations can be attributed to charge transfer or substrate screening effects that severely affect the metal-to-ligand bonding and electronic, chemical as well as magnetic properties of a 2D network.

The Me-TCNQ systems investigated here were chosen because of the rich electronic and magnetic properties discovered for the 3D compounds synthesized by the solution supramolecular chemistry methods [90–94]. However, the accurate interpretation of the results was difficult due to the absence of the long-range order in these materials. Nonetheless, it has been suggested that factors such as structure, stoichiometry and synthesis routes can influence the properties of the compounds. Studies of metal-organic coordination at surfaces under UHV conditions, therefore, could offer the advantages of high control over surface composition as well as capabilities for structural determination with atomic/molecular resolution, and determination of magnetic properties. In this chapter the structure and properties of Ni-TCNQ and Mn-TCNQ coordination structures in relation to the underlying metal substrate are reported. Different substrates are used to provide insight into the interplay between adsorbate-adsorbate and adsorbate-substrate interactions. In Section 4.1 the structure and magnetism of Ni-TCNQ complexes on Ag(100) and Au(111) are discussed. Despite the structural similarity found for the x=1 structures on both substrates the different chemical environment provided by Ag and Au leads to distinctively different properties of Ni centers. The effects of the coordination bond strength, charge-transfer channels on the structure formation and magnetism for Mn-TCNQ networks on Ag(100) and Au(111) are described in Section 4.2. Here only a brief information on the Ni and Mn-TCNQ structures will be given.

As was reported in [84] and in [95] Ni and Mn deposited onto the TCNQ precursor layer on Ag(100) react readily with the cyano groups of TCNQ to form mononuclear complexes. Coordination structures formed by these two metals are geometrically nearly identical. The complexes thus formed consist of four TCNQ molecules surrounding the metal center and resemble propellers (see Chapter 3). The complexes pack into domains such that each domain consists of complexes with alternating chirality (the aspects

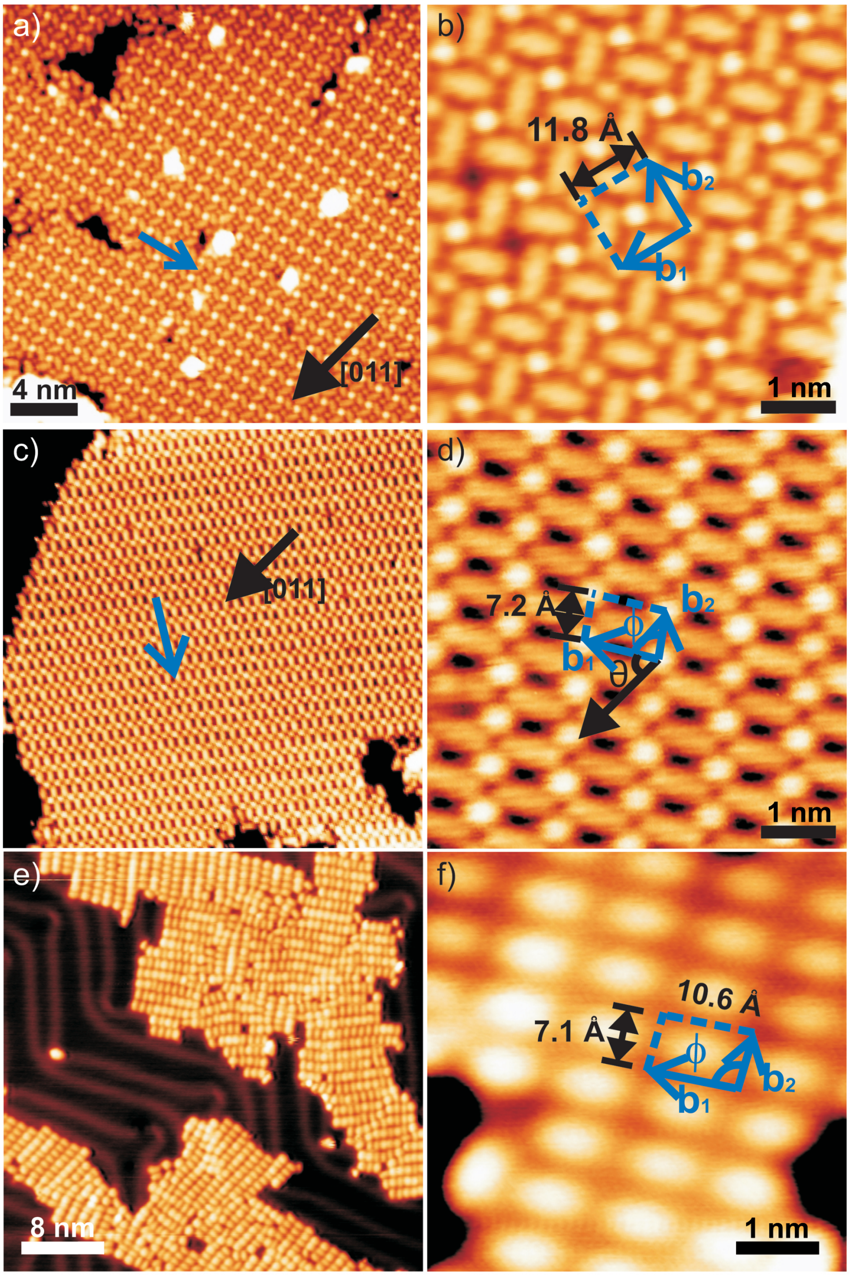

Figure 4.1: STM images of Ni-TCNQ 1:1 structures on (a)-(d) Ag(100) and (e)-(f) Au(111) surfaces. Two phases α (a), (b) and β (c), (d) with 1:1 Ni:TCNQ ratio coexist on Ag(100) surface, and form extended domains. On Au(111) only β type of 1:1 phase is encountered, and is usually found to form small regularly ordered islands merged into a domain.

of chirality were discussed in the previous chapter). Upon increasing the metal concentration another two-dimensional square metal cyanide phase with a stoichiometry of Me-TCNQ$_2$ evolves. The local bonding motif is similar to that in Mn-TCNQ$_2$ networks on Cu(100) [96], that is each TCNQ is monodentately coordinating to two Mn/Ni atoms while each Mn/Ni atom is four-fold coordinated to cyano groups. Further increasing of the Mn/Ni concentration results in the networks with a 1:1 Mn/Ni:TCNQ stoichiometry. Two types of Ni-TCNQ structures are observed, namely the square α phase and rhombic β phase shown in the Fugure 4.1 b, c. In the α phase the molecules orient perpendicular to their neighboring molecules, which is clearly resolved in the STM images. The metal centers are imaged with alternating contrast and no height modulation is found for the molecules. Two domain orientations were found due to the square structure of the α-Ni-TCNQ phase. The domain orientation is defined by the $\mathbf{b}_1$ vector along the shortest Ni-Ni direction. The length of the $\mathbf{b}_1$ vector is 11.8±0.5 Å measured from the STM data. The orientation of $\mathbf{b}_1$ is measured to be 13.8±1.2° from the substrate [011] direction.

In the other type of the 1:1 Ni-TCNQ network, namely the β phase, the molecules within the single domain orient parallel to each other. The rhombic unit is shown on the Figure 4.1. The unit cell parameters are measured to be: $|\mathbf{b}_1|$=11.3±0.2 Å, $|\mathbf{b}_2|$=7.2±0.3 Å, ϕ=85.6±1.5°, and θ=58.5±2.5°. Given these angles the commensurability of the structure is not likely. It also suggests that each Ni center has a distorted fourfold coordination. The fact that β phase forms only at higher annealing temperatures suggests that the system has to overcome an energy barrier since the incommensurability means that the adsorbates are not on energetically favorable sites.

The 1:1 phase can also be produced with Mn atoms. Although both α and β phases are observed in this case too, however with pronounced differences. Initially, only small patches of α phase form, which increase in size upon annealing. The square Mn-TCNQ phase contains many defects and voids, which cannot be eliminated completely even by annealing at 460-470 K. Small domains of β phase are observed as well in contrast to Ni-TCNQ 1:1 structures where large domains of β phase were produced. The differences in structural ordering reflect the chemical dissimilarity of Mn and Ni they cannot be predicted by atomic size or coordination number. They cannot be explained purely from the coordination chemistry point of view. Besides the structural differences, the contrast of the metal centers also shows noticeable alteration. While Ni atoms usually appear relatively bright in the Ni-TCNQ network, Mn centers are imaged as depressions with nonuniform heights. If the nonuniformity can be explained by the structural disorder, the overall contrast is most probably due to the electronic difference of the Mn and Ni-

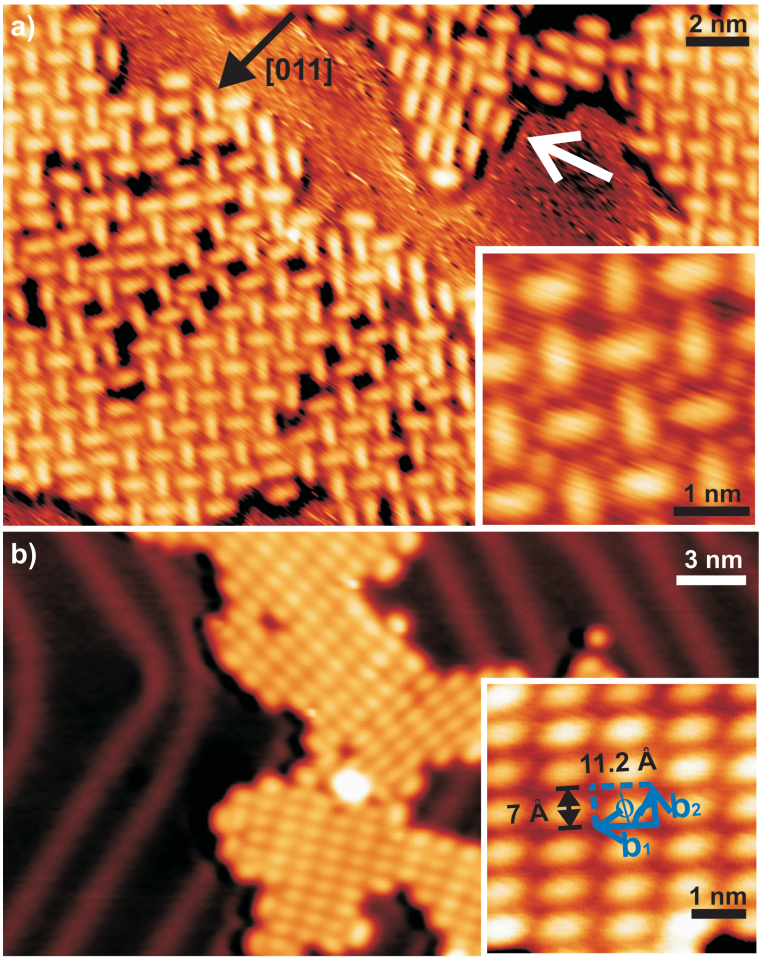

Figure 4.2: STM images of Mn-TCNQ 1:1 structures on a) Ag(100) and b) Au(111) surfaces. The structures on Ag(100) have many similarities to Ni-TCNQ but are considerably less ordered. The inset shows nonuniformity of Mn-TCNQ phase. Mn centers are imaged as depressions compared to TCNQ molecules. Mn-TCNQ structures on Au(111) show a better local ordering but do not form large domains. The local uniformity is clearly visible in the inset b). Alternating contrast is due to the herring-bone reconstruction of the underlying Au(111) surface and Mn centers are imaged as depressions.

TCNQ network.

Unlike on Ag(100), on Au(111) surface only one phase, namely Ni(Mn)-TCNQ 1:1 phase was observed, 4.2a and b. As in the previous cases metal atoms were deposited on top of the precursor layer. The structure formed directly upon the deposition without any post-deposition annealing treatment.

Further increase of metal concentration leads to cluster formation meaning that this phase is the only stable phase on Au(111). The Ni-TCNQ structure is characterized by the unit cell vectors $\mathbf{b}_1$ and $\mathbf{b}_2$, where $|\mathbf{b}_1|$=11.3±0.2 Å, $|\mathbf{b}_2|$=7.2±0.3 Å, ϕ=85.6±1.5°, and θ=58.5±2.5° (cf. Figure 4.1a), while the Mn-TCNQ structure has $|\mathbf{b}_1|$=11.3±0.2 Å, $|\mathbf{b}_2|$=7.2±0.3 Å, ϕ=85.6±1.5°, and θ=58.5±2.5°. Despite the structural similarity, the metal centers in these networks show different contrast. The Ni centers are imaged as depressions, while Mn centers appear as protrusions. The situation is reversed compared to the case of the same networks on Ag(100) surface and certainly indicates a different chemical environment provided by the Au(111) substrate and the electronic differences of Mn and Ni in the networks. These ideas will find their justification when we review the XAS/XMCD data in the following.

XAS and XMCD were used to study the electronic and magnetic properties of Me-TCNQ complexes synthesized on Ag(100) and Au(111) surfaces. In comparison to the metallic Ni and Mn impurities, the XAS multiplet structure at both Ni and Mn L-edges shows the localized $3d$ orbital configuration due to the coordination to the TCNQ molecules. From the XAS lineshapes, the electronic states of Ni and Mn are identified to be mixed $d^8 - d^9$ and d^5, respectively. Further analysis yields valuable information on the magnetic moments of Ni and Mn in the coordination networks.

The experiments were performed at the ID08-beamline of the European Synchrotron Radiation Facility in Grenoble. The coordination structures were prepared *in-situ* and characterized by STM before XAS measurements. For comparison metal impurities were deposited in minute quantities on substrates held at 8 K to obtain isolated metal atoms. XAS spectra were recorded at the metal L-edges and the nitrogen N-edge in total electron yield mode with circularly polarized light (I^+ or I^-) in magnetic fields up to 5 T. XMCD spectra were obtained by taking the difference of the XAS spectra recorded with opposite light polarization. Linearly polarized light (in-plane and out-of-plane) was used to probe the orientations of empty orbitals at grazing incidence angle (θ=70°). In the following the results are organized by the metal coordination species into two sections: Ni-TCNQ and Mn-TCNQ, and the comparison for the properties on Ag(100) and Au(111) is given.

4.1 Ni-TCNQ structures on Ag(100) and Au(111)

In this section the properties of isostructural Ni-TCNQ 1:1 networks on Ag(100) and Au(111) will be given. The XAS spectra for linear polarization (T=8K, B=50 mT) of Ni-TCNQ and 0.018 ML Ni impurities on Ag(100) are shown in Figure 4.3 b) and d). For Ni impurities, the similar L_3 intensities measured at in-plane and out-of-plane light polarizations imply isotropic orbital distribution of the Ni atoms. In the case of Ni centers coordinated to TCNQ, the out-of-plane L_3 intensity almost vanishes. The single in-plane absorption peak at the L_3-edge indicates a single hole in the ground state lying in the surface plane.

XAS spectra measured with right (I^+) and left (I^-) circularly polarized light and corresponding XMCD spectra are shown in Figure 4.3 b) (T=8 K, B=5 T). The lineshape of XAS for Ni impurities on Ag(100) is very simple and has a single peak at the L_3-edge and almost zero L_2 intensity. The absence of the L_2 resonance implies that only the transition from the initial $j = 3/2$ to the final $j = 5/2$ states occurs. The lineshape suggests a d^9configuration. The almost zero XMCD intensity signifies complete quenching of the Ni spin moment. In ferromagnetic Ni, the ground state is represented by the hybridized d^8, d^9 and d^{10} configurations [97, 98]. The observed configuration and non-magnetic behavior is most probably due to the strong hybridization with the substrate. On the other hand, the Ni centers in coordination with TCNQ exhibit substantial XMCD intensity, Figure 4.3. The single L_3 peak and the XAS lineshape indicate a d^9 configuration with the hole in the plane. In addition, the satellite features at ~ 3.2 eV above the L_3 and L_2 mainlines are noticeable in the XAS and XMCD spectra. The satellite peaks can be attributed to the hybridization of the d states with unoccupied s or p states lying above the d band and to the configurational mixing of the d^8 state with the d^9 state. The dehybridization from the substrate is observed for Ni centers in the Ni-TCNQ/Au(111) system as well. The lineshape analysis suggests a mixed valence configuration with d^8, d^9 character. The anisotropic XAS and XMCD spectra are due to the square-planar configuration geometry.

The striking feature in both linearly and circularly polarized XAS spectra of Ni-TCNQ is the energy shift of L_3 peak by 1.1 eV towards higher energies compared to that of Ni impurities (Figure 4.3). It is observed for the Ni-TCNQ networks on both Ag(100) and Au(111) surfaces. This energy shift indicates the strong crystal field environment of the Ni centers due to the rearrangement of atomic orbital upon coordination to TCNQ. Charge

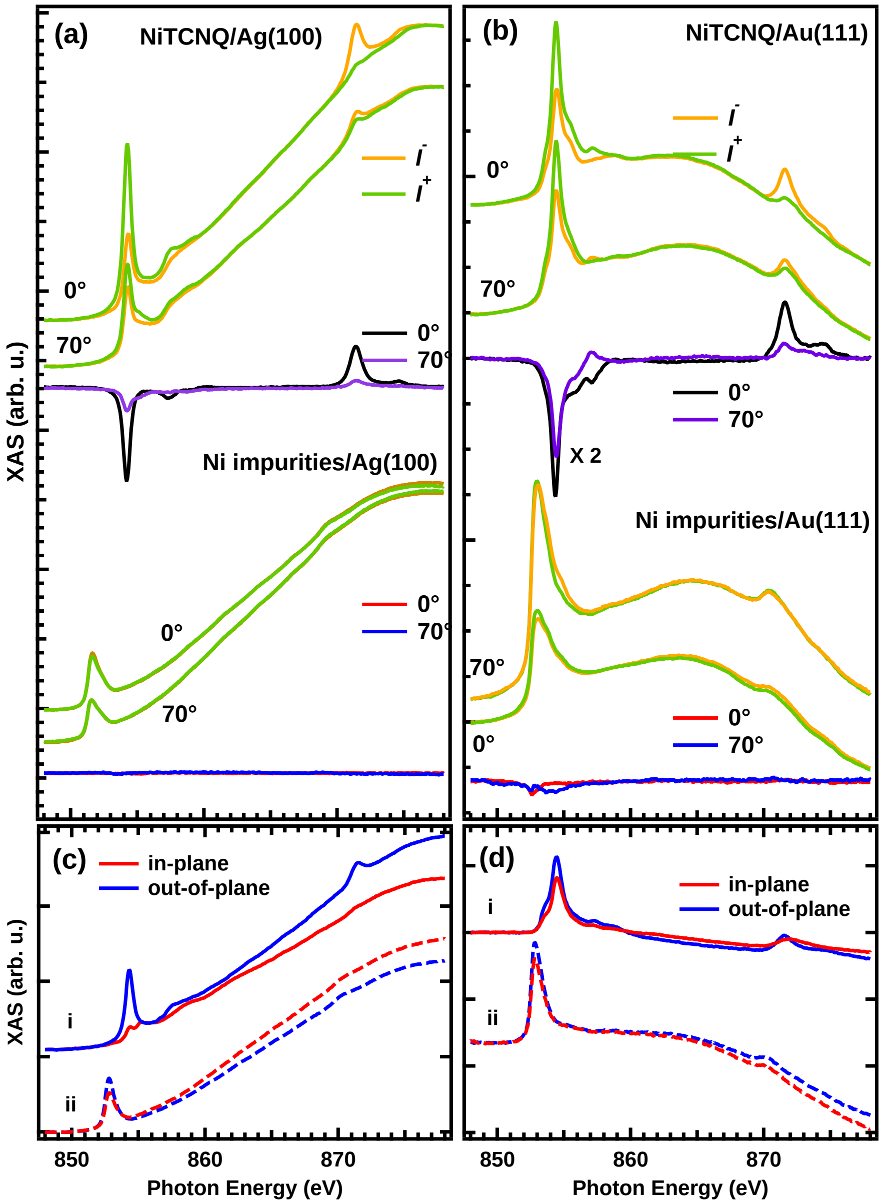

Figure 4.3: XAS spectra measured with linear and circular polarization for Ni impurities and Ni-TCNQ on Ag(100) (panel a) and Au(111) (panel b). (c-d) Spectra with linear polarization were recorded at incidence angles 0° (in-plane) and 20° to the surface normal (out-of-plane). Measurements were performed at T=8 K and B=50 mT. XAS spectra with circularly polarized light were recorded at T=8 K and B=5 T.

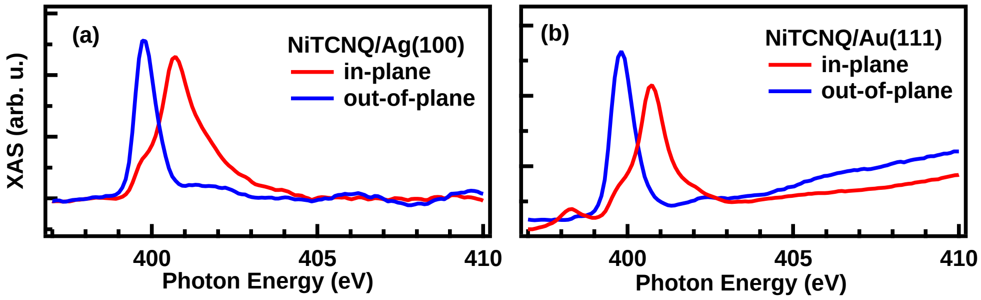

Figure 4.4: (a) and (b) Linearly polarized N edge spectra for Ni-TCNQ on Ag(100) and Au(111) respectively.

transfer effects might contribute to the XAS energy shift as well. In general, the absorption energy increases with the oxidation number. Thus, this energy shift implies that the Ni centers in the network are more positively charged than the Ni impurities supported on the Ag(100) substrate, which is consistent with the assumption of charge transfer from Ni to TCNQ molecules. The charge transfer considerations are supported by the nitrogen K-edge XAS spectra, shown in Figure 4.4. Compared to the TCNQ N1s powder NEXAFS-spectra and N K-edge XAS spectra for TCNQ/Au(111) on Figure 4.6, these spectra are significantly different. For both Ni-TCNQ/Ag(100) and Ni-TCNQ/Au(111) the splitting of the peak 2 is observed. In the case of Ni-TCNQ/Ag(100) this splitting is due to both charge transfer from the substrate and from Ni to TCNQ. However, since the TCNQ/Au(111) nitrogen K-edge spectra strongly resemble those of TCNQ-powder, we conclude that charge transfer from the system is excluded for this system. This is in agreement with recent STS measurements for the TCNQ/Au(111) system where, it was shown that the surface state of Au(111) survives the adsorption process and the STM images of the TCNQ molecules have clearly revealed the unmodified LUMO of the gas-phase molecules [99]. Therefore, the peak

θ	S_{eff}		L	
	I	**II**	**I**	**II**
0°	0.83	1.39	0.07	0.18
70°	0.34	0.64	0.06	0.22

Table 4.1: Spin and orbital moments for NiTCNQ on Ag(100)(**I**) and on Au(111) (**II**) as calculated using sum rules.

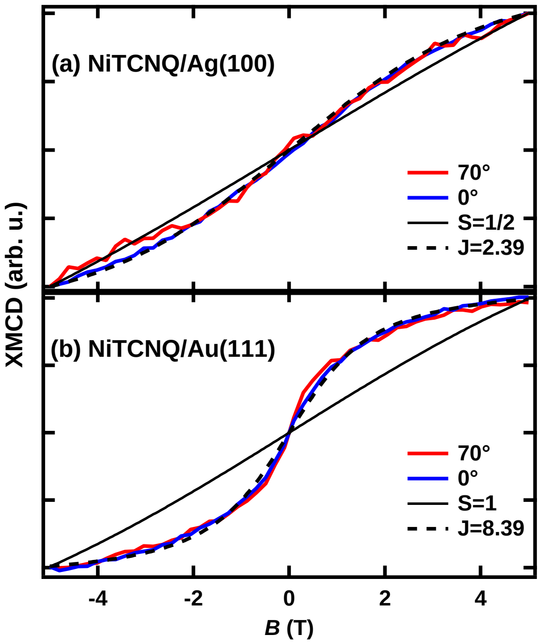

Figure 4.5: Magnetization curves for Ni-TCNQ structures on (a) Ag(100) and Au(111), respectively. The distinct s-shape is visible in both cases.

splitting in Ni-TCNQ/Au(111) is only due to the charge transfer from Ni to TCNQ molecules. This difference in the available charge-transfer channels further affects the magnetic properties of Ni-TCNQ networks, as will be discussed in the following.

The magnetization curves of Ni-TCNQ on Ag(100) and Au(111) are presented in Figure 4.5. In what follows the magnetization curves were obtained as the L_3 XMCD intensity normalized to XAS L_3 peak vs. magnetic field, all the curves were normalized to 1 at 5 T. For Ni-TCNQ on Ag(100) the slight s-shape of the magnetization curves suggests a weak ferromagnetic interaction between the Ni centers. Fitting the magnetization curves with the Brillouin function yields a total angular momentum J=2.39 at 8 K. This J value suggests the existence of an orbital magnetic moment since the highest possible spin moment value for a d^8, d^9 and d^{10} hybridized state would not exceed S=1. Analysis of the XMCD branching ratio consistently indicates an appreciable orbital magnetic moment at the Ni centers (cf. Table 4.1). The effect is even more pronounced for Ni-TCNQ on Au(111). Figure 4.6b shows significantly stronger s-shaped curve than would be expected for paramagnetic S=1 centers (black line). The fit with Brillouin function yields

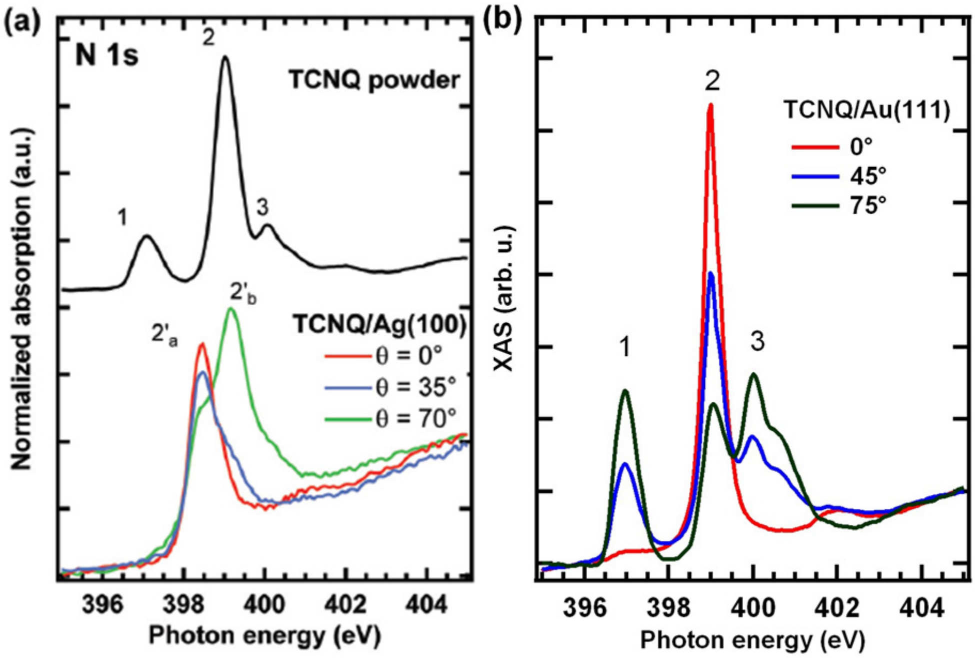

Figure 4.6: a) N 1s NEXAFS spectra of TCNQ on Ag(100) (adapted from Ref. [95]) and b) N K-edge XAS spectra of TCNQ on Au(111). On Ag(100), at submonolayer coverages of TCNQ molecules obtain charge from the substrate and NEXAFS spectra indicate coordination of the cyano groups to the substrate by splitting of peak 2. On the Au(111) surface, the lineshape of the N K-edge spectra strongly resemble that of TCNQ powder suggesting no or negligible charge transfer from the substrate.

unrealistic moment of J=8.39 (dashed line), which cannot be attributed to a sizable orbital moment. Therefore, we conclude that this shape of the magnetization curve is due to the ferromagnetic coupling of Ni centers.

Low-dimensional ferromagnetic behavior was reported previously for the bulk electrochemically synthesized Ni-TCNQ salts [100]. In this case authors argued that magnetism in the system is due to spin-spin interaction between paramagnetic Ni ions mediated by the diamagnetic TCNQ bridging ligands. As has been discussed above, in the Ni-TCNQ on Ag(100) the main charge transfer channel is from the substrate to TCNQ which then acts as a mediator of interaction between Ni centers. For the Ni-TCNQ on Au(111) two scenarios can be proposed. First, assuming that Au substrate acts as a passive support and coupling of adjacent Ni spins is through the TCNQ molecules (Figure 4.7), that is via superexchange mechanism. This mechanism has been proposed earlier for TCNQ-based magnets [94, 100]. Another possibil-

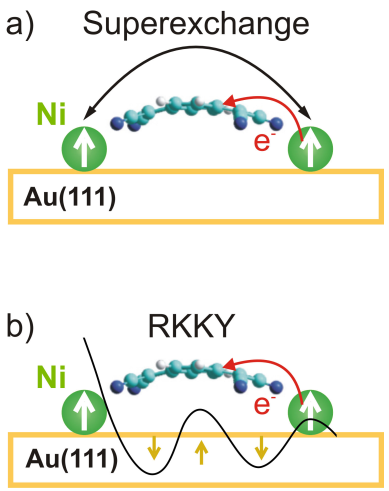

Figure 4.7: Possible coupling schemes for Ni centers in the Ni-TCNQ networks on Au(111): (a) superexchange interaction mediated by the organic ligands and (b) surface mediated RKKY interaction, where the ligand plays a role of the spacer.

ity is the surface mediated Ruderman-Kittel-Kosuya-Yoshida (RKKY, [101–103]) interaction, where the coupling between spins of Ni centers is through the conduction electrons of the Au(111) surface and TCNQ molecules act as a spacer. These two interaction mechanism cannot be discriminated based on XAS/XMCD or STM measurements alone. Further experiments, where the influence of the ligand size on the magnetic coupling are required. In this case TCNQ molecules can be substituted with closely related organic ligands, like e.g. TCNE. Recently, a variation in the coupling strength was reported for a closely related system of V-TCNE$_x$ on Ag(111), where Kondo effect quenching was shown for different molecule/vanadium arrangement, [104]. Alternatively, the mediator-role of the substrate can be eliminated by decoupling the Ni-TCNQ layer from the electron bath of the surface by e.g. introducing an insulating spacer layer.

4.2 Mn-TCNQ structures on Ag(100) and Au(111)

As we have seen in the previous section, properties of Ni-TCNQ networks on different surfaces undergo a significant variation. This conclusion, however, cannot be extended to any generic system as we will see in the following for the Mn-TCNQ structures supported on Ag(100) and Au(111).

Figure 4.8a and b shows the XAS spectra of Mn-TCNQ on Au(111) and Ag(100) recorded with linear light polarization (T=8 K, B=50 mT). Mn centers show pronounced multiplet structure suggesting the presence of localized atomic orbitals. The strong linear dichroism at the Mn L-edge signifies strong interaction between the Mn atoms and the TCNQ, which implies low-symmetry crystal field around the $3d$ shell of Mn atoms. XAS spectra with right (I^+) and left (I^-) circularly polarized light at the Mn $L_{2,3}$-edges for the Mn-TCNQ are shown on Figure 4.8e, f. The corresponding XMCD spectra ($I^- - I^+$) are shown as well. The XAS and XMCD spectra are compared with atomic multiplet calculations reported by van der Laan and Thole to determine the electronic configuration of Mn atoms. The XAS and XMCD lineshape for Mn-TCNQ on Au(111) suggest that the behavior of Mn centers is mostly governed by coordination to TCNQ. However, there is a close similarity to the d^5 configuration of Mn impurities on Cu(100) [95] which suggests that the d-shell electron occupation does not change upon coordination and is not dependent on the local environment. The magnetization curves recorded at the Mn $L_{2,3}$-edges at incident angles θ=0° and 70° after normalization are presented in Figure 4.9a and b, showing paramagnetic behavior of Mn centers. No anisotropy has been observed in either of these systems. The fitting of the magnetization curves with Brillouin function suggests a total angular momentum of J=5/2. The analysis of the XMCD branching ratio indicated small orbital moment, these results suggest that Mn centers in the Mn-TCNQ/Au(111) represent independent paramagnetic centers in the high-spin d^5 state, that is S=5/2. Unexpectedly, Ni centers have shown some orbital of L=0.2 which is probably due to some hybridization with d^4 and d^4 states. A similar behavior was found for the Mn-TCNQ/Ag(100), however, no orbital moment was found in this case (cf. Table 4.2). The slight deviation from the Brilloiun function in this case could indicate weak antiferromagnetic coupling between the adjacent Mn centers but could also be due to somewhat higher measurement temperature.

The nitrogen K-edge XAS spectra recorded with linearly polarized light for Mn-TCNQ networks on Au(111) and Ag(100) are shown in Figure 4.8(c)-(d). The presence of the two peaks indicates the strong Mn-cyano coordination and in the case of Ag(100) surface, also the substrate-cyano interaction. The strong dichroism in both cases is a result of the coordination to Mn, that is the molecular orbital corresponding to the peak for the in-plane polarization is more localized in the surface plane when cyano-groups coordinate to TCNQ. The zero XMCD intensity observed at the N-edge (not shown) indicates no orbital magnetic moment localized on the nitrogen atoms. Al-

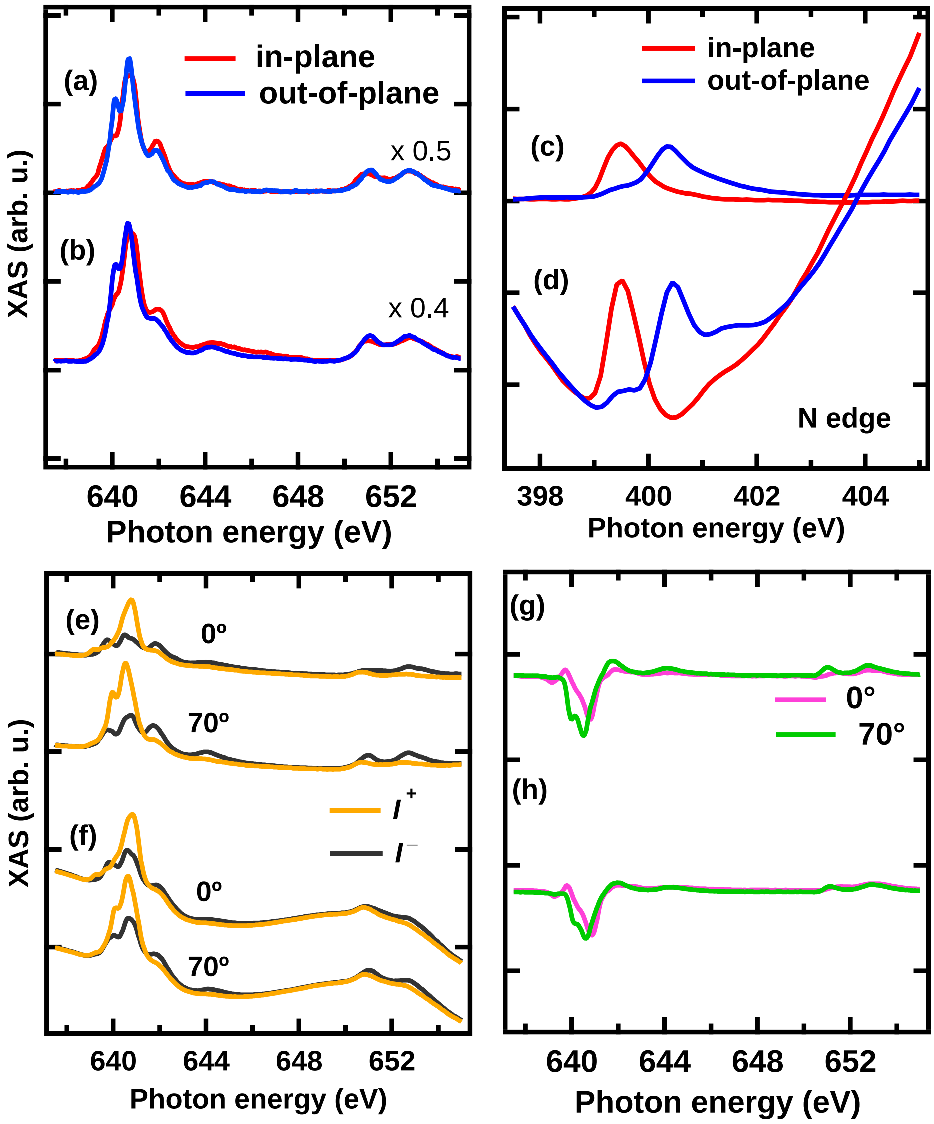

Figure 4.8: XAS and XMCD of Mn-TCNQ networks on Au(111)and Ag(100) (in all panels upper and lower spectra, respectively). (a)-(b) XAS for linearly polarized light parallel to the surface (in-plane) and 20° to the surface normal (out-of-plane) (T=8 K, B=50 mT). (c)-(d) XAS for linearly polarized light recorded at the nitrogen K-edge (T=8 K, B=50 mT). The lineshape indicates strong interaction between cyano groups and Mn centers, as well as with the substrate (in the case of Ag(100)). (e)-(f) Circularly polarized XAS at 0° (normal) and 70° (grazing) incidence and (h)-(g) corresponding XMCD spectra (T=8 K, B=5 T).

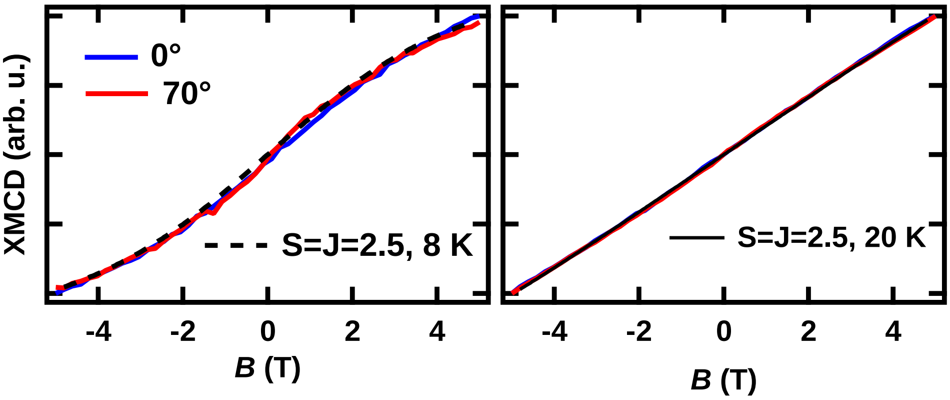

Figure 4.9: Magnetization curves obtained as the Mn L_3 intensity at T=8 K for the Mn-TCNQ networks on (a) Ag(100) and (b) Au(111) surfaces. Fitting with Brillouin function yields a spin magnetic moment of $S = 5/2$ for Mn centers in both cases.

though information about spin magnetic moment is not available from the nitrogen K-edge spectra, the absence of orbital magnetic moment indicates that TCNQ represents a closed-shell system in which all electrons are paired due to the charge transfer from the Mn atoms. If this is so, then it perhaps partly explains the absence of magnetic coupling between the Mn centers since TCNQ molecules do not mediate the spin coupling. The other reason could be the strong Mn-substrate coupling, which is not eliminated even upon coordination to TCNQ or a relatively long distance between Mn centers.

Figure 4.8a-b and e-h shows the XAS/XMCD recorded at the Mn $L_{2,3}$-edges for Mn-TCNQ networks on Au(111) and Ag(100). As can be seen the spectra strongly resemble each other, despite the different local environment. The XAS spectra recorded with the linearly polarized light 4.8a-b show strong anisotropy which signifies the formation of strong coordination bonds to the TCNQ molecules on the both substrates. As we have seen

θ	S_{eff}		L	
	I	**II**	**I**	**II**
0°	1.56	2.29	0.087	0.25
70°	1.41	2.52	0.083	0.24

Table 4.2: Spin and orbital moments for MnTCNQ on Ag(100)(**I**) and on Au(111) (**II**) as calculated using sum rules.

in the previous section, the change in the local environment and influence of the ligand field are reflected in the variation of the lineshape and peak intensities. Here, however, spectra strongly resemble each other. From the coordination structure point of view Mn-TCNQ networks on Ag(100) and Au(111) are similar. Since the XAS resonances are directly related to the electronic properties, this similarity can be interpreted as an inherent property of the Mn centers. A comparison of the STM images of Mn-TCNQ structures on Au(111) and Ag(100), Figure 4.2 shows that Mn centers in the both cases appear as depressions, thus it can be concluded that there is a strong correlation between XAS observations and STM contrasts. This is reasonable since both of them are directly or indirectly associated with electronic properties.

Figure 4.8 shows the XMCD $L_{2,3}$-edge spectra of Mn-TCNQ on Au(111) and Ag(100). Again, there is a strong similarity between the two. The analysis of the XAS/XMCD spectra for Mn-TCNQ/Ag(100) system suggests that Mn centers are in high-spin d^5 state with a very weak spin coupling. This close similarity of the spectra on Ag(100) and Au(111) is quite surprising, since as we have seen in the previous section for the Ni-TCNQ networks on these surfaces, properties varied significantly from one substrate to the other. Besides, we have seen that charge transfer for TCNQ on the two surfaces is different, that is on Au(111) no charge transfer from the surface to the molecules was found, while molecules are charged on Ag(100).

4.3 Conclusions

Structure and magnetic properties of Mn-TCNQ and Ni-TCNQ networks on Ag(100) and Au(111) were studied using STM, XAS and XMCD. To directly trace the changes upon coordination XAS/XMCD studied were performed for metal impurities and TCNQ molecules separately on each surface. For the TCNQ deposited on Ag(100) significant deviation from the TCNQ powder spectrum was found indicating the charge transfer from the substrate to the molecules. To the contrary, XAS spectra for TCNQ on Au(111) have shown marked similarity to the powder spectrum suggesting that molecules remain neutral on this surface. Ni impurities were found to strongly hybridize with surface states on both substrates and assume a spin-quenched mixed valence state.

However, upon coordination to TCNQ Ni centers recover their magnetic moments. The lineshape suggests mixed valence configuration with d^8 and d^9 character. The square-planar geometry resulted in the anisotropic XAS and XMCD. The spectra features are different from the Ni adatoms with more pronounced L_2 edge and a fine structure at L_3. A sharp multiplet structure was observed for Mn-TCNQ networks on Au(111) as well. The spectra lineshape suggests d^5 configuration. The lineshape of XAS and XMCD was found to be very similar to those of the Mn-TCNQ networks on Ag(100). The sum-rule analysis indicated the presence of an orbital magnetic moment for the Mn-TCNQ structure on Au(111), while Mn-TCNQ/Ag(100) have shown zero orbital moment.

The magnetization curves for Mn-TCNQ networks on the both substrates were shown to closely follow the Brillouin fit with S=5/2 suggesting that Mn centers behave like paramagnetic spins. Although, a small deviation from the fit can be seen, which might be suggestive of weak antiferromagnetic coupling but could be the result of somewhat higher measurement temperature. For Ni-TCNQ structures well-pronounced s-shaped magnetization curves were found, which cannot be fit with S=1 (on Ag(100)) and S=1/2 (on Au(111)). This is interpreted as a clear sign of ferromagnetic coupling with the effect being stronger for Ni-TCNQ structures on Au(111). It cannot be attributed to the sizable orbital moment neither can it be due to magnetic anisotropy. The results reported in the section 4.1 allowed us to propose two coupling schemes for Ni centers in the Ni-TCNQ networks on Au(111). Knowing that pure TCNQ acquires no charge from the substrate, the interaction between Ni centers is proposed to be mediated by the TCNQ ligands, that is via superexchange mechanism. However, the fact that TCNQ remains neutral does not completely exclude another coupling scheme, where interaction is mediated by the surface by means of RKKY interaction. In this case TCNQ ligands act as a spacer. Further experiments have to be put forward to discriminate between the proposed mechanisms. For example, the closely related shorter TCNE ligand can be used to validate the RKKY coupling scheme. Alternatively, an insulating layer can be introduced to check the mediator role of the substrate.

Chapter 5

Controlled Synthesis of Carbon-based Nanostructures on Surfaces

Particular physical and chemical properties of carbon based nanomaterials (CBNs)[105] were shown great applications in manufacturing various nanodevices such as electron field emitters, sensors, one-dimensional conductors, supercapacitors, reinforcing fibres, hydrogen storage devices, and catalyst support for fuel cell electrodes. Despite these amazing technical progresses, many challenges still remain in the development of synthesis methods suitable for commercial applications and fabricating novel functional nanostructures with well-defined architecture.

This chapter details the investigations toward the controlled on-surface synthesis of fullerenes, graphene nanoribbons (GNRs) and carbon nanotube (CNTs) from well-defined organic precursors by means of surface supported/ catalyzed cyclodehydrogenation (SCCDH) reaction. This synthesis path offers a greater control over the CBN formation process as opposed to the standard synthesis/production methods which will be reviewed in the following.

Fullerenes represent a unique class of close-cage molecules entirely composed of carbon. Since the discovery of the most famous member of the fullerene family, C_{60}, in 1985 [106] much research has been focused on the synthesis and the remarkable properties of fullerenes. Most effort was dedicated to the properties of C_{60} for which the production method is well established. The first method used laser induced vaporization of grpahite in an inert atmosphere, but this produced microscopic amounts of fullerenes. In 1990, a new type of apparatus using an arc discharge to vaporize graphite was developed in Germany by Krätschmer and Huffmann[107].

In essence, the chamber is filled with He at 100 Torr, then high voltage is applied to one of the graphite electrodes for a short time (typically, 10-15 seconds) to produce a black, soot-like material (fullerene soot). About 10% of the fullerene soot is C_{60}, 2-3% is C_{70}, and the higher fullerenes constitute some trace amounts. Besides the low yield, production of higher fullerenes by the arc-discharge method encounters purification issues as well, for example it has been shown that two major isomers of C_{84} cannot be separated even after 20 rounds of recycling high-performance liquid chromatography [108]. Therefore, synthetic methods are needed that will produce a single isomer of a desired fullerene, free from impurities of other isomers or fullerenes of different sizes.

A promising route to achieve this goal for the selective synthesis of fullerenes is based on planar polycyclic aromatic hydrocarbon precursor molecules that already contain the carbon framework required for the formation of the target fullerene cage. Such an unfolded fullerene can be stitched up through the intramolecular cyclodehydrogenation to form the desired fullerene isomer. The flash vacuum pyrolysis (FVP) technique has been found to be an effective approach to carry out such intramolecular cyclization. Many small curved fullerene fragments have been obtained by this method[109–112]. However, the yield of the target fullerenes is still too low for preparative synthesis. C_{60}, for instance, has been obtained with 0.1-1% yield [113], whereas higher fullerenes were only detected in trace amounts by mass spectrometry[114, 115].

The first step towards the controlled synthesis of non-planar carbon nano-structures on a surface was made by Rim *et al.*,[38] where the formation of carbon half-spheres (so called bucky-bowls) from planar precursor molecules has been demonstrated to take place on Ru(0001) surface. The method utilized surface-catalysed cyclodehydrogenation (SCCDH) exhibits a high selectivity of the dehydrogenation due to the catalytic activity of the surface and a high conversion ratio of the deposited precursors into non-planar cap structures.

Recent work by Otero et al.[39] has demonstrated the efficiency of this SCCDH method for the synthesis of C_{60} fullerene cages. In this study, precursor molecules $C_{60}H_{30}$ and $C_{57}N_3H_{30}$ were deposited onto a Pt(111) surface under ultra-high vacuum conditions and annealed at 750 K. The surface acts as a support for the precursors and final products, allowing for scanning tunnelling microscopy (STM) investigations at the single molecule level. Moreover and importantly the surface serves also as a catalyst for the SCCDH reaction. A simple annealing step led to the formation of the corresponding C_{60} and $C_{57}N_3$ cages with an unprecedented high relative yield. Despite of the variety of experimental and theoretical methods employed to character-

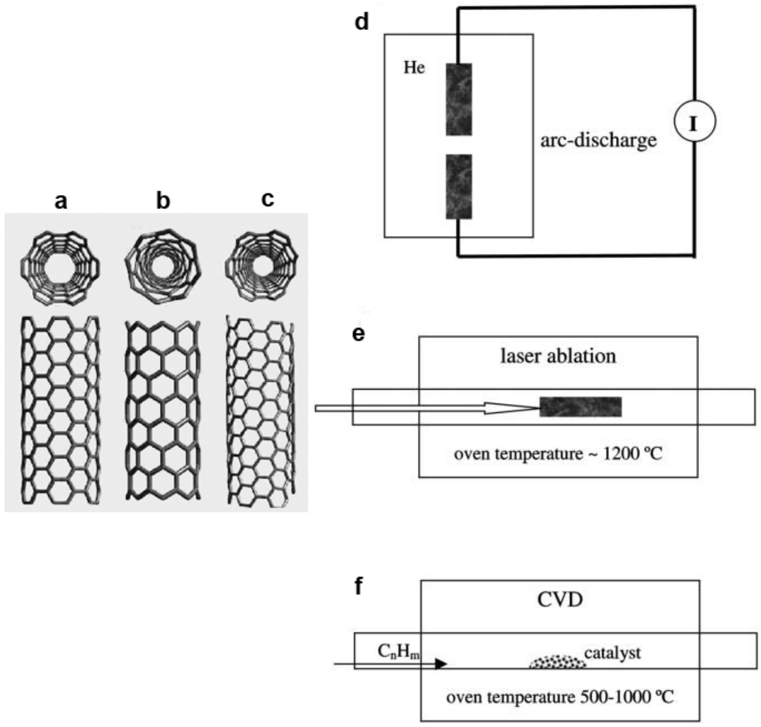

Figure 5.1: Carbon nanotubes exist in three different forms: a) armchair, b) zigzag and c) chiral, which can be produced using d) arc-discharge, e) laser ablation and f) CVD growth.

ize the process, the particular stability of the C_{60} target molecule prevented to demonstrate the selectivity of the C-C bond formation process. In this case it cannot be excluded that C-C bonds rearrange to form the most stable compound, the C_{60} I_h isomer.

In section 5.1 this important question will be addressed by studying the SCCDH process of specifically designed precursor molecules. It is shown that the reaction occurs indeed in a selective manner and that only correctly programmed precursors yield the desired molecule. Namely, it is shown that SCCDH process does not involve C-C bond rearrangement and cage formation proceeds via dehydrogenation and zipping of newly formed bonds at preselected positions only. Based on this result the synthesis of the higher fullerene C_{84} will be demonstrated.

Carbon nanotubes (CNTs) can be produced using arc-discharge, laser ablation and Chemical Vapor Deposition (CVD). In arc-discharge, carbon atoms are evaporated by plasma of helium gas ignited by high currents passed through opposing carbon anode and cathode, quite in the same manner as was discussed before for the fullerenes. Arc-discharge has been developed into an excellent method for producing both high quality multi-walled nanotubes (MWNTs) and single-walled nanotubes (SWNTs). MWNTs can be obtained by controlling the growth conditions such as the pressure of inert gas in the discharge chamber and the arcing current. MWNTs produced by arc-discharge are very straight, indicative of their high crystallinity. For as grown materials, there are few defects such as pentagons or heptagons existing on the sidewalls of the nanotubes. The by-product of the arc-discharge growth process are multi-layered graphitic particles in polyhedron shapes. Purification of MWNTs can be achieved by heating the as grown material in an oxygen environment to oxidize away the graphitic particles [116]. The polyhedron graphitic particles exhibit higher oxidation rate than MWNTs; nevertheless, the oxidation purification process also removes an appreciable amount of nanotubes. For the growth of single-walled tubes, a metal catalyst is usually introduced into the arc-discharge system.

CVD is a common method for the commercial production of carbon nanotubes. For this purpose, the metal nanoparticles are mixed with a catalyst support such as MgO or Al_2O_3 to increase the surface area for higher yield of the catalytic reaction of the carbon feedstock with the metal particles. One issue in this synthesis route is the removal of the catalyst support via an acid treatment, which sometimes destroys the original structure of the carbon nanotubes. However, alternative catalyst supports that are soluble in water have proven effective for nanotube growth [117].

Of the various means for nanotube synthesis, CVD shows the most promise for industrial-scale deposition, because of its price/unit ratio, and because CVD is capable of growing nanotubes directly on a desired substrate, whereas the nanotubes must be collected in the other growth techniques. The growth sites are controllable by careful deposition of the catalyst. In 2007, a team from Meijo University demonstrated a high-efficiency CVD technique for growing carbon nanotubes from camphor [118]. Researchers at Rice University, until recently led by the late Richard Smalley, have concentrated upon finding methods to produce large, pure amounts of particular types of nanotubes [119]. Their approach grows long fibers from many small seeds cut from a single nanotube; all of the resulting fibers were found to be of the same diameter as the original nanotube, however it still has to proven that the type of the resultant CNTs is the same as the original nanotube. Nonetheless, it represents the first attempt towards controlled, size and chirality selective growth of the nanotubes, an alternative to this method will be presented in the Section 5.2.

GNRs are essentially thin strips of graphene whose electronic properties strongly depend on their width and edge-structure the latter one being either of zig-zag, armchair or chiral type. Recent DFT calculations show that armchair and zig-zag GNRs are semiconducting with the gap being dependent on the GNR width. Additionally, zig-zag GNRs are predicted to have spin-polarized edges [120–125].

On the experimental side, only the questions of width-dependent electrical conductivity of generic GNRs were addressed so far, as the production of long ∼1μm nanoribbons suitable for transport measurements with well-defined edge remains a challenge. Several methods to produce well-defined GNRs were suggested:

- Chemical methods include etching with thermally activated metal nanoparticles [126], a bottom-up synthesis using Suzuki-Miyaura coupling in solution [127] and aerosol pyrolisis process [128];
- Sonochemical [129];
- Lithographic [124, 130];
- Unzipping of carbon nanotubes using Ar-etching [131–134].

However, reliable production of graphene nanoribbons smaller than 10 nm in width with chemical precision remains a significant challenge. Recently, Cai *et al.* [41] reported a method consisting of utilizing the dibromo-dianthracene precursor molecules which are thermally activated to debrominate and form a polymer, and then submitted to cyclodehydrogenation step via annealing to produce nanoribbons. This method has the advantage of producing nanoribbons of very precise width but has its drawbacks too. The nanoribbon length is limited to 50 nm, and the width cannot be tuned. Here we apply a similar method of the surface supported synthesis to produce nanoribbons using polyarenes. Compared to anthracenes polyphenylenes have the advantage of the width-tunability, but show poorer connectivity. This issue and the details of growth will be addressed in the section 5.3.

5.1 Controlled fullerene synthesis via SCCDH reaction

The cyclodehydrogenation process used here consists of the following steps: first, the designated precursor molecules are deposited by organic molecular beam epitaxy onto the surface. Second, the sample is annealed to the required temperature to induce the surface assisted reaction resulting in the aforementioned partially and fully closed-cage molecules.

Figure 5.3 shows the precursor molecules employed in this study. Be-

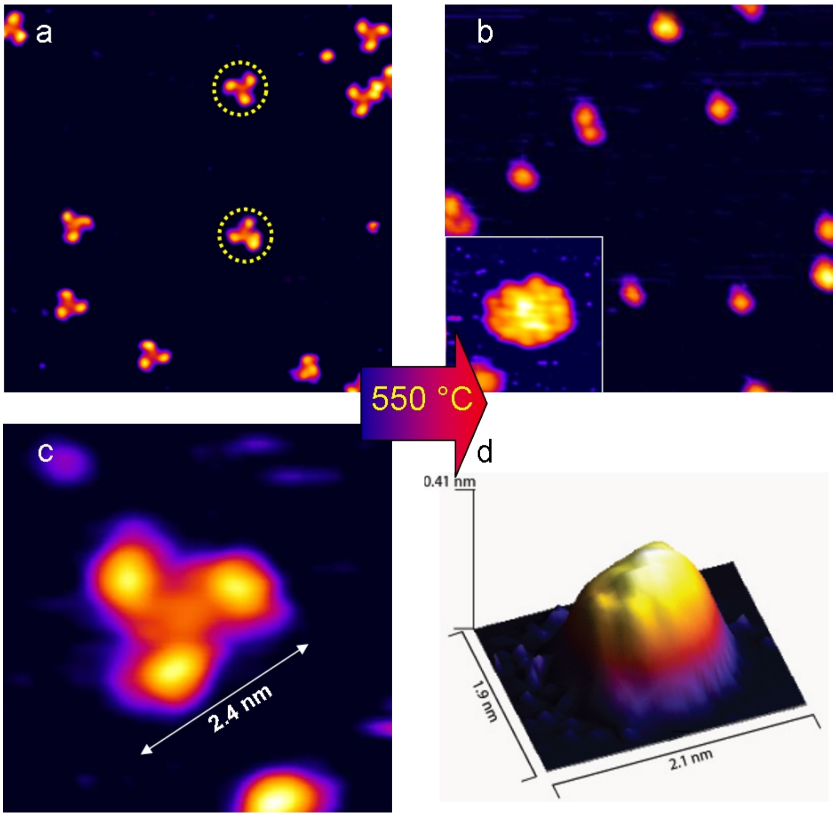

Figure 5.2: STM images of C_{84} cyclization process: a) and c) 25×25 nm^2 and 4×4 nm^2 images of Pt(111) after deposition of $C_{84}H_{42}$; b) and d) after annealing at 820 K; inset in b) shows 3×3 nm^2 image of C_{84} where submolecular structure is resolved.

sides the C_{60} precursor $C_{60}H_{30}$ (**1**) that was also used in the study by Otero and co-workers, we synthesized a modified $C_{60}H_{30}$ (**2**) precursor to verify the selectivity of the reaction. The molecule **3** ($C_{84}H_{42}$) is the precursor for the C_{84}(20) fullerene.

The molecules presented in Figure 5.3a-c are composed of hexagon and pentagon rings, terminated by hydrogen atoms at the periphery. The thin lines connecting the outer carbon atoms show the C-C bonds to be formed upon dehydrogenation. The desired products are shown in Figure 5.3d-f where all necessary C-C bonds have been formed as indicated for the precursors in Figure 5.3a-c without further C-C bond rearrangements.

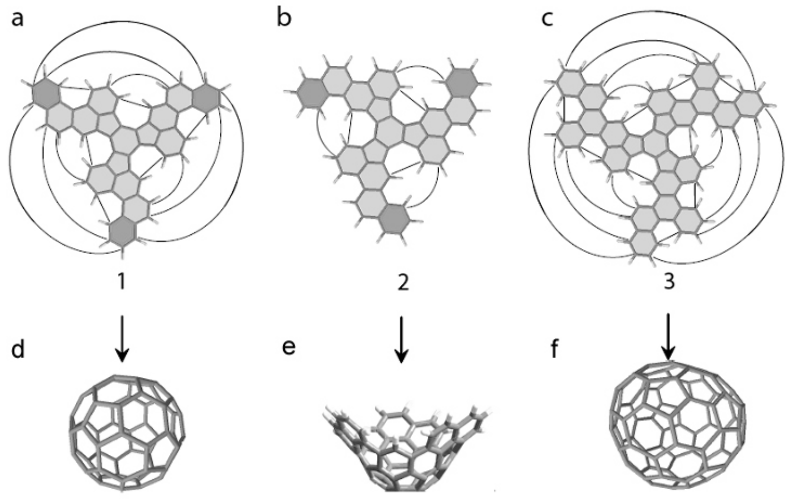

Figure 5.3: Structures of the precursor molecules and their condensation products. a)-c), Precursor molecules used: a) C_{60} precursor $C_{60}H_{30}$ 1; b) modified $C_{60}H_{30}$ 2; c) $C_{84}H_{42}$ 3. The lines mark the C-C bonds that form upon cyclodehydrogenation. d)-f), Expected products after the cyclodehydrogenation: e) C_{60} fullerene; f) nanotetrahedron; g) C_{84} fullerene.

5.1.1 STM studies of the fullerene formation via SCCDH on Pt(111)

Figure 5.5 summarizes our results of the STM investigations for precursors **1** and **2**. Measurements of the C_{60} formation from the precursor **1** were performed in order to directly compare the results with the modified $C_{60}H_{30}$ isomer **2**. Upon deposition on Pt(111) precursor **1** is imaged as a triangular protrusion as shown in Figure 5.5a. After annealing at 750 K the SCCDH reaction is completed and all molecules transform into round C_{60} fullerenes with an apparent height and width of 0.4 nm and 1.5 nm, respectively (Figure 5.5b). These dimensions are in accordance with ref.[39] and previously reported values for C_{60} on Pt(111) and Pd(110)[135, 136]. Although these observations indirectly point towards the C_{60} formation, it has still to be demonstrated that bond formation follows the selective zipping mechanism, in which only preselected C-C bonds are formed.

In order to show the selectivity of the SCCDH and rule out the possibility of C-C bond rearrangement we synthesized the precursor molecule **2**, see Figure 5.3b, which has the same chemical formula and a very similar structure. In contrast to the C_{60} precursor molecule **1**, it has three of its benzene rings shifted to a different position as indicated in Figure 5.3a-b by the shaded

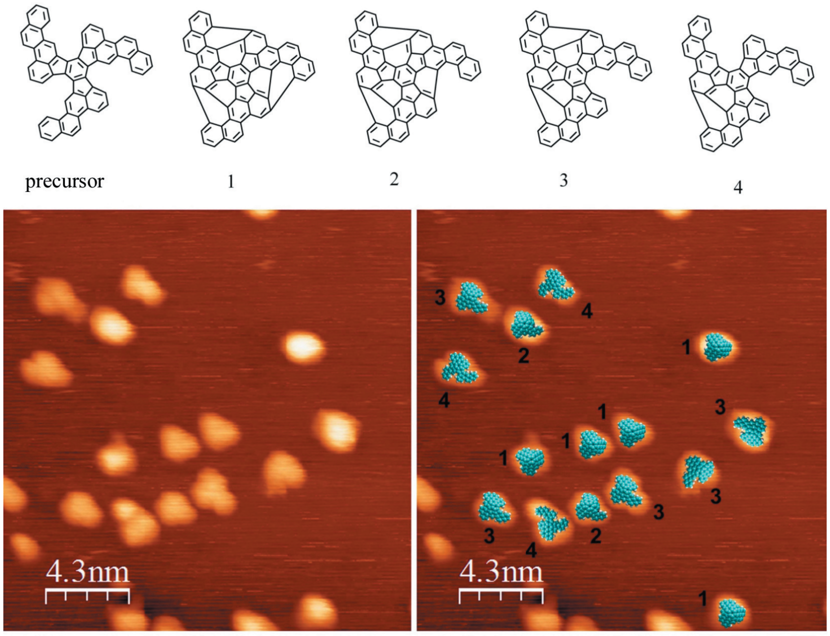

Figure 5.4: Precursor **2** after annealing at 750 K for 2 minutes: a) unfolded precursor and tentative scheme of partially folded molecules to explain the diversity of species. b) Molecules as observed by STM; c) overlay of tentative models onto an STM image.

hexagons. The possible folding paths are shown in Figure 5.3a-b by the thin lines. The repositioning of the benzene rings prevents some folding steps essential to the fullerene formation, thus, the folding should lead to structurally different species. As depicted in Figure 5.3f folding of **2** is expected to yield an open-cage structure which we refer to as nanotetrahedron.

STM analysis of a partially covered surface ($\sim$ 0.2 monolayer) clearly shows the individual planar molecules exhibiting a three-blade propeller shape with a width of approximately 2.1 nm and an apparent height of 0.14 nm (Figure 5.5c). The molecule is prochiral and STM images show that in fact there are two 2D-enantiomers on the surface (Figure 5.5c, yellow dashed circles). The shape and size of the molecules with three distinct lobes confirm that the molecules remain intact during the thermal evaporation process. The structure of this precursor molecule was designed in such a way that upon folding it forms a tetrahedral shaped molecule which should be easily distinguishable by STM as they are lower and wider than C_{60}. After annealing at 750 K for 2 minutes the shape of the molecules changes and STM reveals various species which we ascribe to intermediate states of the

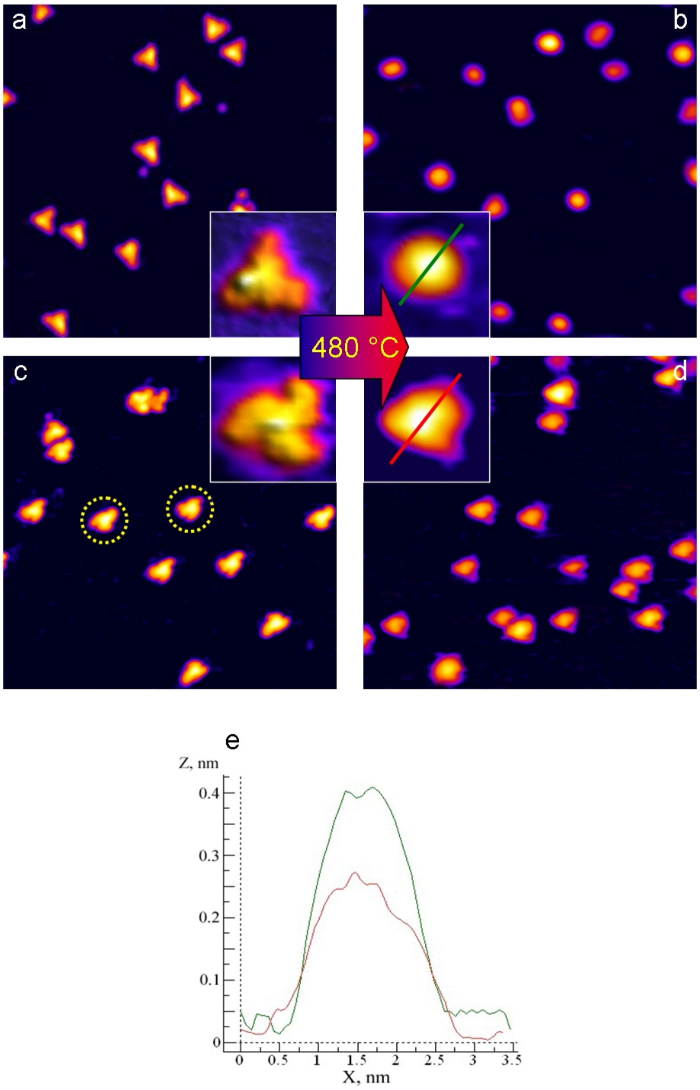

Figure 5.5: STM images of C_{60} cyclization process: a) 25×25 nm^2 image of Pt(111) after deposition of precursor **1** and b) after annealing at 750 K; c) 25×25 nm^2 image of Pt(111) after deposition of precursor **1**, yellow dashed circles showing the two 2D-enantiomers of **2** d) 25×25 nm^2 area of the same surface after annealing at 750 K for 10 min. Insets in a), b), c) and d) are of 3×3 nm^2 in size. e) Superposition of line scans in the insets of b) and d) (green and red lines respectively), showing that after annealing modified precursor **2** yields species of lower apparent height (red curve) compared to precursor **1**.

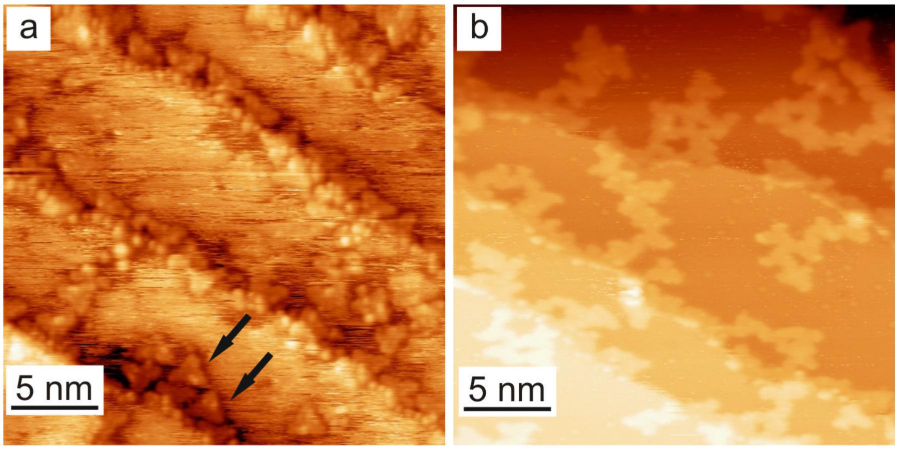

Figure 5.6: images of $C_{60}H_{30}$ on Cu(100): a) as deposited; b) after annealing at 650 K.

partially dehydrogenated and folded molecules (Figure 5.4). Upon annealing at 750 K for 10 minutes the cyclization process is completed as evidenced by Figure 5.5d, showing full conversion into triangular species, all having similar size and shape.

The molecules are imaged as triangular protrusions suggesting that the rim is in contact with the platinum surface. Such a configuration would be favorable considering the formation of strong C-Pt bonds. The apparent height of the final product is ca. 0.28 nm and the base width is about 1.8 nm as opposed to 0.4 nm and 1.5 nm for C_{60} produced from precursor **1** after annealing at 750 K (see Figure 5.5e for comparison). These parameters indicate that although the nanotetrahedra precursor has all the necessary C atoms to form C_{60} and similar structure to precursor **1**, annealing at 750 K results in the formation of a structurally different species as no C-C bond rearrangement occurs during the annealing. On the other hand, the observation of intermediate products along with final products is giving support to the zipper mechanism of the reaction, where only preselected bonds are formed. Therefore we conclude that the SCCDH process is selective in nature and it can further be used to produce specifically designed carbon based nanostructures.

Once the possibility of C-C rearrangement is ruled out, the SCCDH method opens up new horizons in the synthesis of carbon nanostructures. As an example we demonstrate here the efficient synthesis of the higher fullerene C_{84}. The structure of the $C_{84}H_{42}$ precursor molecule is shown in Figure 5.3c. The molecule is imaged as three distinct bright lobes with a width of 2.4 nm and height of 0.14 nm, confirming that the molecule does not decompose during evaporation (Figure 5.2a, c). The model of $C_{84}H_{42}$ (Figure 5.3c) shows that the molecule is prochiral and adsorption on the surface leads to two distinct chiral forms (Figure 5.2a, yellow dashed circles). This, however, does not affect the reaction path as the zipping mechanism for both of these forms is the same (Figure 5.3c, thin lines).

After annealing to 820 K the shape of all the molecules changes and becomes spherical with a lateral size of ca. 1.7 nm and an apparent height of 0.42 nm as evidenced by STM (Figure 5.2b,d). The lateral size of the newly formed molecules is larger and the apparent height is lower compared to the free C_{84} fullerene (van der Waals diameter obtained from DFT calculations is approx. 1.2 nm). This might be due to the imaging process but could also indicate that as a result of strong adsorbate-substrate interactions the molecules on the surface undergo relaxations, i.e., they probably maximize the number of bonds with the surface by deformation of the cage. Furthermore, these interactions could lead to the modification of the underlying surface. These effects were observed for C_{60} after annealing on various substrates including Pt(111)[135–137] as well as for an isomeric mixture of C_{84} on Si(111)-7 × 7 (apparent height 0.59 - 0.69 nm),[138, 139], where the molecule-substrate interaction is considered to be weaker compared to the Pt(111) surface (see ref. [138] and references therein). As shown in Figure 5.2b, the molecules are imaged as featureless spherical species, but under certain conditions, such as with an adsorbate on the tip, the intramolecular structure is resolved (Figure 5.2b, inset). The structure is similar to that observed for the C_{84} isomeric mixture [139] and suggests a p-electron system decoupled from the substrate. Since the possibility of C-C bond rearrangement was excluded by the experiments with precursor **2** we therefore assume that the newly formed molecule is the $C_{84}(20)$ fullerene. It is important to note that the required annealing temperature for the C_{84} synthesis is higher than that for C_{84}, which we ascribe to the larger precursor size which does require the breaking of more C-Pt bonds during the cyclization.

The structure of the products cannot be directly inferred from the STM images. In addition, the minute amount of material (ca. 10^{12} molecules/cm^2) and strong surface bonding prevents further analysis by other standard structure sensitive methods. However, the formation of nanotetrahedra from the modified $C_{60}H_{30}$ precursor represents strong evidence against the occurrence of C-C rearrangements in such systems. Theoretical studies show that the Stone-Wales defects and C-C rearrangement for fullerenes and carbon nanotubes would require 1520 K even in the presence of a catalyst which usually leads to a significant reduction of the activation temperature [140, 141]. Under the employed conditions it is therefore very unlikely that these processes accompany the folding on Pt(111) (only upon annealing to 990 K conversion of bucky-bowls into a planar carbon layer is observed). The surface selectively catalyses the dehydrogenation reaction and together with the demonstrated selectivity of the C-C bond formation the only possibility left is the formation of a single product where the structure is defined by the precursor molecules, hence isomer specific species are very likely formed.

The STM experiments show that the conversion ratio of the planar precursor molecules **1**, **2**, **3** into the corresponding fullerene and open cage structures is nearly 100 %, i.e., no desorption occurs during the annealing and that all planar precursors transform into non-planar structures. The variation in the shape and size distribution of the products is related to many different possible adsorption geometries and potential surface modification below the products. These findings demonstrate that the SCCDH method represents a very efficient path towards the synthesis of fullerenes and related molecules such as open cage structures, hetero- and endofullerenes. There is essentially no limitation for the variety of organic non-planar target molecules that could be derived by this retrosynthetic approach. The procedure could be extended to the fabrication of carbon nanotubes with well-defined diameter and chirality since the buckybowls can be viewed as a seed for carbon nanotubes using chemical vapour deposition. Besides the obvious advantages of the SCCDH synthesis method, there are some limitations. First, it can only be applied in a well-defined temperature interval. Our results show that the annealing temperature required for completing SCCDH increases with the number of the C atoms in the precursor molecule, i.e., 750 K for 1 and 2 and 820 K for 3, respectively. On the other hand, annealing to sufficiently high temperatures of about 990 K leads to complete C-C rearrangement and subsequent decomposition of all the carbon structures into a planar adlayer similar to that grown by CVD on different substrates[142, 143]. These facts signify that only a small temperature window exists for each specimen where the SCCDH can be applied and that the SCCDH process on Pt(111) for high-mass fullerenes might be difficult to achieve. Therefore appropriate substrates have to be explored for the efficient conversion of precursor molecules to the desired carbon nanostructures. Such substrates could be based on platinum group metals (Ru, Rh, Pd, Os, Ir and Pt) since they are generally considered as good catalysts for hydrogenation or dehydrogenation reactions [144].

Control measurements for the C_{60} cyclization by Otero *et al.* on Au(111) surface have shown only very little fullerene formation. In order to elucidate the role of the catalytic properties of the substrate we performed measurements on Cu(100) where the molecule-substrate interaction is stronger than on Au(111) but significantly weaker compared to Pt(111)[138, 145]. The STM measurements demonstrate that molecules aggregate at the step-edges of Cu(100) indicating that they were mobile on the surface. After annealing to 650 K stable islands of randomly merged triangular shaped molecules evolve (see Figure 5.6). After annealing to 750 K, fuzzy mobile features were seen but no fullerene formation was observed. This contrasts with the results on the Pt(111) where the molecules did not form islands at similar temperatures. It thus indicates that the thermal induced diffusion prevents the cage closing since it is likely that adjacent molecules form C-C bonds between them, thereby stabilizing the random aggregates. Thus, a low coverage of precursor molecules has to be employed also on the Pt(111) surface to avoid interlinking of neighbouring molecules. On the other hand, the strong molecule-substrate interaction is required for the successful completion of the SCCDH process. Indeed, the STM observations of immobile molecules and Time of Flight Secondary Ion Mass Spectrometry (discussed in the following) data indicate that this is the case for Pt(111) substrate.

5.1.2 SCCDH reactions studied with ToF-SIMS

The strong bonding of the molecules to the substrate is confirmed by our Time-of-Flight Secondary-Ion-Mass-Spectroscopy (ToF-SIMS) investigations as well, Figure 5.7. The findings show that C_{60} deposited onto the Pt(111) substrate at room temperature exhibits a C_2-loss pattern characteristic for C_{60} powder in ToF-SIMS [146] or laser ablation [106] experiments, Figure 5.7a. Annealing of C_{60}/Pt(111) to 750 K results in the intensity reduction of these peaks but the C_2-loss pattern in preserved, Figure 5.7b. To mimic the conditions at which C_{60} is formed from the $C_{60}H_{30}$ upon annealing, we deposited C_{60} onto platinum at 750 K following the procedure by Otero et al. Indeed, the STM images show that C_{60} molecules deposited onto room temperature Pt(111) substrate assemble into islands and annealing does not change this structure. Images after deposition onto the substrate at 750 K reveal randomly distributed molecules resembling $C_{60}H_{30}$ after annealing. The ToF-SIMS peak-pattern in the case of C_{60} deposited onto Pt(111) at 750 K represents a number of C_xPt_y peaks of various intensities (cf. Figure 5.7e), the C_{60} peak is present but is relatively small. ToF-SIMS spectra for $C_{60}H_{30}$/Pt(111) show a characteristic series of $C_{60}H_{30}Pt_x$ peaks as shown on Figure 5.7c. This pattern disappears after annealing to 750 K and the spectrum closely resembles the one for C_{60} deposited onto the hot Pt(111) surface, compare spectra on Figure 5.7 d and e. This indicates that the binding of the molecules to the substrate is strong and dramatically affects the ionization cross-section of the molecules in the ToF-SIMS experiments. STM measurements on the analogous system [39] show that C_{60} molecules

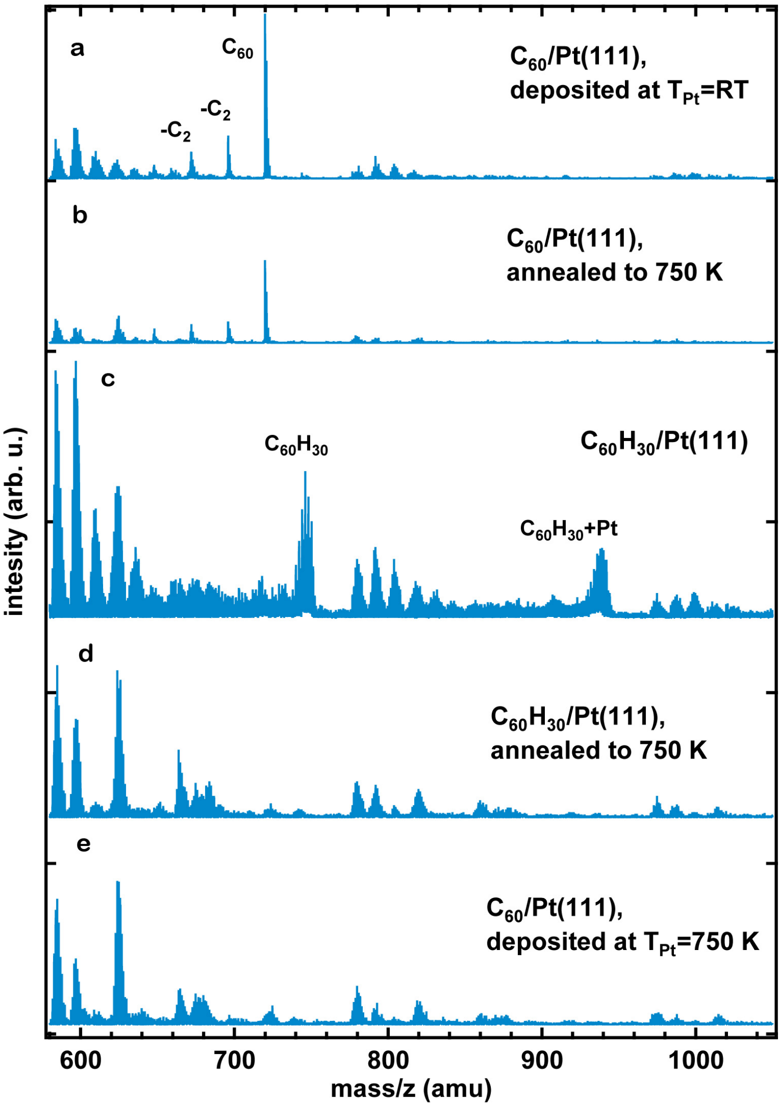

Figure 5.7: ToF-SIMS spectra of C_{60} and $C_{60}H_{30}$ on Pt(111) in positive ion mode: a)C_{60} deposited onto Pt(111) held at RT. Characteristic m/z=720 peak (marked) as well as the C_2-peaks are clearly visible. The same system annealed to 750 K for 5 min (b) shows the same pattern , however with marked intensity reduction of all peaks. c) $C_{60}H_{30}$ deposited onto Pt(111), shows main m/z=750 peak and its replica peak corresponding to $C_{60}H_{30}$+Pt. The spectrum after annealing of this system to 750 K (d) is very similar to that of C_{60} deposited onto Pt(111) held at 750 K. All spectra were normalized to Pt (m/z=196) peak.

remain intact and no decomposition occurs at this temperature.

The same conclusion holds for C_{84} and its precursor $C_{84}H_{42}$ for the

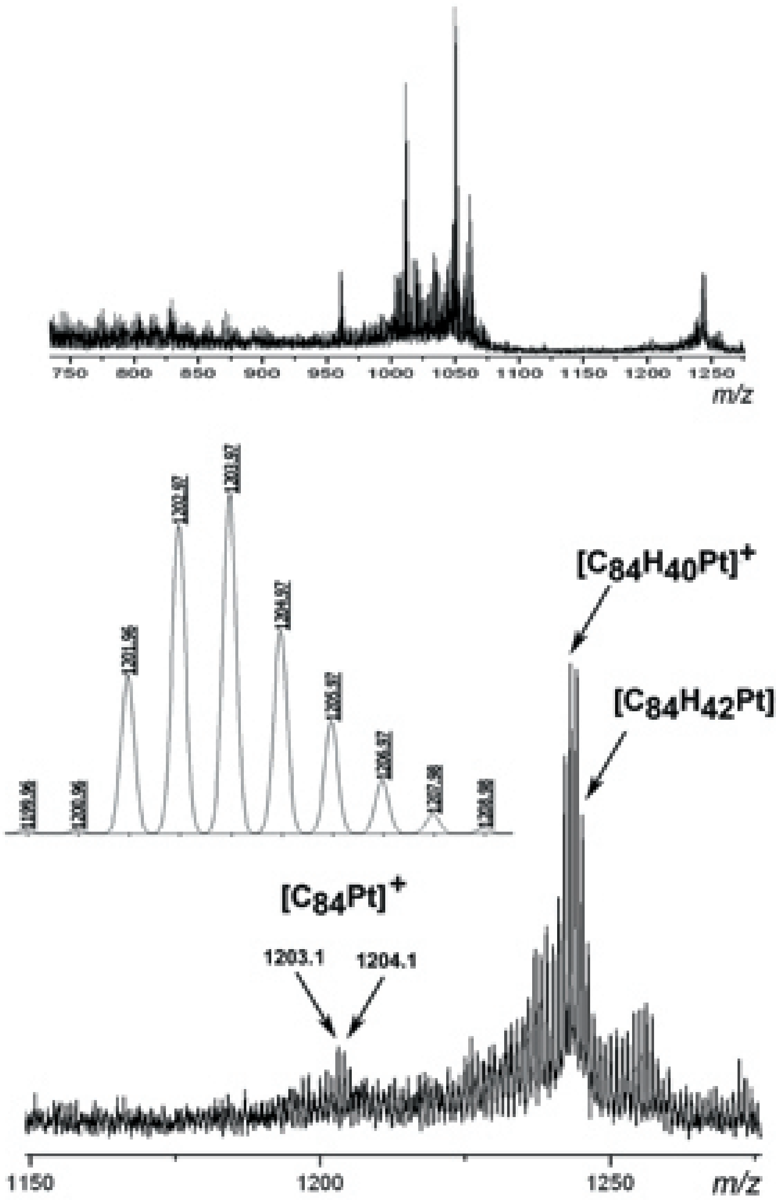

Figure 5.8: ToF-SIMS spectrum of $C_{84}H_{42}$ on Pt(111) in positive ion mode. a) An overview spectrum, showing m/z =1050 peak of $C_{84}H_{42}$ and 1008 peak. b) Theoretical distribution of C_{84}Pt peak; C) The 1150-1300 m/z region showing the $C_{84}H_{42}$Pt and C_{84}Pt peaks, H-loss is clearly seen and no evidence for C-loss.

ToF-SIMS measurements. The data for a C_{84} isomeric mixture on Pt(111) indicates that the charging process in this case is different as the m/z =1008 peak (C_{84}) is observed in the negative ion mode only (Figure 5.1.2). This is in contrast to the results for C_{84} powder where a C_2-loss pattern was observed in the positive ion spectra [146]. Precursor molecules, $C_{84}H_{42}$, deposited on Pt(111), on the other hand, exhibit a main $C_{84}H_{42}$ peak along with a series of $C_{84}H_{42}Pt_x$ peaks in positive ion mode confirming that the molecule remains intact during the evaporation process. Annealing both C_{84} and $C_{84}H_{42}$ results in a very similar ToF-SIMS pattern, where no 1008 peak is observed which indicates again a strong and modified molecule-substrate interactions. The careful inspection of the ToF-SIMS spectrum for $C_{84}H_{42}$ precursor reveals some peculiar details. The spectrum Figure 5.8a) represents two $C_{84}H_{42}Pt_x$ peaks. The peaks below 1050 m/z can be associated with hydrogen and C_2 losses. The next most intense peak corresponds to mass 1011.3 which can be ascribed to $C_{84}H_3$ or $C_{82}H_{27}$; however, it is likely that C_{84} formation happens at this stage already (the peak at 1008 is present but overlaps with peaks of other decomposition products). Indeed, magnifying the region shown in the square in Figure 5.8a, we notice the presence of both $C_{84}Pt$ and C_{84-m}-$H_{42-2n}Pt$ peaks where the peak distribution agrees well with the theoretical isotopic pattern of $C_{84}Pt$. We observe no C-loss peaks indicating the thermal stability of the species. The formation of C_{84} could be induced by the local heating during the Ga^+-bombardment.

The differences in the spectra before and after annealing listed above evidence the strong binding of the final reaction products to the substrate. On the other hand, the fact that annealed precursor species show patterns similar to the fullerene molecules deposited onto a hot substrate can serve as an indirect evidence of fullerene formation from the precursors.

5.2 Synthesis of CNTs from polyaromatic hydrocarbons on Rh(111)

The results described above lay ground for the synthesis of various types of nanostructures using cut-open precursors. In fact, this method was applied to the synthesis of carbon domes [38] and nanographenes [147]. Here the first results on the applications of combined SCCDH and CVD methods to the growth of the CNTs will be discussed.

The method presented is based on resent theoretical and experimental work suggesting that growth of single wall CNTs (SWNTs) starts by nucleation of an end-cap fragment on the catalyst particle followed by subsequent growth through incorporation of carbon atoms from the carbon feed-stock [148, 149]. Assuming this growth mechanism of CNTs, it is natural to look for a way to avoid the usual nucleation step of CNTs leading to the formation of an end-cap with accidental geometry by introducing a predefined end-cap molecule, the structure of which can be fully controlled. Subsequent growth will lead to the desired SWNT species as determined by the end-cap geometry.

The synthesis of several precursor molecules for different SWNT species, including armchair, zigzag or chiral type has been reported [150]. These polyaromatic hydrocarbons can then be folded into the corresponding bucky bowls by surface catalyzed cyclodehydrogenation as was presented in the previous section and in Figure 5.9a. Once the cap is formed, the chamber is filled with hydrocarbon gas (reaction gas) and the sample is heated to the temperatures high enough for the CVD process to take place. This last step leads to the cracking of the gas molecules at the surface and formation of the carbon feed-stock for the growth of the CNTs (Figure 5.9b). In the standard CVD growth the reaction gas, catalyst and the growth temperature are the key parameters governing the structure and quality of the CNTs. As far as the choice of the catalyst is concerned not only chemical composition but also its texture are important. When applying the CVD method on surfaces several aspects have to be considered. Firstly, the CVD temperatures cannot be too high. As we have seen in the previous section, fullerenes formed by means of SCCDH are stable only below a certain temperature threshold,

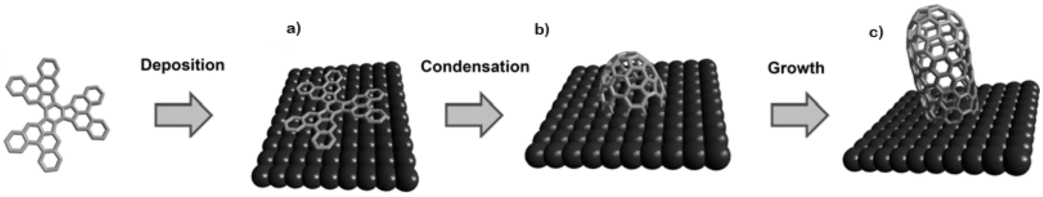

Figure 5.9: Schematics of the controlled growth of CNTs from cap precursors. The precursor molecules are thermally evaporated onto a catalytically active surface (a), where they are annealed to initiate SCCDH reaction leading to the formation of well-defined caps (b). The last step consists of heating the system to temperatures below the decomposition temperature and exposing it to the hydrocarbon gas atmosphere (c). This leads to the simultaneous cracking of hidrocarbon molecules, which form a carbon feed-stock for CNT growth.

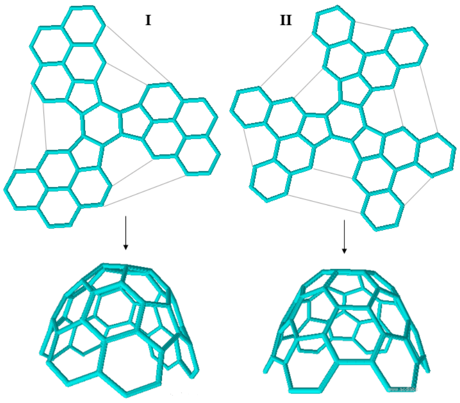

Figure 5.10: Cap precursor and corresponding reaction products after cyclodehydrogenation (indicated by the arrow): **I** $C_{54}H_{24}$ and **II** $C_{60}H_{30}$.

above which complete bond rearrangement takes place forming a layer of carbon. As we shall see later, the same conclusion holds for the CNT caps. On the other hand, too low CVD temperatures might not be sufficient for the growth of CNTs. The effect of temperature, time and post-annealing treatments on the CVD growth will be discussed in the following. The choice of the reaction gas is also important for the standard CVD. It was shown that at high temperatures (>1000 °C) methane is more suitable than ethylene or acetylene as it does not undergo self-decomposition at these temperatures. Under the low-temperature conditions used in our study, however, the type of reaction gas is not crucial and ethylene was used.

As has been mentioned, the CVD process on the surfaces is temperature-limited due to the precursor stability issues. Therefore, after caps have been formed, the corresponding decomposition temperatures have to be established. The employed precursor molecules and their reaction products after SCCDH reaction are shown on the Figure 5.10: precursor **I**-$C_{54}H_{24}$ and the corresponding nanotube cap with the diameter of 0.73 nm is expected to have a zig-zag structure, and precursor **II** - $C_{60}H_{30}$ should yield a cap for the armchair nanotube with the diameter of 0.77 nm. The Rh(111) surface was used for these experiments, on which the CVD growth of graphene has been reported in earlier studies [151–153], showing that reaction gas can be efficiently cracked to form sp^2 hybridized carbon structure.

When deposited onto the substrate at room temperature, both precursors **I** and **II** are imaged as trefoil-shaped protrusions, for which sometimes the symmetric structure can be resolved (Figure 5.11 a and d). Molecules remain intact despite the relatively high deposition temperatures of 740 K and 780 K for **I** and **II**, respectively. The random distribution of the molecules and the absence of step-edge decorations points at the strong molecule-substrate interactions, which is one of the key conditions for the successful SCCDH reactions. The base size of the molecules is found to be 1.8 (precursor **I**) nm and 2 nm (precursor **II**), and the height - 0.15 nm (precursor **I**) and 0.25 nm (precursor **II**) from the STM images. After annealing the sample to 730 K and 750 K, the complete transformation of all the trefoil species into the round molecules was observed, suggesting that the formation of caps has taken place. In order to test the stability of newly formed caps, the temperature range 780-930 K was explored. For the precursor **I** no change in the structure was found up to 820 K, after which the shape and the height of the molecules started to transform. The full transformation into flat carbon islands took place at about 875 K where small islands with typical Moiré - pattern were found. For the precursor **II**, the stability threshold is somewhat higher - $\sim$ 850 K, and the flat carbon islands are found at about 900 K. Note that the threshold temperatures are lower than the conventional temperatures used for the CVD growth, however since the cap for carbon nanotubes has already formed this might trigger the growth of CNTs.

To test this assumption the sample was heated to 800-820 K and exposed to the ethylene gas at $2{\times}10^{-8}$ mbar for various time intervals. The general nanotube growth mechanism in a CVD process involves the dissociation of hydrocarbon molecules catalyzed by the transition metal, and dissolution and saturation of carbon atoms in the metal nanoparticle. The precipitation of carbon from the saturated metal particle leads to the formation of tubular carbon solids in sp^2 structure. Tubule formation is favored over other forms of carbon such as graphitic sheets with open edges. This is because a tube contains no dangling bonds and therefore is in a low energy form. Based on this considerations, it is natural to apply a similar method on the surface, where the surface is saturated with carbon and 'induces' the growth of the nanotubes from the preformed caps. We subject the surface with caps to the $2{\times}10^{-8}$ mbar ethylene at the sample temperature of 815 K for 15 min, after which temperature was increased to 850 K during the next 2 min and kept at these temperature for another 15 min (for the reference the CVD for 10 min without cap molecules using the same parameters resulted in the monolayer amorphous carbon formation). After this treatment the sample was examined with STM and amorphous carbon layer was found. The short exposure times using the same parameters have resulted in the surface with caps and small patches of amorphous carbon.

Although the CVD did not result in the desired growth of CNTs, the results above are not unexpected. The whole growth procedure relies on the

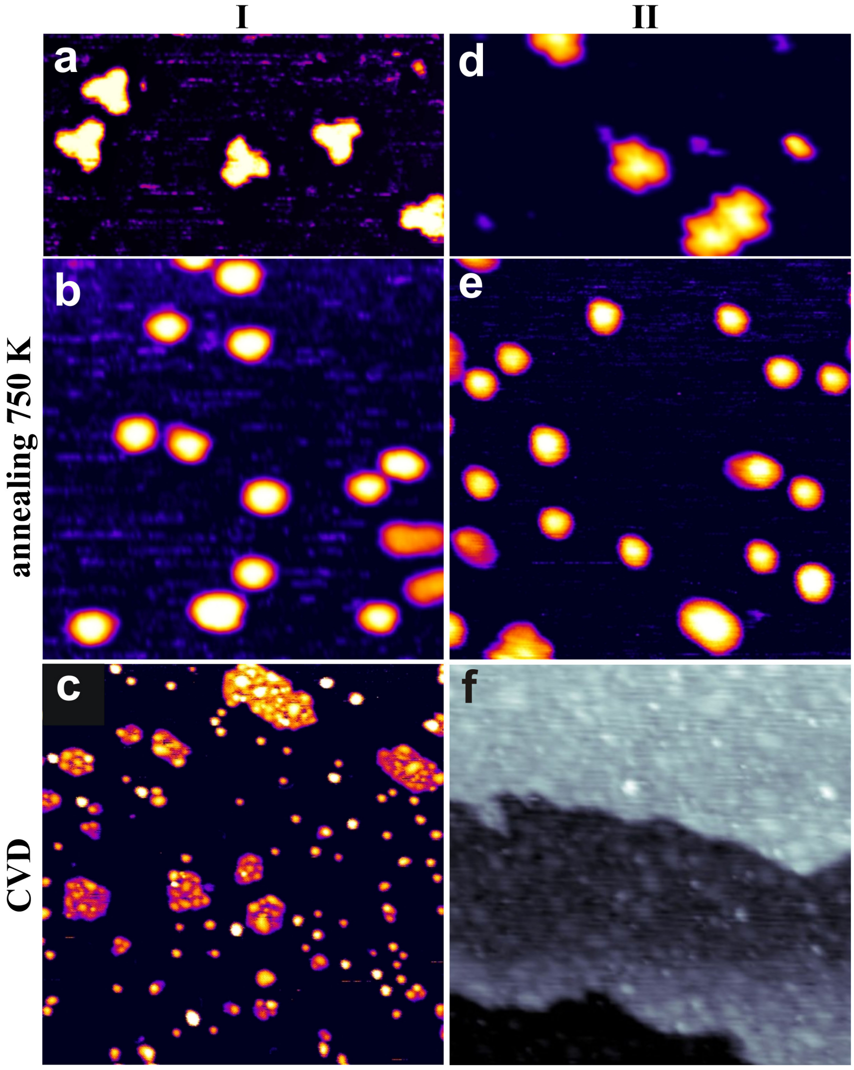

Figure 5.11: Cap formation from precursors and CVD growth. Precursors a) **I** and d) **II** as deposited onto the Rh(111) surface (image size 13×7.2 nm^2 and 13×8 nm^2 respectively)). Cap formation from the precursor b) **I** after annealing to 730 K for 5 min and e) **II** after annealing to 750 K for 5 min ((image size 13×13 nm^2). The cap formation was followed by CVD at 2×10^{-8} mbar ethylene with sample kept at 815 K: c) for (precursor **I**) during 10 sec, leading to the formation of carbonaceous islands and caps and f) for 15 min (precursor **II**) leading to the amorphous carbon layer formation (color changed to gray for clarity); STM images taken over 50×50 nm^2 area. Both procedures were tried on both precursors yielding the same result.

fact that the presence of pre-formed precursor caps would, in a sense, replace the stage of cap-formation on the catalyst nanoparticles used in the standard CVD and, thereby assuming that the structure of the catalyst is not important. In the light of the experiments reported above, it seems that the role of the catalyst structure, texture and chemical composition cannot be ignored. Therefore, as appealing as it might appear, the synthesis on the surface cannot be used in its present form. Based on the knowledge accumulated in the field of CVD growth, the usage of structured surfaces can be suggested. In this case, the known catalyst material for CNT growth, Fe, Ni or Co, can be evaporated onto an inert substrate to form small catalytically active sites. It is well-known, for example, that Ni forms well-defined Ni-Au clusters at the elbow-site of Au(111) surface reconstruction [154, 155]. The precursor molecules can then be deposited onto this structured surface. Alternatively, porous surface of alumina-covered $Ni_3Al(111)$ can be used[156]. The pores were found to form a periodic pattern which can be used as a template for the growth of metallic clusters. In fact clusters of Pd, Fe and Co of regular size were shown to grow on this surface[157]. The molecular mobility is known to be higher on the Au(111) or oxide surfaces compared to Rh or Pt surfaces, therefore precursors should bind to the clusters. The next step of precursor conversion into a cap and CVD growth could then be performed according to the scheme described above.

5.3 Synthesis of GNRs from polyphenylenes

The basic graphene nanoribbon (GNR) fabrication steps for the prototypical armchair ribbon of width N=9 obtained from dibromotriphenylene precursor monomers are depicted in Figure 5.12. Thermal sublimation of the monomers onto a solid surface leaves the molecules intact, the first annealing step removes their halogen substituents, yielding the molecular building blocks of the targeted graphene ribbon in the form of surface-stabilized biradical species. During a first thermal activation step, the diradical species diffuse across the surface and undergo radical addition reactions to form linear polymer chains as imprinted by the specific chemical functionality pattern of the monomers. In a second thermal activation step a surface-assisted cyclodehydrogenation establishes an extended fully aromatic system.

Figure 5.13 shows the polyarene precursors used for the synthesis of GNRs. As compared to acene-based precursors[41], the stability of poly-

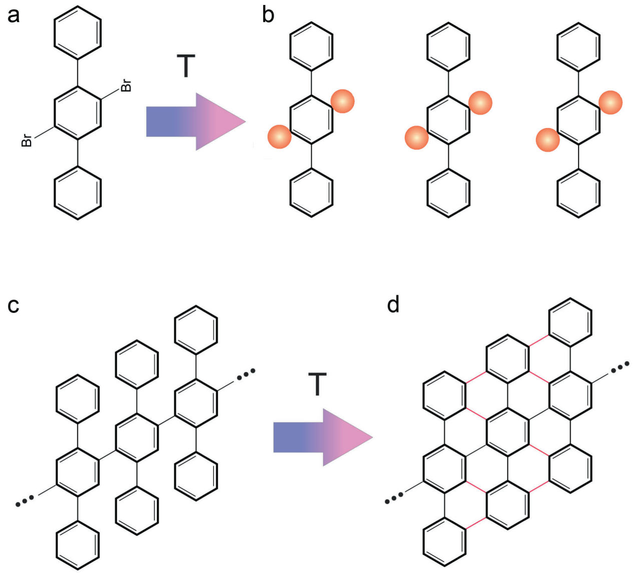

Figure 5.12: Schematics of the bottom-up fabrication of GNRs from precursors. Starting with thermal deposition (a), the precursors are annealed to induce dehalogenation during which the diradicals are formed (b). The diradicals react readily and form a covalent polymeric chain where each segment is covalently coupled to the next one (c). The next annealing step leads to formation of fully aromatic GNRs by cyclodehydrogenation (d).

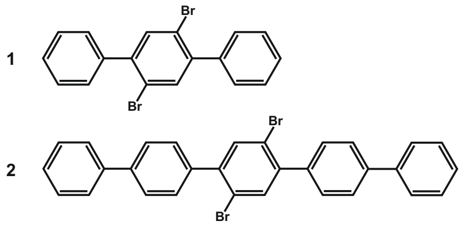

Figure 5.13: GNR precursors employed in this study: **1** Dibromotriphenylene and **2** Dibromopentaphenylene.

phenylene-based precursors is almost independent on the molecule size which allows the usage of higher homologues and fabricate wider ribbons. Although the precursor might acquire a planar conformation on the surface which would hinder the direct radical recombination, the rotational barrier between adjacent benzene rings is small enough to switch the geometry to twisted conformation and induce polymerization. On the other hand, polyphenylene precursors do not require preliminary dimerization, thus having molecular weights suitable for thermal deposition even in the cases of very wide ribbons.

Figure 5.14 summarizes our experimental findings for GNRs synthesis according to the scheme presented in Figure 5.12, using precursors **2** on the Au(111) surface. Both precursors are very mobile on the surface and can only be imaged when coverage is close to full monolayer. Annealing to 460 K leads to the formation of islands. Although the possibility of partial polymerization cannot be excluded since sometimes linear structures were observed as well, cf. Figure 5.14a, b. The first step to GNR fabrication intermolecular colligation through radical addition is thermally activated by annealing at 600 K, at which temperature the dehalogenated intermediates have enough thermal energy to diffuse along the surface and form single covalent CC bonds between each monomer to give polymer chains. STM images of the colligated monomers show protrusions that appear alternately on both sides of the chain axis and with a periodicity of 0.8 nm (Figure 5.14c, d), in agreement with the periodicity of the pentaphenylene core of about 0.6 nm. Steric hindrance between the hydrogen atoms of adjacent units rotates the phenyl rings around the σ-bonds connecting them, resulting in opposite tilts of successive polyphenylene units with respect to the metal surface. This deviation from planarity explains the higher apparent height of the polyanthrylenes of about 0.27 nm. Moreover, the polymer is imaged with a width of 1.75 nm in agreement with the structural model (1.8 nm). The fully aromatic system is obtained by annealing the sample in a second step at 720 K, which induces intramolecular cyclodehydrogenation of the polymer chain and hence the formation of an N = 15 armchair ribbon (Figure 5.14e, f) with 2.1 nm width and a markedly reduced apparent height of 0.14 nm. The results using the triphenylene are shown in Figure 5.15. Here too, the first annealing step of 450 K led to the formation of the polymers which, however, are difficult to image at room temperature due to their short lengths. The second annealing to 650 K yields fully aromatic GNRs.

As can be seen from the Figures 5.14 and 5.15, the GNRs formed from the polyphenylene precursors used here do not show perfect structure and are not entirely defect-free. Besides, GNRs of relatively good quality can be formed under the high precursor density conditions only, where the radicals are 'forced' to couple to each other in a desired configuration. At the lower precursor densities only very short GNRs along with single molecules were observed. The latter observation is most probably due to the formation of C-Au bond with the surface since as-deposited the precursor molecules show high mobility and can only be imaged when the coverage is close to a monolayer. Despite the defectiveness of the final products, the polymer formation

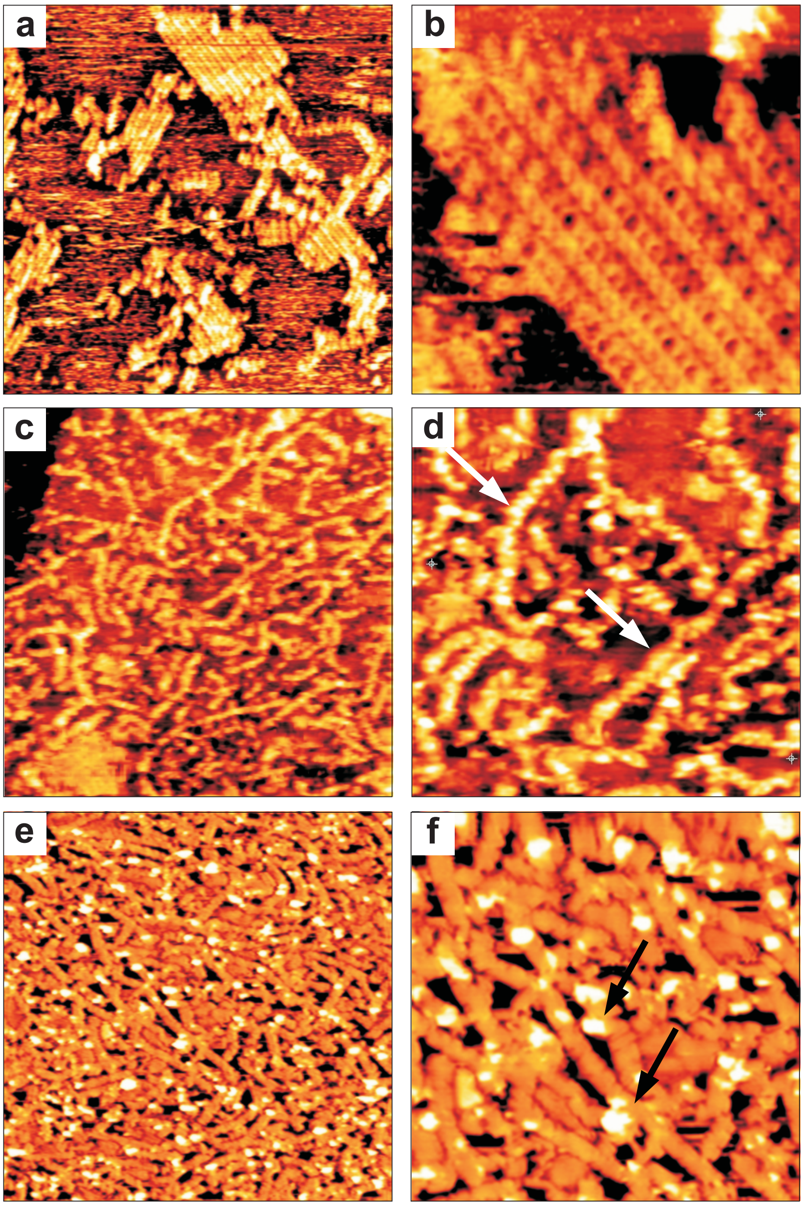

Figure 5.14: GNRs synthesized using dibromopentaphenylene: a) 59×59 nm^2 and b)15×15 nm^2 images of the surface after deposition of precursors and successive annealing to 460 K. STM images reveal islands and linear structure formed by molecules. c), d) Annealing to 600 K leads to the formation of biradicals which readily react to yield polymers. e), f) cyclodehydrogenation occurs at 720 K, at which temperature fully aromatic structure is formed (sizes of images are 59×59 nm^2 for c) and e) and 29×29 nm^2 for d) and f)).

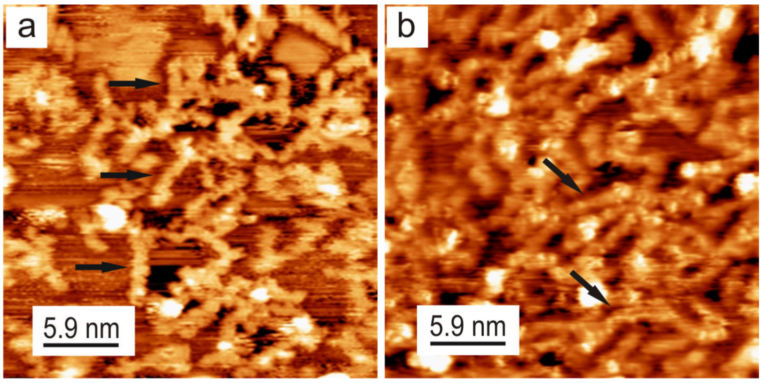

Figure 5.15: GNRs produced using triphenylene precursors. (a) At low coverage and (b) high coverage after annealing to 650 K, short GNRs along with mobile species are found on the surface. The width of GNRs is measured to be $\sim$ 1.1 nm from the STM data, which is in a good agreement with the structural model (1 nm) Image size (29×29 nm^2).

from the byradical of polyphenylene is a very interesting finding. It is known from basic chemistry that this type of radicals are very active and in principle the bonds within the radical should rearrange immediately or the radical is expected to form bonds with underlying substrate [158]. However, these radicals were found to react with each other and form polymers. The question regarding defects can be perhaps answered by the following considerations. The first annealing step leads to dehalogenation and formation of extremely active radicals. High precursor densities help in guiding the polymerization reaction but effects like tautomerization and bond rearrangement cannot be completely avoided (cf. Figure 5.16). On the other hand, due to increased reactivity of the diradical it forms new C-C bonds by cleaving the hydrogens and not by recombination with another radical at the Br positions. This idea finds its support in the observation at low coverages. Here, the very short GNRs are found along with a disordered phase of molecules bonded to the Au(111) surface.

Careful inspection of images presented in Figures 5.14 and 5.15 reveals the presence of large bright protrusions on the surface which most probably are reaction products of Au_xBr_y. It has been shown in the recent work, that halogenated cyclic polyphenylenes undergo dehalogenation upon adsorption on the surface and halogen atoms form a bond with the surface as was evidenced with XPS[159]. However, for particular cases of Au(111) and Ag(111) surfaces annealing at elevated temperatures lead to complete desorption of halogen atoms. In our case, neither higher temperature annealing up to 740

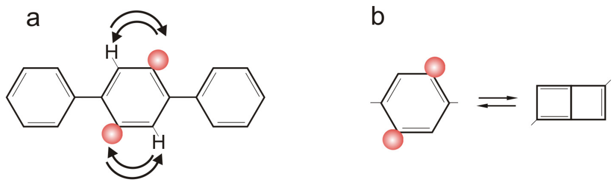

Figure 5.16: Possible transformations of diradical of triphenylene: a) tautomerization and b) one of the possible bond rearrangements.

K, nor long-time annealing (up to 14 h) lead to complete elimination of these species.

Coupling reactions, where either identical or different species of hydrocarbons are coupled to each other with the aid of a catalyst are well studied in the framework of synthetic chemistry. Several types of coupling reactions were discovered and some of them , e.g. the Ullmann reaction [160], were successfully carried out on the surface [161, 162]. Ni is also a well-known catalyst used for coupling reactions [163, 164]. These ideas were applied to the above-mentioned precursors in the expectation to guide the reaction and achieve better coupling. Various Ni(Cu) coverages, deposition onto a room-temperature and elevated temperature substrates were explored but essentially lead to the formation of GNRs as shown in Figures 5.14, 5.15 and clusters (Cu) or small islands (Ni) of metal atoms. At this point perhaps the role of the substrate in guiding the reaction path has to be considered. Unlike in previous sections of this chapter, where the surface catalyzed the cyclodehydrogenation reactions, here the mobility of adsorbed species suggests much weaker interaction with the substrate. In general there are few parameters that affect the growth of nanostructures on the surfaces: the deposition flux, the nucleation rate of precursors, their mobility and reactivity. The morphology of the final structure is a result of the intricate interplay of these parameters. Our experimental findings at low precursor coverages show the presence of various short length GNRs along with immobile single molecules. This suggests that dehalogenated species have preference to form bonds with the underlying substrate and that the nucleation rate is high and the formation of short-length ribbons is preferred. In order to reduce the nucleation rate higher coverages can be used where molecules would be confined and forced to react with each other, reactions occurring at the pre-defined positions. Note that in this case due to the confinement one reduces the mobility of the species as well. Indeed, our data at high coverage shows the formation of longer ribbons. The role of mobility and reactivity was nicely covered in the recent study, where covalent nanostructures formed by the same molecule (cyclohexa-*m*-phenylene) on Cu(111), Ag(111) and Au(111) have shown completely different morphology[159]. Monte-Carlo simulations have suggested that for the systems where coupling rate is much higher than the diffusion rate diffusing molecules immediately react to form a covalent bond once they hit each other. In this case the dendritic type of growth is encountered (on the Cu(111)). In the opposite extreme where the diffusion rate is higher than the coupling rate, formation of compact networks was observed (e.g. Ag(111)). These findings highlight the importance of the choice of the substrate in steering the reaction. In particular, for the systems considered in this section the choice should be towards the substrate where the nucleation rate will be reduced and the mobility is high enough to allow the molecules to diffuse and react with each other. In light of the investigation cited above, this could be, e.g. a Ag(111) surface, or a boron-nitride layer/metal system. The latter would be of particular interest, as the nanostructures thus synthesized will be decoupled from the metallic surface and ready to be investigated by STS to address their electronic properties.

5.4 Conclusions

This chapter summarized the results of our investigations of covalently bonded nanostructure synthesis from well-defined precursors. Three different systems were presented: fullerenes formed by means of SCCDH reaction on Pt(111), related to it formation of size and chirality-specific CNT caps on Rh(111) and the first results of growth of CNTs using conventional CVD method and at last the growth of armchair GNRs from polyphenylene precursors.

The selectivity of the C-C bond formation during the SCCDH reaction is an important issue. As it has been discussed above, the synthesis of C_{60} from the $C_{60}H_{30}$ precursor leaves the question of selectivity open because this fullerene has only one stable isomer. For the syntheses of higher fullerene species using SCCDH reaction its selectivity has to be demonstrated first, which was done by using a modified precursor. This precursor yielded an open-cage structure upon annealing demonstrating the selectivity of the synthesis. As a further step the isomerically pure C_{84} was synthesized from the respective precursor. All the reactions were tracked with STM for the structural characterization, and with ToF-SIMS to obtain the information on molecular composition/mass. This method represents a new possibility for the catalytic selective synthesis of higher fullerenes and CNTs.

The results above were applied to the synthesis of CNT caps on Rh(111) in attempt to synthesize size-selective CNTs. The principles of standard CVD were applied to grow nanotubes starting from precursor caps. The growth procedure has to be modified on the surface, as very high temperatures cannot be used due to the decomposition of the cap precursors at the temperatures higher than 850 K. It was shown that at temperatures below 850 K, only cap precursors and the amorphous carbon layer was found. Modifications of growth conditions and deposition/annealing sequence/time did not affect the overall result. Further experiments would be required to explore the effects of the substrate, its structure on the growth of CNTs by the method described above.

The last section was dedicated to the GNR synthesis using polyphenylene precursors. These precursors consist of a polyphenylene core and two bromine latent groups attached to one phenyl ring. It is clear that debromination results in highly reactive and potentially unstable species. Therefore, the formation of polymers upon annealing is an interesting finding as it shows that the diradical is stable enough to be submitted to further annealing yielding GNRs. The structure of the latter was found to have some defects. To improve the quality of the final product and gain insight into the effect of reaction conditions various temperatures, precursor coverages and coupling reaction schemes were explored. It was found that the polymer formation and, as a result, the structure of GNR are dependent on the intricate interplay between various parameters such as mobility, reactivity and nucleation. These parameters can be tuned by the appropriate choice of the substrate, therefore possible solution for the further improvement were discussed.

Chapter 6

Summary and Perspectives

In this thesis metal-organic coordination and on-surface cyclodehydrogenation reactions were used for the synthesis of nanostructures with preprogrammed structure and properties. Three main aspects of these nanostructures were explored:

- chirality of two-dimensional metal-organic coordination networks;
- magnetic properties of metal-organic coordination networks;
- and covalent-bond formation reactions.

As the mechanisms governing chiral separation and racemate formation still remain obscure, considerable effort was dedicated to investigating various systems possessing some degree of chirality. The STM, with its capability to resolve surface supported nanostructures at the submolecular level, has proven to be an indispensable tool to address these important issues. Here, STM was used to investigate the chirality of two systems - Mn and Cs-TCNQ$_4$ on Ag(100). It was found that both metals deposited onto the TCNQ precursor layer form nearly identical coordination motifs with the central metal center surrounded by four TCNQ molecules. As the molecular adsorption process results in the symmetry breaking of the molecules the units thus formed (MeTCNQ$_4$) are chiral, and two enantiomeric forms can be identified on the surface. These units were found to condense into extended domains. However, the translation of chirality from the units to domains in the Cs and Mn structures is very different. Cs-TCNQ$_4$ units form large domains with all units having the same chirality, while Mn-TCNQ$_4$ represents a racemate, that is units of alternating chirality comprise the domain. The DFT calculations performed to understand these observations have shown that chiral organization of these domains is due to the different nature of Mn-TCNQ and Cs-TCNQ bonds. In particular, Cs forms ionic, non-directional bonds which allow a high degree of rotational freedom of the molecules around the Cs-N bonds. On the contrary, Mn-TCNQ bonds are directional and rigid. When condensed into a domain, as a result of the flexibility of Cs-N bond, complexes were found to undergo a deformation where all the molecules fold around the central Cs atoms forming an umbrella-like shape. This allows the repulsive cyano-groups to avoid each other. This folding and deformation are not possible for the rigid Mn-N bond in the Mn-TCNQ$_4$ units. Therefore, the same effect is achieved by condensation with the unit of opposite chirality, since it was shown that cyano-groups remain in close proximity in the hypothetical homochiral Mn-TCNQ$_4$ structure.

The same principles of metal-organic coordination were applied to synthesize and investigate properties of Ni and MnTCNQ structures on Ag(100) and Au(111) surfaces. Highly ordered MeTCNQ network formation was shown on both substrates, the properties of which were investigated by XAS and XMCD. To gain insight into charge transfer effects, first the behavior of the constituents was investigated. By measuring the N K-edge spectra, it was found that on Ag(100) TCNQ acquires charge from the surface, while on Au(111) TCNQ remains neutral. Upon coordination to Mn, on both substrates, TCNQ nitrogen-edge spectra change significantly. However, Mn L-edge spectra for MnTCNQ/Ag(100) and MnTCNQ/Au(111) strongly resemble each other. This change is interpreted as the signature of lateral charge transfer. A similar effect was found for TCNQ coordinated to Ni on Ag(100) and Au(111) surfaces.

To better understand the role of lateral charge transfer in NiTCNQ structures on both substrates, the XAS/XMCD measurements for Ni adatom impurities on these surfaces were performed. Ni impurities in both cases did not show a sizable XMCD and appeared to be non-magnetic. They strongly hybridize with the surface states and are interpreted to assume a spin-quenched mixed-valence state. However, when coordinated to TCNQ, Ni centers recover their moment, and are found to have a mixed-valence configuration with d^8 and d^9 character on Au(111) and predominantly d^9 electronic configuration on Ag(100) from the XAS lineshape analysis. The magnetization curves for NiTCNQ networks have shown a pronounced s-shape than would be expected for paramagnetic S=1/2 (on Ag(100)) or S=1 (on Au(111)) centers. This is a clear indication of ferromagnetic coupling between Ni centers in the network. The effect cannot be attributed to a sizable orbital moment. Based on these results, two interaction schemes, namely ligand or surface electron mediated (RKKY) coupling, were proposed, which however, cannot be discriminated based on the XAS/XMCD measurements alone. Further experiments with closely related longer or shorter ligands or introduction of a decoupling layer between the metallic substrate and metal-organic networks would be advisable to better understand the coupling mechanism.

A sharp, well-defined XAS multiplet structure was observed for MnTCNQ networks on Au(111). The spectral lineshape suggests a d^5 configuration with little difference compared to the MnTCNQ network on Ag(100). The sum rule analysis for Mn centers on Au(111) has shown a sizable orbital moment, while no orbital moment was found on Ag(100). The Mn magnetization curves follow closely the Brillouin function for a high-spin center with d^5 configuration on both substrates. A little deviation from the Brillouin function for MnTCNQ networks on Ag(100) most probably indicates antiferromagnetic interaction of Ni centers, but could also be due to somewhat higher measurement temperature.

The last part of this thesis concentrated on the on-surface synthesis of covalently bonded nanostructures. The surfaces assisted cyclodehydrogenation reactions were applied to obtain fullerenes, CNT caps and graphene nanoribbons from the respective polycyclic hydrocarbons. For the synthesis of fullerenes and CNT caps catalytically active surfaces of Pt(111) and Rh(111) were used to activate the dehydrogenation and covalent bond formation process. The central issue of selective covalent bond formation during the fullerene formation reaction from the planar precursors was addressed by using a modified precursor. In this precursor one of the phenyl rings was shifted such that some folding paths were inhibited resulting in the formation of the so-called nanotetrahedra. These species can be easily distinguished by their lower apparent height and triangular shape from the C_{60} fullerenes. These results were then used to synthesize the higher fullerene C_{84} and CNT caps. Recently, it was suggested that the CVD growth of CNTs proceeds via cap formation. That is, caps of random size are formed on the catalytic nanoparticle, which act as a seed for further CNT growth. In this respect it appears very appealing to replace the random cap formation step by a controlled process where the cap size would be pre-defined. The precursor-based approach shown in this thesis represents a controlled way of CNT cap formation since the precursors define the size and the chirality of the CNT caps. These parameters ultimately are 'built-in' during the precursor synthesis stage.

The standard CVD method was applied to grow CNT from the pre-formed caps. STM was used to monitor the growth process. Images after CVD deposition of ethylene have revealed the presence of an amorphous carbon layer and CNT caps but no CNT growth was observed. Based on the knowledge accumulated in the field of CVD-growth of nanotubes, further improvement strategies were proposed. First, it is well-known that standard CVD utilizes the structured surfaces or, more precisely, catalytically active nanoparticles of Fe, Co, and Ni for the nanotube growth. Therefore, usage of surface supported Ni/Fe nanoparticles is suggested. An inert Au(111) surface can be used for this purpose as it is known that Ni nucleates at the elbow-sites of the herring-bone reconstruction of the Au(111) surface. NiAu clusters with a very narrow distribution of size were shown to grow on Au(111). This fact is of particular importance since several experiments have indicated that the CNT diameter depends on the nanoparticle size on which it is grown [165–167]. As an alternative an ultrathin aluminum oxide layer on $Ni_3Al(111)$ can be used. The aluminum oxide layer is shown to have regularly spaced pores of well-defined size. This porous surface was used to grow highly ordered, regular clusters of Fe, Co and Pd. The former two, Fe and Co, are well-known catalysts for the CVD growth of CNTs. Therefore, these systems could be potentially used for the precursor-based CNT growth.

The GNR formation from polyphenylenes reported here is based on the fact that unlike previously used polyacenes they allow production of GNRs of variable widths by addition of phenyl rings without affecting the stability of the precursors. Upon dehalogenation highly reactive radicals are formed which readily react with each other or the substrate. Therefore, special care has to be taken when choosing the appropriate reaction conditions. Surprisingly, despite the high reactivity of the radicals, they were found to react with each other and form polymers at the pre-defined positions, showing the suitability of these type of precursors for polymerization reactions. This, however, can only be achieved at high precursor coverages, when the precursors are confined and 'forced' to form the bonds along the Br-positions. When the polymer is submitted to the second annealing step, extended ribbons form. At low coverage, only short ribbons and single molecules were found on the surface suggesting bonding to the substrate. In both cases the structures were found to have some defects, most probably due to the reactivity of the dehalogenated radicals. This is ultimately because effects like tautomerization cannot be completely excluded. Furthermore, the polymerization reactions can occur via the cleavage of hydrogen and subsequent C-C bond formation. As polymerization reaction on surfaces were suggested to be governed by parameters like precursor mobility, nucleation rate and reactivity, we propose the usage of surfaces on which the precursor mobility is preserved while the nucleation rate is decreased. This can be either Ag(111) as suggested by Ref. [159] or a boron nitride layer on metallic surfaces. The latter is particularly interesting because it would allow STS investigations of the electronic properties of GNRs decoupled from the metallic substrate.

The controlled on-surface approach to the synthesis of covalently bound nanostructures is a path towards rational bottom-up molecular assembly at the nanoscale. Starting with the organic chemistry to generate the molecular precursor that must be either combined with other precursors to construct a molecular nanostructure or transformed into others, as in Chapter 5. This puts forward new goals for chemistry: the design of the desired molecule for specific properties, the synthesis of their constituent pieces, and their assembly using the catalytic properties of a nanostructured surface at specific locations required for addressing an electrical signal. This new approach is intrinsically interdisciplinary and can only be successful after convergence of the approaches of several disciplines. In fact, the results reported here combine the use of the catalytic properties of metallic surfaces to generate new carbonaceous species, and the synthesis of CBNs as an essential element for future electronics. All the conditions met, it will become a useful method in the field of molecular electronics.

Bibliography

[1] G. K. Binnig and H. Rohrer. Scanning tunneling microscopy. *IBM Journal of Research and Development*, 44:279, 2000.

[2] R. Yamachika, M. Grobis, A. Wachowiak, and M. F. Crommie. Controlled Atomic Doping of a Single C_{60} Molecule. *Science*, 304:281, 2004.

[3] M. F. Crommie, C. P. Lutz, and D. M. Eigler. Confinement of Electrons to Quantum Corrals on a Metal Surface. *Science*, 262(5131):218, 1993.

[4] A. J. Heinrich, C. P. Lutz, J. A. Gupta, and D. M. Eigler. Molecule cascades. *Science*, 298(5597):1381, 2002.

[5] James K. Gimzewski and Christian Joachim. Nanoscale science of single molecules using local probes. *Science*, 283:1683, 1999.

[6] W. Ho. Single-molecule chemistry. 117:11033, 2002.

[7] G.A. Somorjai and Y. Li. *Introduction to Surface Chemistry and Catalysis.* Wiley, 2010.

[8] T. A. Jung, R. R. Schlittler, and J. K. Gimzewski. Conformational identification of individual adsorbed molecules with the STM. *Nature*, 386:696, 1997.

[9] M. Böhringer, K. Morgenstern, W.-D. Schneider, R. Berndt, F. Mauri, A. De Vita, and R. Car. Two-dimensional self-assembly of supramolecular clusters and chains. *Phys. Rev. Lett.*, 83:324, 1999.

[10] A. Dmitriev, H. Spillmann, N. Lin, J. V. Barth, and K. Kern. Modular assembly of two-dimensional metal-organic coordination networks at a metal surface. *Angewandte Chemie International Edition*, 42:2670, 2003.

[11] J. V. Barth, J. Weckesser, C. Cai, Peter Günter, L. Bürgi, O. Jeandupeux, and K. Kern. Building supramolecular nanostructures at surfaces by hydrogen bonding. *Angewandte Chemie International Edition*, 39:1230, 2000.

[12] K. W. Hipps, Louis Scudiero, Dan E. Barlow, and Manning P. Cooke. A self-organized 2-dimensional bifunctional structure formed by supramolecular design. *Journal of the American Chemical Society*, 124:2126, 2002.

[13] H. Spillmann, A. Dmitriev, N. Lin, P. Messina, J. V. Barth, and K. Kern. Hierarchical assembly of two-dimensional homochiral nanocavity arrays. *Journal of the American Chemical Society*, 125:10725, 2003.

[14] J.-M. Lehn. *Supramolecular chemistry: concepts and perspectives.* VCH, Weinheim. Germany, 1995.

[15] J.-M. Lehn. Supramolecular chemistry - scope and perspectives molecules, supermolecules, and molecular devices (nobel lecture). *Angew. Chem. Int. Ed.*, 27:89, 1988.

[16] K.-F. Braun and K.-H. Rieder. Engineering electronic lifetimes in artificial atomic structures. *Phys. Rev. Lett.*, 88:096801, 2002.

[17] J.W. Steed and J.L. Atwood. *Supramolecular chemistry.* Wiley, Germany, 2009.

[18] Bradley J. Holliday and Chad A. Mirkin. Strategies for the construction of supramolecular compounds through coordination chemistry. *Angewandte Chemie International Edition*, 40:2022, 2001.

[19] A. Werner. Beitrag zur konstitution anorganischer verbindungen. *Zeitschrift für anorganische Chemie*, 3:267, 1893.

[20] O. Kahn. *Molecular Magnetism.* Wiley-VCH, 1993.

[21] J. R. Galán-Mascarós and K. R. Dunbar. A self-assembled 2d molecule-based magnet: The honeycomb layered material Co3Cl4(H2O)2[Co(Hbbiz)3]2. *Angewandte Chemie International Edition*, 42:2289, 2003.

[22] M. Ruben, J. Rojo, F. J. Romero-Salguero, L. H. Uppadine, and J.-M. Lehn. Grid-type metal ion architectures: Functional metallosupramolecular arrays. *Angewandte Chemie International Edition*, 43:3644, 2004.

[23] G. A. Attard. Electrochemical Studies of Enantioselectivity at Chiral Metal Surfaces. *J. Phys. Chem. B*, 105:3158, 2001.

[24] C.F. McFadden, P.S. Cremer, and A.J. Gellman. Adsorption of chiral alcohols on 'chiral' metal surfaces. *Langmuir*, 12:2483, 1996.

[25] D. S. Sholl, A. Asthagiri, and T. D. Power. Naturally chiral metal surfaces as enantiospecific adsorbents. *J. of Phys. Chem. B*, 105(21):4771, 2001.

[26] R. Raval. Chiral expressions at metal surfaces. *Current Opinion in Solid State and Materials Science*, 7:67, 2003.

[27] SM Barlow and R Raval. Complex organic molecules at metal surfaces: bonding, organisation and chirality. *Surface Science Reports*, 50:201, 2003.

[28] R. Raval. *Chirality at the nanoscale: nanoparticles, surfaces, materials and more*, chapter 6. Wiley-VCH, 2009.

[29] S. Haq, N. Liu, V. Humblot, A. P. J. Jansen, and R. Raval. Drastic symmetry breaking in supramolecular organization of enantiomerically unbalanced monolayers at surfaces. *Nature Chemistry*, 1:409, 2009.

[30] M. Lingenfelder, G. Tomba, G. Costantini, C. L. Colombi, A. DeVita, and K. Kern. Tracking the chiral recognition of adsorbed dipeptides at the single-molecule level. *Angewandte Chemie International Edition*, 46:4492, 2007.

[31] H.-U. Blaser. Enantioselective synthesis using chiral heterogeneous catalysts. *Tetrahedron: Asymmetry*, 2:843, 1991.

[32] G. Ertl, H. Knözinger, and J. Weitkamp. *Handbook of heterogeneous catalysis*. Number v. 4. VCH, New York, 1997.

[33] K.T. Wan and M.E. Davis. Design and Synthesis of a heterogeneous asymmetric catalyst. *Nature*, 370:449, 1994.

[34] A. P. Côté, A. I. Benin, N. W. Ockwig, M. O'Keeffe, A. J. Matzger, and O. M. Yaghi. Porous, Crystalline, Covalent Organic Frameworks. *Science*, 310:1166, 2005.

[35] L. Grill, M. Dyer, L. Lafferentz, M. Persson, M. V. Peters, and S. Hecht. Nano-architectures by covalent assembly of molecular building blocks. *Nature Nanotechnology*, 2:687, 2007.

[36] L. Lafferentz, F. Ample, H. Yu, S. Hecht, C. Joachim, and L. Grill. Conductance of a single conjugated polymer as a continuous function of its length. *Science*, 323:1193, 2009.

[37] S. Weigelt, C. Busse, C. Bombis, M. Knudsen, K. V. Gothelf, T Strunskus, C. Wöll, M. Dahlbom, B. Hammer, E. Læ gsgaard, F. Besenbacher, and T. R. Linderoth. Covalent Interlinking of an Aldehyde and an Amine on a Au(111) Surface in Ultrahigh Vacuum. *Angewandte Chemie International Edition*, 46:9227, 2007.

[38] K. Rim, M. Siaj, Sh. Xiao, M. Myers, V. D. Carpentier, L. Liu, Ch. Su, M. L. Steigerwald, M. S. Hybertsen, P. H. McBreen, G. W. Flynn, and C. Nuckolls. Forming aromatic hemispheres on transition-metal surfaces. *Angewandte Chemie International Edition*, 46:7891, 2007.

[39] G. Otero, G. Biddau, C. Sanchez-Sanchez, R. Caillard, M. F. Lopez, C. Rogero, F. J. Palomares, N. Cabello, M. A. Basanta, J. Ortega, J. Mendez, A. M. Echavarren, R. Perez, B. Gomez-Lor, and J. A. Martin-Gago. Fullerenes from aromatic precursors by surface-catalysed cyclodehydrogenation. *Nature*, 454:865, 2008.

[40] K. Amsharov, N. Abdurakhmanova, S. Stepanow, S. Rauschenbach, M. Jansen, and K. Kern. Towards the Isomer-Specific Synthesis of Higher Fullerenes and Buckybowls by the Surface-Catalyzed Cyclodehydrogenation of Aromatic Precursors. *Angewandte Chemie International Edition*, 49:9392, 2010.

[41] J. Cai, P. Ruffieux, R. Jaafar, M. Bieri, T. Braun, S. Blankenburg, M. Muoth, A. P. Seitsonen, M. Saleh, X. Feng, K. Muellen, and R. Fasel. Atomically precise bottom-up fabrication of graphene nanoribbons. *Nature*, 466:470, 2010.

[42] J.A. Stroscio and W.J. Kaiser. *Scanning tunneling microscopy.* Methods of experimental physics. Academic Press, 1993.

[43] R. Wiesendanger. *Scanning probe microscopy: analytical methods.* Nanoscience and technology. Springer-Verlag, 1998.

[44] J. Tersoff and D. R. Hamann. Theory and application for the scanning tunneling microscope. *Physical Review Letters*, 50:1998, 1983.

[45] J. Tersoff and D. R. Hamann. Theory of the scanning tunneling microscope. *Physical Review B*, 31:805, 1985.

[46] N. D. Lang. Spectroscopy of Single Atoms in the Scanning Tunneling Microscope. *Physical Review B*, 34:5947, 1986.

[47] M. Blume. Magnetic scattering of x-rays. *Journal of Applied Physics*, 57:3615, 1985.

[48] F. Groot and A. Kotani. *Core level spectroscopy of solids.* Advances in condensed matter science. CRC Press, 2008.

[49] F. M. F. de Groot, J. C. Fuggle, B. T. Thole, and G. A. Sawatzky. 2p x-ray absorption of 3d transition-metal compounds: An atomic multiplet description including the crystal field. *Phys. Rev. B*, 42:5459, 1990.

[50] H. Ebert. Magneto-optical effects in transition metal systems. *Reports on Progress in Physics*, 59:1665, 1996.

[51] D. Mauri, R. Allenspach, and M. Landolt. Electron spin polarization in inner-shell excitations in a solid. *Phys. Rev. Lett.*, 52:152, 1984.

[52] P. Carra, B. T. Thole, M. Altarelli, and X. Wang. X-ray circular dichroism and local magnetic fields. *Phys. Rev. Lett.*, 70:694, 1993.

[53] M. Altarelli. Orbital-magnetization sum rule for x-ray circular dichroism: A simple proof. *Phys. Rev. B*, 47:597, 1993.

[54] J. Stöhr and H. König. Determination of spin- and orbital-moment anisotropies in transition metals by angle-dependent x-ray magnetic circular dichroism. *Phys. Rev. Lett.*, 75:3748, 1995.

[55] B. T. Thole, P. Carra, F. Sette, and G. van der Laan. X-ray circular dichroism as a probe of orbital magnetization. *Phys. Rev. Lett.*, 68:1943, 1992.

[56] J. Stöhr. Exploring the microscopic origin of magnetic anisotropies with X-ray magnetic circular dichroism (XMCD) spectroscopy. *Journal of Magnetism and Magnetic Materials*, 200:470, 1999.

[57] R. Wu and A. J. Freeman. Spin-orbit induced magnetic phenomena in bulk metals and their surfaces and interfaces. *Journal of Magnetism and Magnetic Materials*, 200:498, 1999.

[58] S. Stepanow. *Low-dimensional supramolecular architectures at metal surfaces*. PhD thesis, EPF Lausanne, 2005.

[59] `http://www.fkf.mpg.de/ga/`.

[60] `http://www.iontof.com/`.

[61] `http://www.esrf.eu/`.

[62] `http://www.sigmaaldrich.com/germany`.

[63] `http://www.fkf.mpg.de/jansen/`.

[64] `http://www.saesgetters.com/`.

[65] `http://www.omicron.de/`.

[66] K.W. Busch and M.A. Busch. *Chiral analysis*. Elsevier, 2006.

[67] I.K. Reddy and R. Mehvar. *Chirality in drug design and development*. Marcel Dekker, 2004.

[68] J.M. Brown and S.G. Davies. Chemical asymmetric-synthesis. *Nature*, 342:631, 1989.

[69] R.M. Hazen and D.S. Sholl. Chiral selection on inorganic crystalline surfaces. *Nature Materials*, 2:367, 2003.

[70] S. J. Jenkins and S. J. Pratt. Beyond the surface atlas: A roadmap and gazetteer for surface symmetry and structure. *Surface Science Reports*, 62:373, 2007.

[71] A. J. Gellman. Chiral surfaces: Accomplishments and challenges. *ACS Nano*, 4:5, 2010.

[72] D. Andelman and H. Orland. Chiral discrimination in solutions and in langmuir monolayers. *Journal of the American Chemical Society*, 115:12322, 1993.

[73] I. Paci, I. Szleifer, and M. A. Ratner. Chiral separation: Mechanism modeling in two-dimensional systems. *Journal of the American Chemical Society*, 129:3545, 2007.

[74] W. Mönch. Adsorbate induced surface states and fermi-level pinning at semiconductor surfaces. *J. Vac. Sci. Tech. B: Microelectronics and Nanometer Structures*, 7:1216, 1989.

[75] T. C. Leung, C. L. Kao, W. S. Su, Y. J. Feng, and C. T. Chan. Relationship between surface dipole, work function and charge transfer: Some exceptions to an established rule. *Phys. Rev. B*, 68:195408, 2003.

[76] G. P. Lopinski, D. J. Moffatt, D. D. Wayner, and R. A. Wolkow. Determination of the absolute chirality of individual adsorbed molecules using the scanning tunnelling microscope. *Nature*, 392:909, 1998.

[77] Hongbin F., L.C. Giancarlo, and G.W. Flynn. Direct determination of the chirality of organic molecules by scanning tunneling microscopy. *Journal of Physical Chemistry B*, 102:7311, 1998.

[78] M. Böhringer, W.-D. Schneider, and R. Berndt. Real space observation of a chiral phase transition in a two-dimensional organic layer. *Angew. Chem. Int. Ed.*, 39:792, 2000.

[79] J. Weckesser, A. De Vita, J. V. Barth, C. Cai, and K. Kern. Mesoscopic correlation of supramolecular chirality in one-dimensional hydrogen-bonded assemblies. *Phys. Rev. Lett.*, 87:096101, 2001.

[80] A. Kühnle, T. R. Linderoth, B. Hammer, and F. Besenbacher. Chiral recognition in dimerization of adsorbed cysteine observed by scanning tunnelling microscopy. *Nature*, 415:891, 2002.

[81] Q. Chen, D. J. Frankel, and N. V. Richardson. Self-assembly of adenine on cu(110) surfaces. *Langmuir*, 18:3219, 2002.

[82] A. Dmitriev, H. Spillmann, M. Lingenfelder, N. Lin, J. V. Barth, and K. Kern. Design of extended surface-supported chiral metal-organic arrays comprising mononuclear iron centers. *Langmuir*, 20:4799, 2004.

[83] F. Vidal, E. Delvigne, S. Stepanow, N. Lin, J. V. Barth, and K. Kern. Chiral phase transition in two-dimensional supramolecular assemblies of prochiral molecules. *J. Am. Chem. Soc.*, 27:10101, 2005.

[84] T.-C. Tseng, N. Abdurakhmanova, S. Stepanow, and K. Kern. Hierarchical Assembly and Reticulation of Two-Dimensional Mn- and NiTCNQx (x = 1, 2, 4) Coordination Structures on a Metal Surface. *The Journal of Physical Chemistry C*, 115:10211, 2011.

[85] J. V. Barth. Molecular architectonic on metal surfaces. *Ann. Rev. Phys. Chem.*, 58:375, 2007.

[86] S. Leininger, B. Olenyuk, and Stang P. J. Self-assembly of discrete cyclic nanostructures mediated by transition metals. *ChemInform*, 31:1522, 2000.

[87] M. Eddaoudi, J. Kim, N. Rosi, D. Vodak, J. Wachter, M. O'Keeffe, and Yaghi O. M. Systematic design and pore size and functionality in isoreticular mofs and their application in methane storage. *Science*, 295:469, 2002.

[88] N. N. Greenwood and A Earnshaw. *Chemistry of the elements.* Pergamon Press, 1984.

[89] J. He, C. Yang, Z. Xu, M. Zeller, A. D. Hunter, and J. Lin. Building thiol amd metal-thiolate functions into coordination nets: Clues from a simple molecule. *Journal of Solid State Chemistry*, 182:1821, 2009.

[90] J. Ferraris, D. O. Cowan, V. Jr. Walatka, and J. H. Perlstein. Electron-transfer in a new highly conducting ddonor-acceptor complex. *J. Am. Chem. Soc.*, 95:948, 1973.

[91] J. S. Miller. Magnetically ordered molecule-based assemblies. *Dalton. Trans.*, 23:2742, 2006.

[92] E. B. Vickers, I. D. Giles, and J. S. Miller. M[tcnq]$_x$ -based magnets (m = mn, fe, co, ni). *Chem. Mater.*, 17:1667, 2005.

[93] E. J. Schelter, F. Karadas, C. Avendano, A. V. Prosvirin, and K. R. Wernsdorfer, W. Dunbar. A family of mised-metal cyanide cubes with alternating octahedral and tetrahedral corners exhibiting a variety of magnetic behavior including single molecule magnetism. *J. Am. Chem. Soc.*, 129:8139, 2007.

[94] R. Clerac, S. O'Kane, J. Cowen, X. Ouyang, R. Heintz, H. Zhao, Jr. Bazile, M. J., and K. R. Dumbar. Glassy magnets composed of metals coordinated to 7,7,8,8-tetracyanoquinodimethane: M(tcnq)$_2$ (m = mn, fe, co, ni). *Chem. Mater.*, 15:1840, 2003.

[95] T.-C. Tseng. *TCNQ-based Supramolecular Architectures at Metal Surfaces.* PhD thesis, EPF Lausanne, 2010.

[96] T.-C. Tseng, C. Lin, X. Shi, S. L. Tait, X. Liu, U. Starke, N. Lin, R. Zhang, C. Minot, M. A. Van Hove, J. I. Cerdá, and K. Kern. Two-dimensional metal-organic coordination networks of Mn-7,7,8,8-tetracyanoquinodimethane assembled on Cu(100): Structural, electronic, and magnetic properties. *Phys. Rev. B*, 80:155458, 2009.

[97] T. Jo and G. A. Sawatzky. Ground state of ferromagnetic nickel and magnetic circular dichroism in ni 2p core x-ray-absorption spectroscopy. *Phys. Rev. B*, 43:8771, 1991.

[98] G. van der Laan and B. T. Thole. Electronic correlations in ni 2p and 3p magnetic x-ray dichroism and x-ray photoemission of ferromagnetic nickel. *J. Phys.: Condensed Matter*, 4:4181, 1992.

[99] K. J. Fernandez-Torrente, I.and Franke and J. I. Pascual. Structure and electronic configuration of tetracyanoquinodimethane layers on a au(111) surface. *Int. J. Mass Spectrosc.*, 277:269, 2008.

[100] G. Long and R. D. Willett. Electrochemical synthesis, characterization and magnetic studies of ni/tcnq salts. *Inorganica Chimica Acta*, 313:1, 2001.

[101] M. A. Ruderman and C. Kittel. Indirect exchange coupling of nuclear magnetic moments by conduction electrons. *Phys. Rev.*, 96:99, 1954.

[102] K. Yosida. Magnetic properties of cu-mn alloys. *Phys. Rev.*, 106:893, 1957.

[103] T. Kasuya. A theory of metallic ferro- and antiferromagnetism on zener's model. *Prog. of Theor. Phys.*, 16:45, 1956.

[104] D. Wegner, R. Yamachika, X. Zhang, Y. Wang, T. Baruah, M. R. Pederson, B. M. Bartlett, J. R. Long, and M. F. Crommie. Tuning molecule -mediated spin coupling in bottom-up-fabricated vanadium tetracyanoethylene nanostructures. *Phys. Rev. Lett.*, 103:087205, 2009.

[105] M. Burghard, H. Klauk, and K. Kern. Carbon-Based Field-Effect Transistors for Nanoelectronics. *Advanced Materials*, 21:2586, 2009.

[106] Heath J. R. O'Brien S. C. Curl R. F. Smalley R. E. Kroto, H. W. C_{60}: Buckminsterfullerene. *Nature*, 318:162, 1985.

[107] W. Kratschmer, L. D. Lamb, K. F., and D. R. Huffman. Solid C_{60}: a new form of carbon. *Nature*, 347:354–358, 1990.

[108] T. J. S. Dennis, T. Kai, K. Asato, T. Tomiyama, H. Shinohara, T. Yoshida, Y. Kobayashi, H. Ishiwatari, Y. Miyake, K. Kikuchi, and Y. Achiba. Isolation and Characterization by 13C NMR Spectroscopy of [84]Fullerene Minor Isomers. *The Journal of Physical Chemistry A*, 103:8747, 1999.

[109] G. Mehta and H. S. P. Rao. Synthetic studies directed towards bucky-balls and bucky-bowls. *Tetrahedron*, 54:13325, 1998.

[110] M. J. Plater, M. Praveen, and D. M. Schmidt. Buckybowlsynthesis: A Novel Application of Flash Vacuum Pyrolysis. *Fullerene Science and Technology*, 5:781, 1997.

[111] L. T. Scott. Fragments of fullerenes: Novel syntheses, structures and reactions. *ChemInform*, 27, 1996.

[112] L. T. Scott. Methods for the chemical synthesis of fullerenes. *Angewandte Chemie International Edition*, 43:4994, 2004.

[113] L. T. Scott, M. M. Boorum, B. J. McMahon, S. Hagen, J. Mack, J. Blank, H. Wegner, and A. de Meijere. A Rational Chemical Synthesis of C_{60}. *Science*, 295:1500–1503, 2002.

[114] K. Amsharov and M. Jansen. Synthesis of a higher fullerene precursor-an unrolled C_{84} fullerene. *Chem. Commun.*, page 2691, 2009.

[115] Konstantin Yu. Amsharov and Martin Jansen. A C_{78} Fullerene Precursor: Toward the Direct Synthesis of Higher Fullerenes. *The Journal of Organic Chemistry*, 73:2931, 2008.

[116] T. W. Ebbesen and P. M. Ajayan. Large-scale synthesis of carbon nanotubes. *Nature*, 358:220, 1992.

[117] A. Eftekhari, A. Jafarkhani, and F. Moztarzadeh. High-yield synthesis of carbon nanotubes using a water-soluble catalyst support in catalytic chemical vapor deposition. *Carbon*, 44:1343, 2006.

[118] Mukul K. and Yoshinori A. Carbon nanotubes from camphor: An environment-friendly nanotechnology. *Journal of Physics: Conference Series*, 61:643, 2007.

[119] R. E. Smalley, Y. Li, V. C. Moore, B. K. Price, R. Colorado, H. K. Schmidt, R. H. Hauge, A. R. Barron, and J. M. Tour. Single wall carbon nanotube amplification: En route to a type-specific growth mechanism. *Journal of the American Chemical Society*, 128:15824, 2006.

[120] M. Fujita, K. Wakabayashi, K. Nakada, and K. Kusakabe. Peculiar localized state at zigzag graphite edge. *J. Phys. Soc. Japan*, 65:1920, 1996.

[121] K. Nakada, M. Fujita, G. Dresselhaus, and M. S. Dresselhaus. Edge state in graphene ribbons: Nanometer size effect and edge shape dependence. *Phys. Rev. B*, 54:17954, 1996.

[122] K. Wakabayashi, M. Fujita, H. Ajiki, and M. Sigrist. Electronic and magnetic properties of nanographite ribbons. *Phys. Rev. B*, 59:8271, 1999.

[123] J. Jung, T. Pereg-Barnea, and A. H. MacDonald. Theory of interedge superexchange in zigzag edge magnetism. *Phys. Rev. Lett.*, 102:227205, 2009.

[124] Y. Han, B. Özyilmaz, Y. Zhang, and Ph. Kim. Energy band-gap engineering of graphene nanoribbons. *Phys. Rev. Lett.*, 98:206805, 2007.

[125] V. Barone, O. Hod, and G. E. Scuseria. Electronic Structure and Stability of Semiconducting Graphene Nanoribbons. *Nano Letters*, 6:2748, 2006.

[126] S. S. Datta, D. R. Strachan, S. M. Khamis, and A. T. C. Johnson. Crystallographic Etching of Few-Layer Graphene. *Nano Letters*, 8:1912, 2008.

[127] X. Yang, X. Dou, A. Rouhanipour, L. Zhi, H. J. Räder, and Klaus Mü llen. Two-dimensional graphene nanoribbons. *JACS*, 130:4216, 2008.

[128] J. Campos-Delgado, J. M. Romo-Herrera, X. Jia, D. A. Cullen, H. Muramatsu, Y. A. Kim, T. Hayashi, Zh. Ren, D. J. Smith, Yu Okuno, T. Ohba, H. Kanoh, K. Kaneko, M. Endo, H. Terrones, M. S. Dresselhaus, and M. Terrones. Bulk Production of a New Form of sp^2 Carbon: Crystalline Graphene Nanoribbons. *Nano Letters*, 8:2773, 2008.

[129] X. Li, X. Wang, L. Zhang, S. Lee, and H. Dai. Chemically derived, ultrasmooth graphene nanoribbon semiconductors. *Science*, 319:1229, 2008.

[130] Z. Chen, Yu-M. Lin, M. J. Rooks, and Ph. Avouris. Graphene nanoribbon electronics. *Physica E: Low-dimensional Systems and Nanostructures*, 40:228, 2007.

[131] L. Jiao, L. Zhang, X. Wang, G. Diankov, and H. Dai. Narrow graphene nanoribbons from carbon nanotubes. *Nature*, 458:877, 2009.

[132] D. V. Kosynkin, A. L. Higginbotham, A. Sinitskii, J. R. Lomeda, A. Dimiev, B. K. Price, and J. M. Tour. Longitudinal unzipping of carbon nanotubes to form graphene nanoribbons. *Nature*, 458:872, 2009.

[133] A. L. Elías, A. R. Botello-Méndez, D. Meneses-Rodríguez, V. J.González, D. Ramírez-González, L. Ci, E. Muñoz-Sandoval andP. M. Ajayan, H. Terrones, and M. Terrones. Longitudinal Cutting of Pure and Doped Carbon Nanotubes to Form Graphitic Nanoribbons Using Metal Clusters as Nanoscalpels. *Nano Letters*, 10:366–372, 2010.

[134] L. Jiao, X. Wang, G. Diankov, H. Wang, and H. Dai. *Nature Nanotecnology*, 6:132, 2011.

[135] T. Orzali, M. Petukhov, M. Sambi, and E. Tondello. STM study of the initial stages of C_{60} adsorption on the Pt(110)-(1×2) surface. *Applied Surface Science*, 252:5534, 2006.

[136] J. Weckesser, J. V. Barth, and K. Kern. Mobility and bonding transition of $C60$ on Pd(110). *Phys. Rev. B*, 64:161403, 2001.

[137] F. Borgatti S. Iannotta M. Capozi G. Ciullo A. Stierle R. Felici, M. Pedio. X-ray-diffraction characterization of Pt(111) surface nanopatterning induced by C_{60} adsorption. *Nature Materials*, 4:688, 2005.

[138] C. Cepek and L. Gavioli. *Advanced Scanning Probe Methods V*, chapter 13. Springer, 2008.

[139] C.-P. Huang, C. C. Su, and M. S. Ho. Intramolecular structures of C_{60} and C_{84} molecules on Si(111)-7×7 surfaces by scanning tunneling microscopy. *Applied Surface Science*, 254:7712, 2008.

[140] H. Su, R. J. Nielsen, A. C. T. van Duin, and W. A. Goddard III. Simulations on the effects of confinement and Ni-catalysis on the formation of tubular fullerene structures from peapod precursors. *Phys. Rev. B*, 75:134107, 2007.

[141] R. Pfeiffer, M. Holzweber, H. Peterlik, H. Kuzmany, Zh. Liu, K. Suenaga, and H. Kataura. Dynamics of carbon nanotube growth from fullerenes. *Nano Letters*, 7:2428, 2007.

[142] J. Coraux, A. T. N'Diaye, M. Engler, C. Busse, D. Wall, N. Buckanie, M.-J. Meyer zu Heringdorf, R. van Gastel, B. Poelsema, and T. Michely. Growth of graphene on Ir(111). *New Journal of Physics*, 11:023006, 2009.

[143] T. Fujita, W. Kobayashi, and C. Oshima. Novel structures of carbon layers on a Pt(111) surface. *Surface and Interface Analysis*, 37:120, 2005.

[144] P. N. Rylander. *Organic syntheses with noble metal catalysts*. Academic Press, 1974.

[145] G. Schull, N. Néel, M. Becker, J. Kröger, and R. Berndt. Spatially resolved conductance of oriented C_{60}. *New Journal of Physics*, 10:065012, 2008.

[146] N. Kato, Y. Yamashita, S. Iida, N. Sanada, and M. Kudo. Analysis of TOF-SIMS spectra from fullerene compounds. *Applied Surface Science*, 255:938, 2008.

[147] M. Treier, C. A. Pignedoli, T. Laino, R. Rieger, K. Müllen, D. Passerone, and R. Fasel. Surface-Assisted Cyclodehydrogenation Provides a Synthetic Route Towards Easily Processable and Chemically Tailored Nanographenes. *Nature Chemistry*, 3:61, 2011.

[148] Y. Ohta, Y. Okamoto, S. Irle, and K. Morokuma. Temperature dependence of iron-catalyzed continued single-walled carbon nanotube growth rates: Density functional tight-binding molecular dynamics simulations. *The Journal of Physical Chemistry C*, 113:159, 2009.

[149] S. Hofmann, R. Sharma, C. Ducati, Andrea C. Du, G., R. Dunin-Borkowski, S. Lizzit, L. Petaccia, A. Goldoni, and J. Robertson. In situ observations of catalyst dynamics during surface-bound carbon nanotube nucleation. *Nano Letters*, 7:602, 2007.

[150] A. Müller, K. Yu. Amsharov, and M. Jansen. Synthesis of end-cap precursor molecules for (6, 6) armchair and (9, 0) zig-zag single-walled carbon nanotubes. *Tetrahedron Letters*, 51:3221, 2010.

[151] M. Fonin, M. Sicot, O. Zander, S. Bouvron, Ph. Leicht, U. Rdiger, M. Weser, Yu. S. Dedkov, and K. Horn. Spatial corrugation and bonding of single layer graphene on Rh(111). *arXiv.com*, 2006.

[152] A. B. Preobrajenski, May Ling Ng, A. S. Vinogradov, and N. Mårtensson. Controlling graphene corrugation on lattice-mismatched substrates. *Phys. Rev. B*, 78:073401, 2008.

[153] H. Ma, M. Thomann, J. Schmidlin, S. Roth, and T. Greber. Corrugated single layer templates for molecules: From h-BN Nanomesh to Graphene based Quantum dot arrays. *arXiv.com*, 2008.

[154] J. A. Meyer, I. D. Baikie, E. Kopatzki, and R. J. Behm. Preferential island nucleation at the elbows of the Au(111) herringbone reconstruction through place exchange. *Surface Science*, 365, 1996.

[155] D. D. Chambliss, R. J. Wilson, and S. Chiang. Nucleation of ordered Ni island arrays on Au(111) by surface-lattice dislocations. *Phys. Rev. Lett.*, 66:1721, 1991.

[156] M. Schmid, G. Kresse, A. Buchsbaum, E. Napetschnig, S. Gritschneder, M. Reichling, and P. Varga. Nanotemplate with holes: Ultrathin alumina on ni$_3$al(111). *Phys. Rev. Lett.*, 99:196104, 2007.

[157] A. Buchsbaum, M. De Santis, H. C. N. Tolentino, M. Schmid, and P. Varga. Highly ordered pd, fe, and co clusters on alumina on ni$_3$al(111). *Phys. Rev. B*, 81:115420, 2010.

[158] J.J. Gajewski. *Hydrocarbon thermal isomerizations*. Organic chemistry. Elsevier, 2004.

[159] M. Bieri, M.-T. Nguyen, Oliver Gröning, J. Cai, M. Treier, K. Aït-Mansour, P. Ruffieux, C. A. Pignedoli, D. Passerone, M. Kastler, K. Müllen, and R. Fasel. Two-dimensional polymer formation on surfaces: Insight into the roles of precursor mobility and reactivity. *Journal of the American Chemical Society*, 132:16669, 2010.

[160] F. Ullmann and Jean Bielecki. Über Synthesen in der Biphenylreihe. *Berichte der deutschen chemischen Gesellschaft*, 34:2174, 1901.

[161] W. Wang, X. Shi, S. Wang, M. A. Van Hove, and N. Lin. Single-molecule resolution of an organometallic intermediate in a surface-supported ullmann coupling reaction. *Journal of the American Chemical Society*, 133:13264, 2011.

[162] J. A. Lipton-Duffin, O. Ivasenko, D. F. Perepichka, and F. Rosei. Synthesis of polyphenylene molecular wires by surface-confined polymerization. *Small*, 5:592, 2009.

[163] Sze-Sze Ng, Chun-Yu Ho, K. D. Schleicher, and T. F. Jamison. Nickel-catalyzed coupling reactions of alkenes. *Pure and Applied Chemistry*, 80:929, 2008.

[164] D. K. Rayabarapu and C.-C. Cheng. Novel cyclization and reductive coupling of bicyclic olefins with alkyl propiolates catalyzed by nickel complexes. *Pure and Applied Chemistry*, 74:695, 2002.

[165] S.B. Sinnott, R. Andrews, D. Qian, A.M. Rao, Z. Mao, E.C. Dickey, and F. Derbyshire. Model of carbon nanotube growth through chemical vapor deposition. *Chemical Physics Letters*, 315:25, 1999.

[166] C. L. Cheung, A. Kurtz, H. Park, and C. M. Lieber. Diameter-controlled synthesis of carbon nanotubes. *The Journal of Physical Chemistry B*, 106:2429, 2002.

[167] E.F. Kukovitsky, S.G. L'vov, and N.A. Sainov. Vls-growth of carbon nanotubes from the vapor. *Chemical Physics Letters*, 317:65, 2000.

Acknowledgments

Without the support of many people in many places, this thesis could not have been written... I'd like to express my gratitude first of all to Prof. Kern for giving me the opportunity to carry out my PhD work in his group. His perspective on scientific questions, guidance and motivating environment he has created within the group were the driving force through my PhD time here.

My deepest gratitude is to Dr. Sebastian Stepanow. I was amazingly fortunate to have an advisor like him, who gave me the freedom to explore on my own, and at the same time the guidance to recover when my steps faltered. His suggestions and help made it so much easier to accomplish my work. Without his (sometimes *ab initio*) explanations, help with data analysis and critical approach, many of the things written in this thesis would not be there.

My special thanks goes to my office-mates in 7C6: Theresa Lutz, Alexander Langner, Christopher Kley, Gordon Rinke and Jakob Bork. Thank you all for creating such a friendly atmosphere in our office and for 'just being there'. Your jokes, the ability to say a kind word when it is needed the most were sometimes as important as the decisions how to proceed with my experiments. I am especially grateful to Theresa for numerous 'schoko-pausen'. I also would like to express my gratitude to the present and former members of my sub-group: Christopher Kley, Alexander Langner, TzuChun Tseng, Nan Jiang, Doris Grumelli and Jan Čechal. You were and are good friends and very nice colleges. Weather regarding the scientific or non-scientific matters you were there to help and discuss. Thank you all! I would be remiss not to also acknowledge people in the 6B15 and 4B6 labs: Nicha Thorntasen, Stephan Rauschenbach, Liza Herrera-Diez, Violetta Sessi, Sören Krotzky and Carola Srtaßer. Thanks for the cheerful atmosphere in the labs. The 4B6

deserves a special acknowledgment for tolerating me in their lab during my 'fullerene' and 'nanotube' projects. I would like to extend my gratitude to the whole Nanoscale Science Department for the cooperative atmosphere.

A word of sincere gratitude goes to my dear friends Doris Grumelli, Cristina Fenollar-Ferrer, Claudio Anselmi and Cecilia Blasetti. You were always there for me through all this time. Thanks for your kind support! I'm grateful to Cecilia Balsetti for her kind help on many occasions and for translating the abstract of my thesis into Italian; to Giuliano Gregori for adding a chemical touch to the Italian version of the abstract, even though he claims to be a material scientist :-); to Christopher Kley for translating the abstract into German.

Finally, I would like to thank my family and Seth for their unflagging love, understanding and encouragement.

Curriculum Vitæ

Name	Nasiba Abdurakhmanova
Date of Birth	31.12.1983
Nationality	Uzbek

2008-2011	PhD student in the group of Prof. Dr. Klaus Kern at the Max Planck Institute for Solid State Research in Stuttgart, Germany
2006-2008	Reaserch Assistant at the Surface Structure and Reactivity Group, Laboratio Nazionale TASC, Triest, Italy
2005-2006	Reaserch Fellow at the Condensed Matter Theory Group, University of Basel, Basel, Switzerland
2004-2005	Studies of Condensed Matter Physics at the International Centre for Theoretical Physics, Triest, Italy
2000-2004	Studies of Physics at the National University of Uzbekistan, Tashkent, Uzbekistan
1998-2000	High-School named after T. G. Shevchenko, Tashkent, Uzbekistan.